Magnetic Vortex Dynamics in the Thick Ferromagnetic Nanoelement

Hee-Sung Han

Department of Materials Science Engineering

Graduate school of UNIST

2016

Magnetic Vortex Dynamics in the Thick Ferromagnetic Nanoelement

Hee-Sung Han

Department of Materials Science Engineering

Graduate school of UNIST

Magnetic Vortex Dynamics in the Thick Ferromagnetic Nanoelement

A thesis
submitted to the Graduate School of UNIST
in partial fulfillment of the
requirements or the degree of
Master of Science

Hee-Sung Han

12. 04. 2015
Approved by

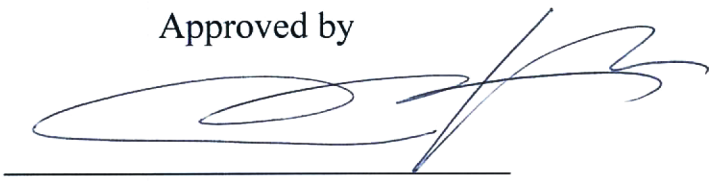

Advisor
Ki-Suk Lee

Magnetic Vortex Dynamics in the Thick Ferromagnetic Nanoelement

Hee-Sung Han

This certifies that the thesis of Hee-Sung Han is approved.

12. 04. 2015

Advisor: Ki-Suk Lee

Sukbin Lee: Thesis Committee Member #1

Mi-Young Im: Thesis Committee Member #2

Abstract

A magnetic vortex structure, which is formed in a ferromagnetic rectangular disk, circular disk, and elliptical disk, has attracted a lot of interest due to high thermal stability and structural rigidity among spatially non-uniform magnetization configuration. It consists of the in-plane curling magnetization configuration, which rotates either counterclockwise (CCW, c = +1) or clockwise (CW, c = -1), and out-of-plane magnetization configuration pointing either up (p = +1) or down (p = -1) which is called vortex core, *i.e.*, it has energetically equivalent fourfold states. It has been known that the magnetic vortex is very stable and it is hard to be deformed by the dynamics of vortex core below the critical velocity. The magnetization distribution of the magnetic vortex is uniform along the thickness and most of studies using micromagnetic simulation employed two dimensional numerical calculation, *i.e.*, the number of cell along the thickness is only one. The numerical simulation results are in a good agreement with experimental results when the thickness (< ~ 40 nm) is thin. However, the magnetization distribution of the magnetic vortex structure in the ground state is no longer uniform along the thickness when the thickness is relatively thick (> ~ 70 nm) and it causes a different dynamics compared to the magnetic vortex which is formed in thin ferromagnetic elements.

This thesis treats the dynamics of the magnetic vortex structure under an in-plane rotating magnetic fields and an out-of-plane spin-polarized current by micromagnetic numerical simulations in relatively thick circular disk (> ~ 70 nm).

Under an in-plane rotating magnetic fields, the dramatic time-varying deformation of vortex core during the gyration is observed in a relatively thick circular disk. Surprisingly, vortex core reversal does not occur although its velocity exceeds the critical velocity. Instead of vortex core reversals, the vortex core starts to tear up at the surface when the velocity of vortex core reaches some specific value as the amplitude of rotating magnetic fields increases more.

When the magnetic vortex is driven by out-of-plane spin polarized dc current, it is well-known that the spin transfer torque (STT) does not influence eigenfrequency of magnetic vortex while a circumferential Oersted (OH) fields make shift of eigenfrequency. Accordingly, the energetically equivalent states of magnetic vortex are split by whether the in-plane magnetization is parallel to OH fields or not. However, in relatively thick circular disk, only STT can make shift of eigenfrequency of the magnetic vortex and it is dependent on chirality of magnetic vortex. Furthermore, each split state shows different dynamics. It is completely different from the dynamics of magnetic vortex driven by in-plane rotating magnetic fields. In case of vortex for c = -1, the vortex dynamics shows the vortex-antivortex mediated reversal is observed regardless of whether OH fields is included or not while it cannot be observed under in-plane rotating magnetic fields. However, vortex for c = +1 shows the difference for dynamics. Only STT cannot induce vortex core reversal. It shows non-linear dynamics

instead of vortex core reversal, similar to the dynamics driven by rotating fields. The vortex core on the top surface is confined inside the small area while the vortex core on the bottom surface shows a large gyrotropic radius and undergo perturbation by vortex-antivortex pair. Interestingly, the vortex core reversal is observed when OH fields is included. However, it is achievable after chirality is reversed or both chirality and polarity are reversed simultaneously.

When ac spin-polarized current is applied, the magnetic vortex shows an eigenmode, corresponding to the size oscillation of vortex core in the interior region analogous to the breathing mode of a magnetic skyrmion and radial mode of a magnetic vortex. When out-of-plane ac spin-polarized current is tuned to the eigenfrequency corresponding to the size oscillation of vortex core, ultrafast vortex core reversal can be achievable and the switching time is faster (< ~1 ns). During the reversal process, the antivortex-vortex, edge-soliton and the injection of Bloch point at the surface cannot be observed. Interestingly, in the interior region, the magnetic vortex is disconnected and Bloch-point pair is formed. One Bloch point moves into top surface and the other moves into bottom surface with removing the original vortex core. Each Bloch point is annihilated at the surface layer and the reversal process is complete.

Finally, this thesis deal with a chaotic behavior in the formation of magnetic vortex structure. There is a fundamental hurdles to competitive magnetic-vortex-based memory device, chaos in the nucleation process. This thesis show comprehensive understandings on the deterministic chaos in the nucleation process of magnetic vortex in a nanodisk and we show that it can be manipulated simply by the breaking of the static- and dynamic-symmetries.

Contents

List of figures

Figure 3.6 The nonlinear dynamics of magnetic vortex in a circular disk with L = 80 nm, and H_0 = 20 Oe. (a) The gyro-radii and (b) the velocity of vortex core are not constant. Each color in (a) and (b) means the individual dynamic regions and it is distinguished by boundaries for the sign of acceleration of vortex core on the top and bottom surface. The trajectories of individual regions is shown in (c).

Figure 3.7 The gyro-radii when the amplitude increases (a), (c), (e) non-adiabatically and (d), (f) adiabatically in the circular disk with (c-d) L = 80 nm, and (a), (e-f) 100 nm. The amplitude H_0 is following : (a) 40 Oe, (c-d) 25 Oe, and (e-f) 50 Oe. Fig. (b) shows the time evolution of amplitude H_0 to mimic an adiabatic process. Initially, H_0 increases with a gradient 0.25 Oe / ns and at the 25 Oe (50 Oe), H_0 is fixed at the Fig. (d) (Fig. (f)).

Figure 3.8 Two types of tearing up a vortex core at (a-b) the bottom surface and at (c) the top surface. At the bottom surface, the torn vortex core (vortex tube structure) is annihilated by (a) the collision with the edge and (b) combination with new nucleated non-zero m_z.

Figure 3.9 At the bottom surface, the annihilation process of vortex tube by (a) the collision with the edge of disk and the combination with non-zero m_z which consists of vortex-antivortex pair.

Figure 3.10 The three-dimensional image of vortex tube structure.

Figure 3.11 (a) The phase diagram of vortex dynamics with varying H_0 and L. The green region shows the non-linear and the linear gyrotropic motion of vortex core. The blue region means the vortex core reversals. The red color means the vortex core tearing. The yellow region means that the magnetic vortex shows gyrotropic motion in the adiabatic process and tearing up a vortex core in the non-adiabatic process. (b) The required velocity for tearing up vortex core at the top surface (magenta circle) and bottom surface (cyan circle). The region colored in yellowish green in Fig. (b) is a critical velocity required for vortex core reversals in Py disk.

Figure 3.12 (a) The isolated magnetic vortex structure. (b) The strength of OH fields versus the distance **r** from the center of the disk.

Figure 3.13 The shift of eigenfrequency of magnetic vortex when the out-of-plane spin polarized current is applied. At each point, the magnetic vortex shows the linear gyrotropic motion. An orange color and green color mean c = +1 and c = -1. The open triangle includes both STT and OH fields while

List of tables

1. Introduction

These days, thanks to remarkable development of the electronic technology, we live in comfortable circumstances which were unavailable in times past. The digital information storage device and processing device play an important role in electronic age. However, these electronic device uses the mechanical moving. In cased of hard disk drives, it works by moving read/write heads. It is slow, and spend a lot of energy cost. Also, it is easy to lose data and be broken by the collision.

In nanometer-scaled ferromagnetic elements, magnetization dynamics have been studied in the fields of naomagnetism and spintronics due to fundamental interests and technological applications and many researchers are trying to solve the problem of present electronic device using the magnetization dynamics. Especially, the dynamics of spatially non-unfirom magnetization configuration have attracted**.** For example, STT-MRAM (Spin Transfer Torque-Magnetic Random Access Memory) [1-4] will be released commercially to replace DRAM (Dynamic Random Access Memory). Racetrack memory, proposed by IBM group leader, Stuart S.P.Parkin, is a hot issue in the magnetic academic world using moving of domain wall induced by current [5,6].

Especially, magnetic vortex structure, which is formed in a ferromagnetic rectangular disk, circular disk, and prism, has attracted a lot of interest due to high thermal stability and structural rigidity among spatially non-uniform magnetization configuration. The magnetic vortex structure consists of the in-plane curling magnetization configuration, which rotates either counterclockwise (CCW, c = +1) or clockwise (CW, c = -1), and out-of-plane magnetization configuration pointing either up (p = +1) or down (p = -1) which is called vortex core , i.e., it has energetically equivalent fourfold states. A vortex core reversals can be achievable through the resonant excitation of their eigenmode with low power. For these reason, VRAM (Vortex Random Access Memory) is proposed [7] and prototype of VRAM is manufactured by the foremost scientists [8,9]. Furthermore, a dynamic properties of vortex core makes possible manufacture new type of spin torque vortex oscillators (STVOs) [10-12]. However, it has been studied in a thin film for over the past decade, i.e. two dimensional (2D) system.

Recently, advanced sample fabrication and super computing system make a lot of studies of three dimensional (3D) system such as spheres [13,14], half spheres [15], and spherical shells [15-17], be possible. It shows that magnetic vortex in 3D system has a rich variety of the dynamics compared to that in 2D system. It is reported flexure oscillations of the vortex core with higher order frequency along the disk thickness [18-22]. However, the understanding the dynamics of magnetic vortex formed in thick circular disk is insufficient yet.

This thesis shows the dynamics of the magnetic vortex structure under in-plane rotating magnetic fields and spin transfer torque (STT) by micromagnetic numerical simulations in 3D system. Chapter 1 introduces magnetic vortex structure, its dynamic properties and micromagnetic simulations. In Chapter 2, the thickness dependence of magnetic vortex structure is presented. In Chapter 3, the magnetic vortex

dynamics under in-plane rotating magnetic fields, DC out-of-plane spin-polarized current and AC out-of-plane spin-polarized current. Finally, in Chapter 4, the formation of magnetic vortex structure is dealt with. In Chapter 5, a magnetic vortex dynamics in relatively thick circular disk are summarized.

1.1 Introduction to magnetic vortex structure

A magnetic vortex structure is one of a non-uniform magnetization configuration in a ferromagnetic nano-scaled element. The magnetic vortex is stabilized by the competition between exchange energy and magnetostatic energy. Within the framework of exchange energy, the system is stable when the spins is parallel to each other (See Fig. 1.1(a)). In contrast, the magnetostatic energy is lowest when there is no free pole in the sample. As seen in Fig. 1.1(b), all spins are arranged along a longitudinal direction and this arrangement makes free pole minimized. In other words, it minimizes emitting stray fields.

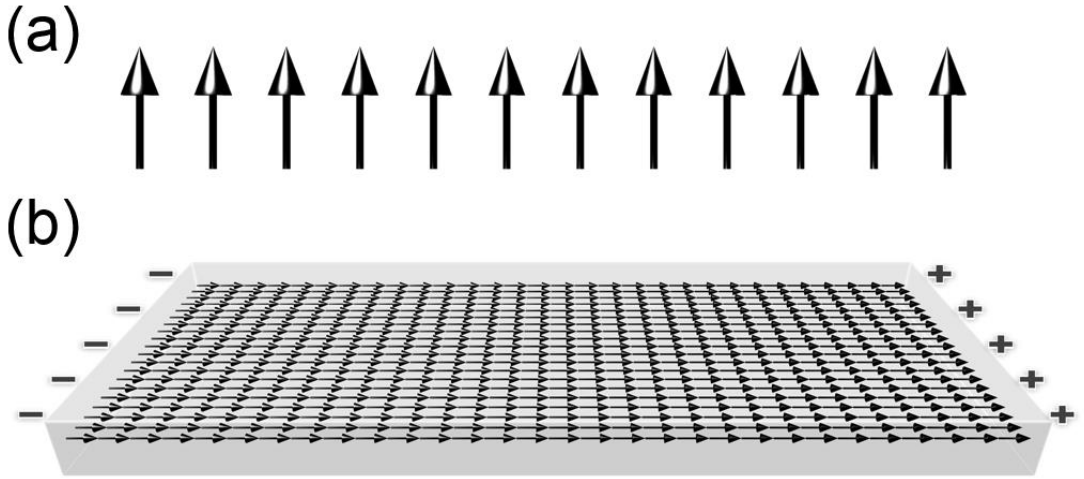

Figure 1.1 (a) parallel spin arrangement induced by exchange coupling. (b) The spins which arranged along easy axis induced by dipole-dipole interaction.

Accordingly, the competition between two energies causes a unique spin configuration in the nano-scaled ferromagnetic element. All spins at the edge are parallel to the spin in order to decreases magnetostatic energy. As a result, this unique structure has in-plane curling magnetization (See Fig. 1.2(b)). However, at the center, the singularity occurs, which causes explosion of the exchange energy when in-plane curling magnetization maintain (See Fig. 1.2(c)). It makes out-of-plane magnetization at the center in order to avoid explosion of the exchange energy. It is called magnetic vortex due to appearance analogous to typhoons, as presented in Fig. 1.2(a).

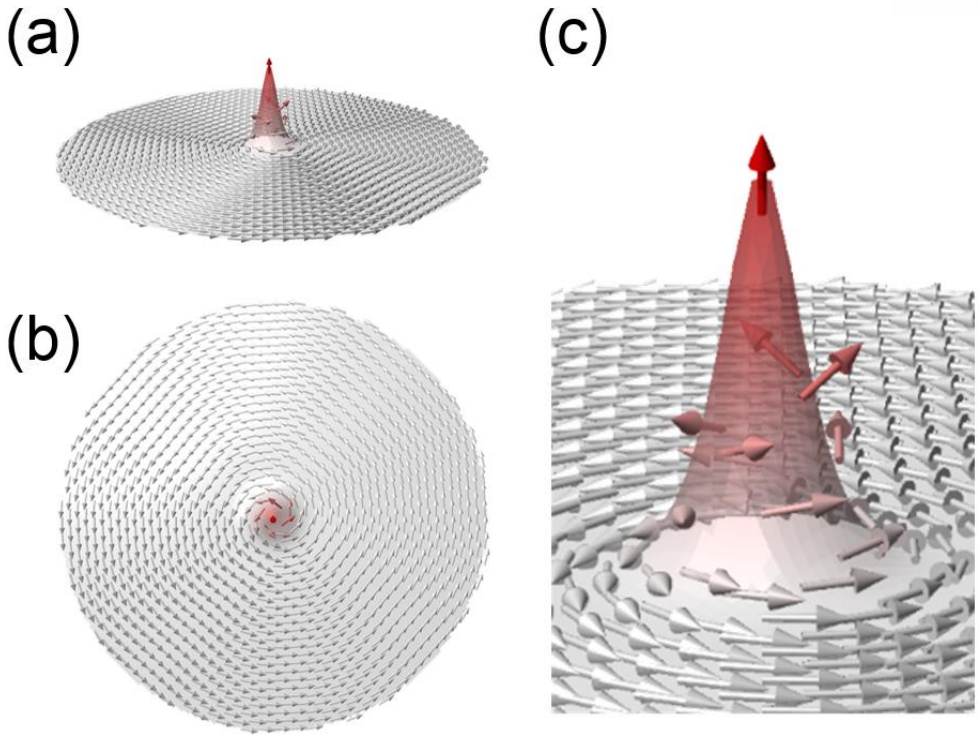

Figure 1.2 (a) The magnetic vortex structure which consists of (b) in-plane curling magnetization and (c) out-of-plane magnetization in the ferromagnetic nano-scaled disk.

The magnetization is aligned at the edge for decreasing the free pole. As above mentioned, there is out-of-plane magnetization structure at the disk center and it is called the vortex core. A magnetic vortex, which consist of a chirality c which means in-plane curling magnetization direction and a polarity p which means the vortex core direction, *i.e.*, it has energetically equivalent fourfold states in shown Fig. 1.3. p = +1 (-1) means upward (downward) core direction and c = +1 (-1) means counterclockwise (clockwise) direction.

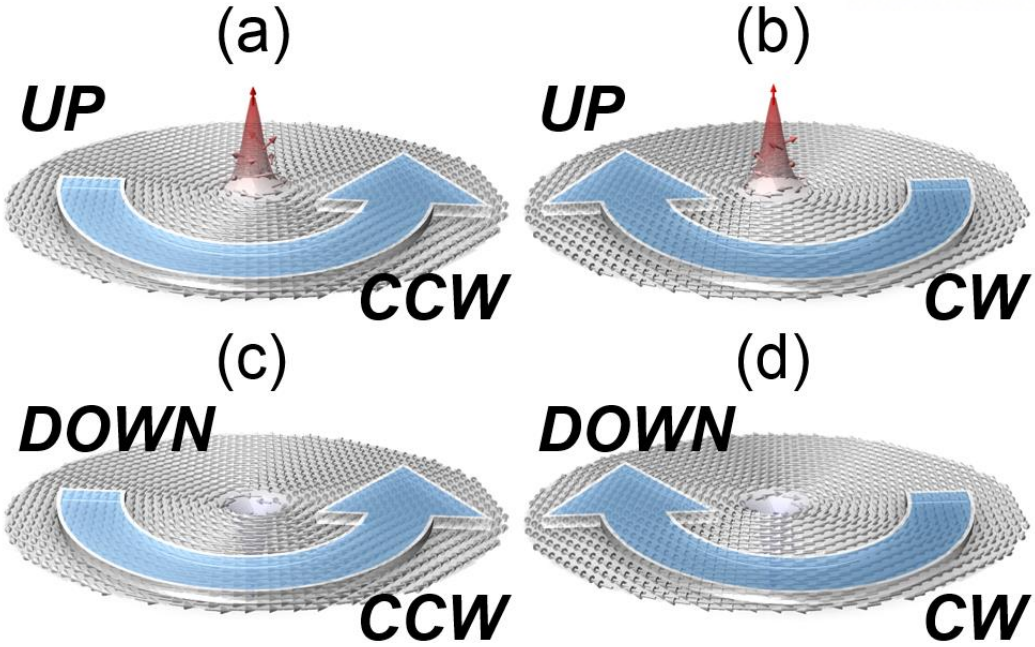

Figure 1.3 Energetically equivalent quaternary states of magnetic vortex structure.

In the past, the existence of magnetic vortex structure was only studied by the physical theory due to absence of an imaging and sample fabrication technique. The first observation of magnetic vortex is achieved in 1965 by M. S. Cohen using Lorentz microscopy [23]. A Lorentz microscopy is used for observation of chirality of magnetic vortex structure [23,24]. As time goes, Shinjo observed the magnetic vortex core using magnetic force microscopy (MFM) in 2000 [25]. Miltat and Thiaville observed magnetic vortex using low angle diffraction in 2002 [26]. Wachowiak used spin-polarized scanning tunneling microscopy (SP-STM) to show the polarity and chirality in a Fe island and it showed vortex core size obviously [27]. The chirality and polarity of magnetic vortex can be observed by magnetic transmission x-ray microscopy (MTXM) [28].

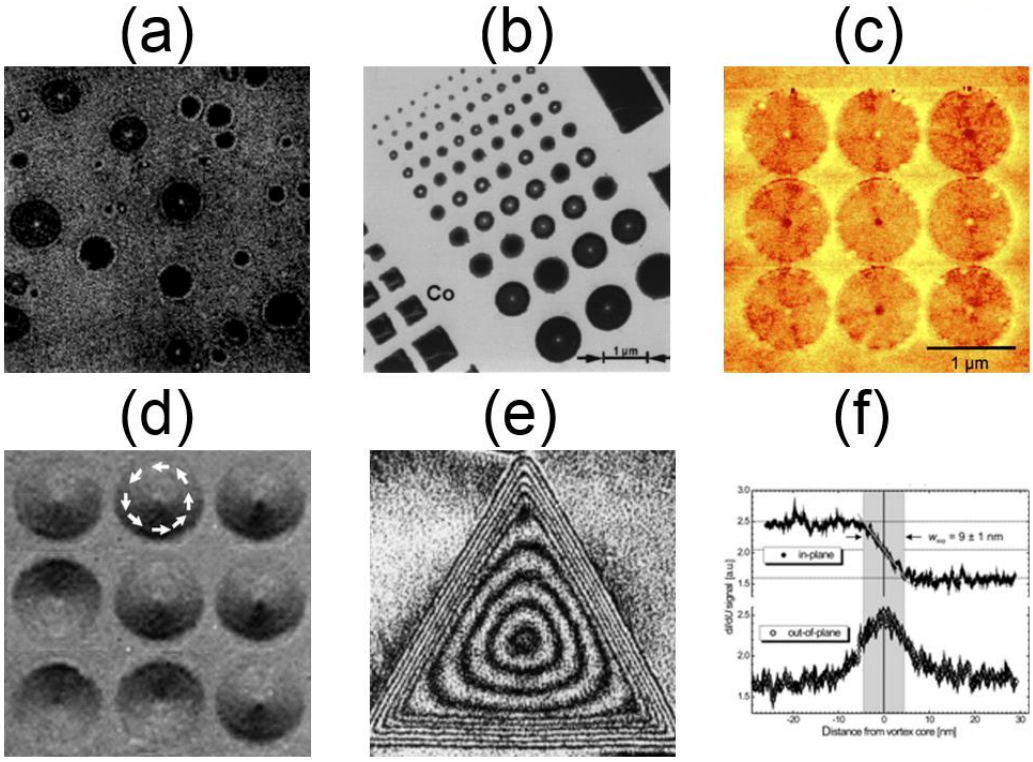

Figure 1.4 The experimental observation using (a-b) Lorentz microscopy, (c) magnetic force microscopy (MFM) (d) magnetic transmission x-ray microscopy (MTXM), (e) electron holography, and (f) spin-polarized scanning tunneling microscopy (SP-STM) [23-28].

1.2 Dynamic properties of magnetic vortex

The magnetic vortex has a variety of dynamic modes such as gyrotropic mode [29], azimuthal and radial spin wave mode [30-32]. Such dynamic characteristics gives a possibility to develop a nano-oscillator and signal transfer device. In this section, the dynamic modes of magnetic vortex are introduced.

1.2.1. Low frequency mode

The gyrotropic mode is the low frequency translational mode magnetic vortex. It has been predicted from Thiele equation [29,33] which can be derived by Landau-Lifhsitz Gilbert (LLG) equation .

$$G \times \dot{\mathbf{X}} + D \cdot \dot{\mathbf{X}} - \frac{\partial W(\mathbf{X})}{\partial \mathbf{X}} = 0$$

The frequency of gyrotropic modes can be calculated based on the two vortex side-charge free model and its value $\omega_0 = \dfrac{\kappa}{p|G| + D}$. It is well corresponded to the system where the aspect ratio L/R << 1.

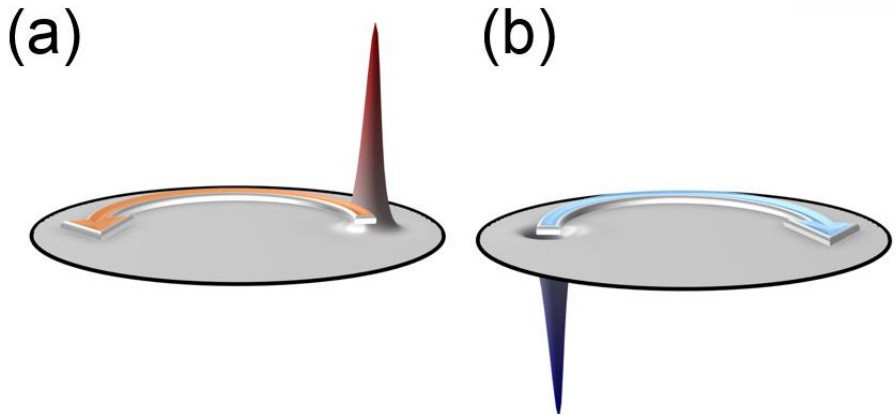

Figure 1.5 The rotating sense of magnetic vortex when it shows gyrotropic motion. The vortex core with p = +1 (-1) rotates counterclockwise (clockwise).

This dynamic motion of vortex core have been observed by time-resolved MTXM [34].

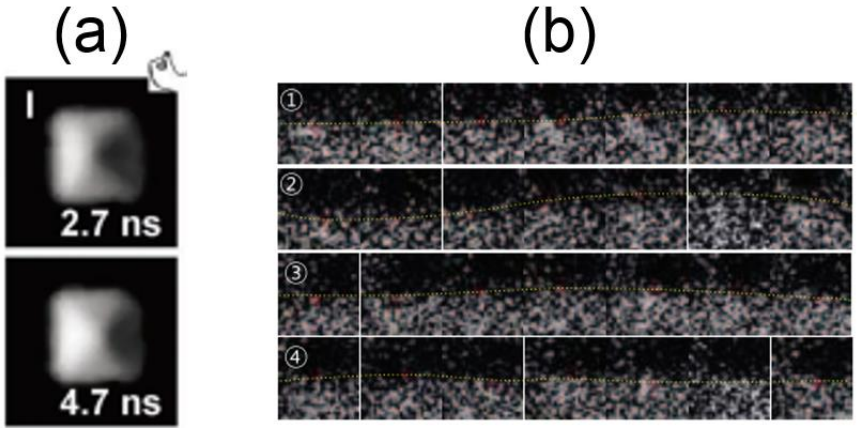

Figure 1.6 The snapshot of gyrotropic motion of magnetic vortex in (a) a rectangular prism and (b) a circular disk which is observed by time-resolved MTXM.

S.-B. et al., observed the gyrotropic motion of magnetic vortex which is formed in the rectangular prism in 2004 using time-resolved MTXM [35]. Then, gyrotropic motion of magnetic vortex in a circular is also observed using time-resolved MTXM [36]. The most interesting point of gyrotropic mode is that vortex core reversal occurs if the external stimulus is applied to the magnetic vortex with the frequency corresponding the eigenfrequency of gyrotropic mode [37-39].

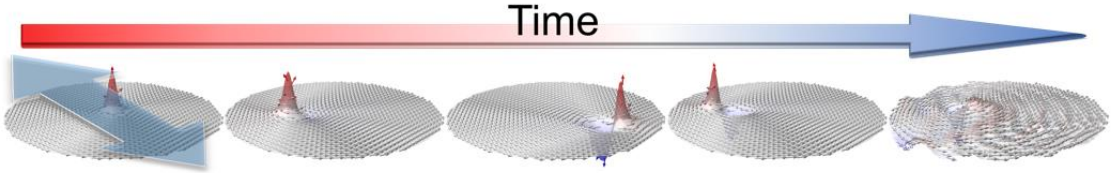

Figure 1.7 A vortex core reversals through resonant exaction of gyrotropic motion using a linearly oscillated magnetic fields.

1.2.2. High frequency mode

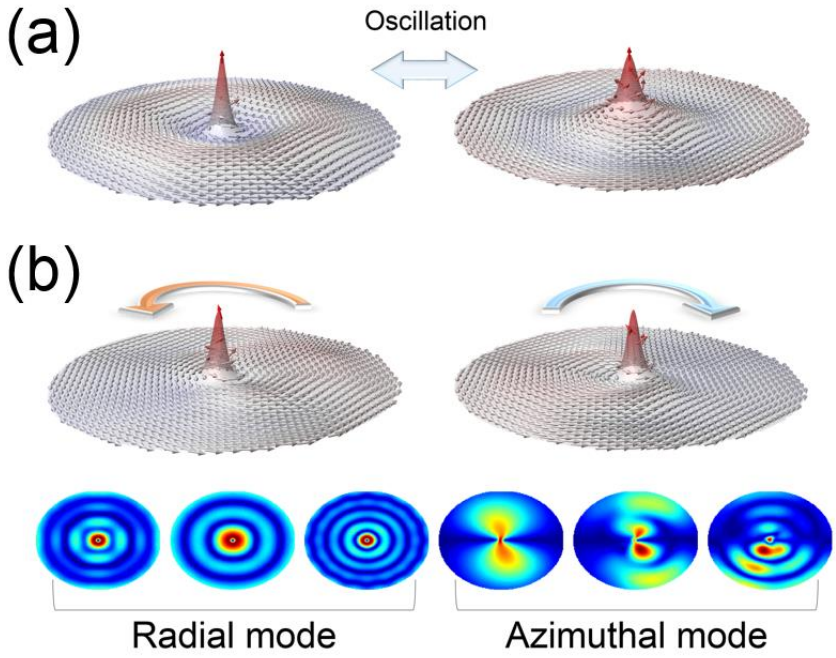

Figure 1.8 The high frequency mode of magnetic vortex. (a) A radial and (b) azimuthal spin wave mode of magnetic vortex. Fig. (c) shows the spatial distribution of FFT intensity corresponding to the radial and azimuthal spin wave mode.

An azimuthal spin wave mode and radial spin wave mode is the spin wave mode of magnetic vortex structure with a high frequency [30-32]. It can be divided by the number of node on the in-plane. A resonant excitation with these modes make vortex core reversal with low power [40-42]. The resonant excitation with high frequency spin wave mode reduces the switching time compared to the vortex core reversals through the resonant excitation with gyrotropic mode.

1.3 Micromagnetic simulations

All energy, related to the magnetization procession, can be considered as the perturbation by adding to the Heisenberg Hamiltonian. However, a lot of approximation is necessary to solve it quantum mechanically. As a results, classical theory, which consider an atomic spin as a classical vector in a continuous medium, has been developed. Landau and Lifshitz published the paper in 1935 [43] and it is considered as the start of micromagnetics and Brown named this theory micromagnetics [44]. The micromagnetics is powerful tool for describing the spin procession and it is widely used for spintronics research. This part manipulate time evolution of magnetization and micromagnetic simulation.

Landau and Lifshitz proposed the equation describing the dynamic properties of magnetization and it is modified with substituting damping term with the time evolution of magnetization [45]. It is called the Landau-Lifshitz-Gilbert (LLG) equation.

$$\frac{d\mathbf{M}}{dt} = -\gamma\left(\mathbf{M}\times\mathbf{H}_{eff}\right) + \frac{\alpha}{M_s}\left(\mathbf{M}\times\frac{d\mathbf{M}}{dt}\right) + \mathbf{T}_{STT} + \mathbf{T}_{SHT} + \mathbf{T}_{RT} \quad (1.1)$$

M is the magnetization vector and γ is the gyromagnetic ratio and α is the Gilbert damping constant and M_s is the saturation magnetization. In equation (1.1), $\mathbf{H}_{eff}$ is the effective field and it is expressed as the derivative of total energy $\mathbf{H}_{eff} = -\delta E/\delta \mathbf{M}$. The effective field is separated into the exchange field $\mathbf{H}_{exch}$, the anisotropy field $\mathbf{H}_{ani}$ and the demagnetization field $\mathbf{H}_{demag}$ and Zeeman field $\mathbf{H}_{Zeeman}$ and Dzyaloshinskii-Moriya field $\mathbf{H}_{DM}$. That is, $\mathbf{H}_{eff} = \mathbf{H}_{eff} + \mathbf{H}_{ani} + \mathbf{H}_{demag} + \mathbf{H}_{Zeeman} + \mathbf{H}_{DM}$. Each effective field can be obtained from the negative variational derivative of the energy density.

The electrical currents makes the torque at the local magnetization. $\mathbf{T}_{STT}$, $\mathbf{T}_{SHT}$ and $\mathbf{T}_{RT}$ are spin-transfer torque (STT) [1,2], spin Hall torque (SHT) and Rashba torque (RT). Both spin Hall torque and Rashba torque are called spin-orbit torque (SOT) [46,47].

$$\mathbf{T}_{STT} = \frac{u}{M_s}\left(\hat{x}\cdot\nabla\right)\mathbf{M} - \frac{\beta}{M_s^2}u\mathbf{M}\times\left(\hat{x}\cdot\nabla\right)\mathbf{M} \quad (1.2)$$

$$\mathbf{T}_{SHT} = \frac{\gamma}{M_s^2}\mathbf{M}\times\left(\mathbf{M}\times H_{SH}\hat{y}\right) \quad (1.3)$$

$$\mathbf{T}_{RT} = \mathbf{T}_{FT} + \mathbf{T}_{ST} = -\gamma\mathbf{M}\times H_R\hat{y} + \gamma\frac{\beta}{M_s}\mathbf{M}\times\left(\mathbf{M}\times H_R\hat{y}\right) \quad (1.4)$$

Spin transfer torque is the torque originated from the interaction between a conduction electron and local magnetic moment [1,2,48,49]. A spin of conduction electron is changed by the local magnetization of the magnetic layer when the conduction electron pass through the magnetic layer. To conserve the angular momentum, there occurs the torque at the local magnetization. A spin Hall torque and Rashba torque is originated from spin orbit coupling. Spin Hall torque is originated from a spin Hall effect and Rashba torque is originated from a Rashba effect[46,47]. This two effects is dominant compared to the spin-transfer torque when the system is under strong spin orbit coupling [46,50-54].

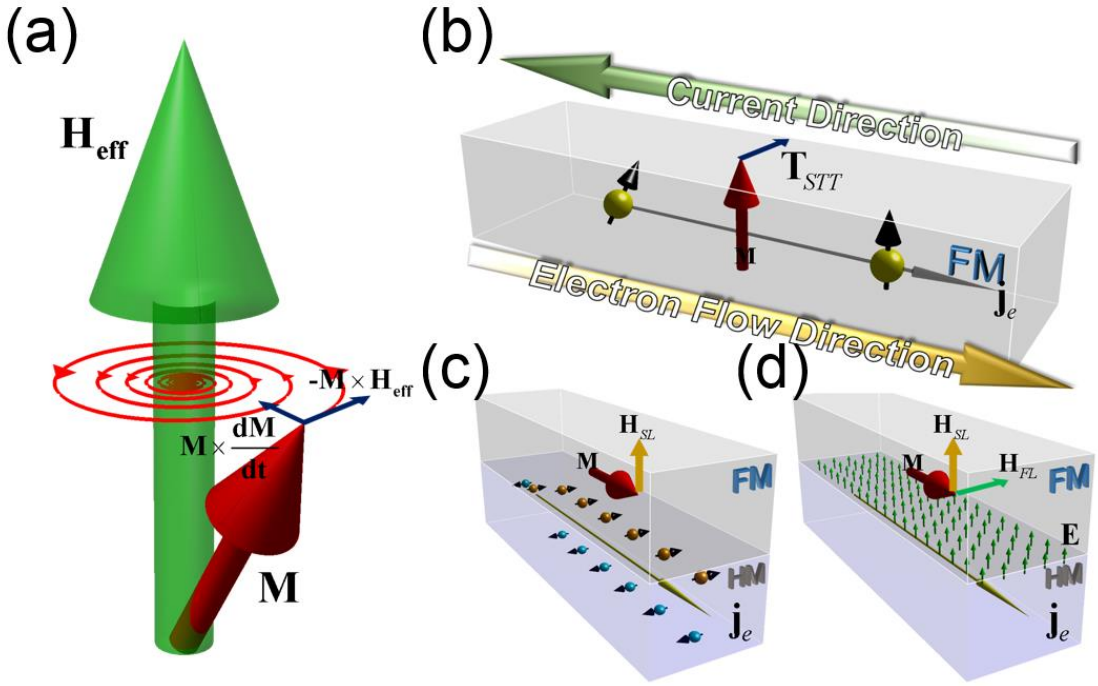

Figure 1.9 (a) The precession motion of local magnetization by Landau-Lifshitz Gilbert equation. An additional torque, such as (b) spin-transfer torque, (c) spin Hall torque, and (d) Rashba torque, can occur by an electrical current.

1.3.1. Micromagnetic energy

Figure 1.10 An illustration of a representative five micromagnetic energy.

The magnetization configuration in ferromagnetic materials is determined by a lot of magnetic energies. The exchange energy is quantum-mechanical energy which describes the interaction with neighbor spin. The magnetostatic energy is originated from the interaction between spins and stray fields induced by neighbouring spin, *i.e.*, dipole-dipole interaction. The magnetocrystalline anisotropy

energy is the energy by coupling with lattice, orbit and spin. Zeeman energy is the interaction between an external magnetic fields and spin. Dzyaloshinskii-Moriya energy is induced by the broken symmetry in B20 materials or interface [55,56]. In this section, the contents are summaries of Ref.[57-59].

1.3.1.1. Exchange energy

In the Heisenberg model, spin Hamiltonian is described as

$$\mathrm{H} = -2\sum_{i,j} J_{i,j}\mathbf{S}_i \cdot \mathbf{S}_j \quad (1.5)$$

As an atomic spin *S* is considered as the classical vector and the exchange energy is

$$-2JS^2 \sum_{neighbours} \cos\phi_{i,j} \quad (1.6)$$

In the continuous medium, $\phi_{i,j}$ is small. That is, the energy loss when the atomic spin is changed from all parallel spins state can be approximated into

$$\delta E_{exchange} = 2JS^2 n\sum_i (1-\cos\phi_{i,j}) = 4JS^2 n\sum_i \sin^2\left(\frac{1}{2}\phi_{i,j}\right) \approx JS^2 n\sum_i \phi_{i,j}^2 \quad (1.7)$$

In micromagnetics, this energy loss is considered as the exchange energy by redefining the reference state. Accordingly, exchange energy is redefined as

$$E_{exchange} = JS^2 \sum_{neighbours} \phi_{i,j}^2 \quad (1.8)$$

Also, $\phi_{i,j}$ can be re written as $(s_i \cdot \nabla)\mathbf{m}$ and s_i means the position vector and **m** is a unit vector which is parallel to the spin direction and the magnetization vector. As a results, for simple cubic lattice, exchange energy is defined as

$$E_{exchange} = JS^2 \sum_{neighbours} \sum_{\mathbf{s_i}} \left[(s_i \cdot \nabla)\mathbf{m}\right]^2 = \int w_e d\tau \quad (1.9) \text{ where}$$

$$w_e = A_{ex}\left[(\nabla m_x)^2 + (\nabla m_y)^2 + (\nabla m_z)^2\right] \quad (1.10), A_{ex} = 2JS^2/a \text{ and } a \text{ is a lattice constant.}$$

1.3.1.2. Magnetostatic energy

The magnetostatic energy can be derived from Maxwell equation.

$$\nabla \cdot \mathbf{B} = 0 \quad (1.11)$$

$$\nabla \times \mathbf{H} = \mathbf{J} + \varepsilon_0 \frac{\partial \mathbf{E}}{\partial t} \quad (1.12)$$

From Eq. (1.8), $\nabla \cdot \mathbf{H} = -\nabla \cdot \mathbf{M}$. **H** can be written using a magnetic scalar potential $\mathbf{H} = -\nabla\phi$. if the current density **J** and time derivative of electric field vanishes in Eq. (1.13). As a results, a magnetic scalar potential can be rewritten as

$$\nabla^2\phi = \nabla\cdot\mathbf{M} \quad (1.14)$$

It is in the form of Poisson equation. The solution of the magnetic scalar potential is

$$\phi = \frac{1}{4\pi}\int_V \frac{\hat{\varsigma}\cdot\mathbf{M}}{\varsigma^2}dV' \quad \text{where} \quad \varsigma = |\mathbf{r}-\mathbf{r}'| \quad (1.15)$$

Using $\nabla'\left(\frac{1}{\varsigma}\right) = \frac{\hat{\varsigma}}{\varsigma^2}$,

$$\begin{aligned}\phi &= \frac{1}{4\pi}\int_V \mathbf{M}\cdot\nabla'\left(\frac{1}{\varsigma}\right)dV' \\ &= \frac{1}{4\pi}\left[\int_V \nabla'\cdot\left(\frac{\mathbf{M}}{\varsigma}\right)dV' - \int_V \frac{1}{\varsigma}(\nabla'\cdot\mathbf{M})dV'\right]\end{aligned} \quad (1.16)$$

By divergence rule,

$$\phi = \frac{1}{4\pi}\left[-\int_V \frac{\nabla'\cdot\mathbf{M}}{|\mathbf{r}-\mathbf{r}'|}dV' + \int_S \frac{\mathbf{n}\cdot\mathbf{M}}{|\mathbf{r}-\mathbf{r}'|}dS'\right] = \frac{1}{4\pi}\left[\int_V \frac{\rho(\mathbf{r}')}{|\mathbf{r}-\mathbf{r}'|}dV' + \int_S \frac{\sigma(\mathbf{r}')}{|\mathbf{r}-\mathbf{r}'|}dS'\right] \quad (1.17)$$

where $\rho = -\nabla'\cdot\mathbf{M}$ is a volume charge density and $\sigma = -\mathbf{n}\cdot\mathbf{M}$ $\sigma = \mathbf{n}\cdot\mathbf{M}$ is a surface charge density. Using $-\frac{1}{2}\mathbf{M}\cdot\int\mathbf{H}\,dV$ and $\mathbf{H} = -\nabla\phi$, we can derive the magnetostatic energy. For example, in a uniformly magnetized ellipsoidal medium, $-\nabla'\cdot\mathbf{M} = 0$ and the magnetic scalar potential is $\phi = \frac{1}{4\pi}\mathbf{M}\cdot\int_S \frac{\mathbf{n}}{|\mathbf{r}-\mathbf{r}'|}dS'$.

Accordingly, demagnetizing field is

$$\mathbf{H} = -\frac{1}{4\pi}\nabla\left(\int_S \frac{\mathbf{M}\cdot\mathbf{n}}{|\mathbf{r}-\mathbf{r}'|}dS'\right) = -\frac{1}{4\pi}\nabla\left(\mathbf{M}\cdot\int_S \frac{\mathbf{n}}{|\mathbf{r}-\mathbf{r}'|}dS'\right) \quad (1.18)$$

M is considered as a constant and it can be taken out of the integral and the differentiation and it means the demagnetizing field is linear function and it can be expressed as $\mathbf{H}_i = -\mathbf{N}_{ij}\cdot\mathbf{M}_j$ and $\mathbf{N}_{ij}$ is the demagnetizing tensor. Likewise, the magnetostatic energy is represented as

$$\begin{aligned}E_{magnetostatic} &= -\frac{1}{2}\mathbf{M}\cdot\int\mathbf{H}\,dV = \frac{1}{2}\mathbf{M}\cdot\int\mathbf{N}_{ij}\cdot\mathbf{M}_j\,dV \\ &= \frac{1}{2}V(N_{11}M_x^2 + N_{12}M_xM_y + \cdots)\end{aligned} \quad (1.19)$$

1.3.1.3. Magnetocrystalline anisotropy energy

Magnetocrystalline anisotropy is an intrinsic properties and its origin is spin-orbit coupling. Both easy axis and hard axis are determined by the crystal symmetry. That is, the dynamics of magnetization

is different as there exists a magnetocrystalline anisotropy. For the simple cubic structure, the magnetocrystalline energy is given by

$$E_{ani} = \int K_{1c}(\alpha_1^2\alpha_2^2 + \alpha_2^2\alpha_3^2 + \alpha_3^2\alpha_1^2) + K_{2c}(\alpha_1^2\alpha_2^2\alpha_3^2)\, dV \quad (1.20)$$

K_{1c} and K_{2c} are the anisotropy constants and α_i is the direction cosine of the magnetization. For the hexagonal structure, generally the direction of easy axis is *c*-axis. A magnetization process is the same regardless of the direction in the basal plane. It is called as a uniaxial magnetocrystalline anisotropy and it is given by

$$E_{ani} = \int K_0 + K_1 \sin^2\theta + K_2 \sin^4\theta\, dV \quad (1.21)$$

K_i is the anisotropy constants and θ is the angle between the magnetization and *c*-axis.

1.3.1.4. Dzyaloshinskii-Moriya energy

When there exists the inversion symmetry breaking, antisymmetric exchange coupling occurs and it is called Dzyaloshinskii-Moriya interaction (DMI). It is expressed as

$$E_{DM} = \sum_{neighbours} d_{ij} \cdot \vec{S}_i \times \vec{S}_j \quad (1.22)$$

For interfacial DMI, the DM interaction vector $d_{ij} = ds_{ij} \times \hat{\boldsymbol{z}}$, DM energy is rewritten as

$$E_{DM} = \sum_{neighbours} \left(ds_{ij} \times \hat{\boldsymbol{z}}\right) \cdot \left(\vec{S}_i \times \vec{S}_j\right) \quad (1.23)$$

Using $A \cdot (B \times C) = C \cdot (A \times B) = B \cdot (C \times A)$, the DM energy can be rewritten as

$$E_{DM} = d \sum_{neighbours} S_j \cdot \left[(s_{ij} \times \hat{\boldsymbol{z}}) \times \vec{S}_i\right] \quad (1.24)$$

Using $(A \times B) \times C = -A(B \cdot C) + B(A \cdot C)$, the DM energy can be rewritten as

$$E_{DM} = dS^2 \sum_{neighbours} \left[-m_z(m_j \cdot s_{ij}) + (m_j \cdot \hat{\boldsymbol{z}})(m_i \cdot s_{ij})\right] \quad (1.25)$$

For simple cubic lattice, along positive x direction, and $m_j \sim (dm_j/dx)a$

$$E_{DM} = dS^2 a \sum_{neighbours} \left[-m_z \frac{dm_x}{dx} + m_x \frac{dm_z}{dx}\right] \quad (1.26)$$

Along negative x direction, $j = i-1$ and $m_j \sim -(dm_j/dx)a$, it causes the same results as Eq.(1.26). Likewise, along y direction,

$$\begin{aligned} E_{DM} &= dS^2 a \sum_{neighbours} \left[-m_z \frac{dm_y}{dy} + m_y \frac{dm_z}{dy}\right] \\ &= 2dS^2 a \sum_{neighbours} \left(m_x \frac{dm_z}{dx} - m_z \frac{dm_x}{dx}\right) + \left(m_y \frac{dm_z}{dy} - m_z \frac{dm_y}{dy}\right) \end{aligned} \quad (1.27)$$

By changing it into integral form,

$$\begin{aligned} E_{DM} &= \frac{t}{2}\iint \frac{2dS^2a}{Nta^2}\left[\left(m_x\frac{dm_z}{dx}-m_z\frac{dm_x}{dx}\right)+\left(m_y\frac{dm_z}{dy}-m_z\frac{dm_y}{dy}\right)\right]dr^2 \\ &= t\iint \frac{dS^2}{Nat}\left[\left(m_x\frac{dm_z}{dx}-m_z\frac{dm_x}{dx}\right)+\left(m_y\frac{dm_z}{dy}-m_z\frac{dm_y}{dy}\right)\right]dr^2 \\ &= t\iint D\left[\left(m_x\frac{dm_z}{dx}-m_z\frac{dm_x}{dx}\right)+\left(m_y\frac{dm_z}{dy}-m_z\frac{dm_y}{dy}\right)\right]dr^2 \end{aligned} \quad (1.28)$$

For Bulk DMI, the DM interaction vector $d_{ij} = ds_{ij}$, DM energy is rewritten as

$$E_{DM} = d\sum_{neighbours} s_{ij}\cdot\left(\vec{S}_i\times\vec{S}_j\right) = d\sum_{neighbours}\vec{S}_i\cdot\left(\vec{S}_j\times s_{ij}\right) = dS^2\sum_{neighbours} m_i\cdot\left(m_j\times s_{ij}\right) \quad (1.29)$$

For simple cubic lattice, along positive x direction, and $m_j \sim (dm_j/dx)a$,

$$E_{DM} = dS^2a\sum_{neighbours} m\cdot\left(\frac{dm}{dx}\times\hat{\boldsymbol{x}}\right) \quad (1.30)$$

Likewise,

$$E_{DM} = dS^2a\sum_{neighbours} m\cdot\left[\left(\frac{dm}{dx}\times\hat{\boldsymbol{x}}\right)+\left(\frac{dm}{dy}\times\hat{\boldsymbol{y}}\right)+\left(\frac{dm}{dz}\times\hat{\boldsymbol{z}}\right)\right] = dS^2a\sum_{neighbours} m\cdot\nabla\times(-m) \quad (1.31)$$

By changing it into integral form,

$$\begin{aligned} E_{DM} &= \frac{1}{2}\iiint -\frac{dS^2a}{Na^3}\,m\cdot\nabla\times m\,dr^3 \\ &= \iiint -\frac{dS^2}{2Na^2}\,m\cdot\nabla\times m\,dr^3 \\ &= \iiint Dm\cdot\nabla\times m\,dr^3 \end{aligned} \quad (1.32)$$

1.3.1.4. Zeeman energy

When the ferromagnetic materials is under the external field, spins interacts with the external fields. The interaction between atomic spins and magnetic field is called Zeeman interaction. The Zeeman energy is expressed as

$$E_{Zeeman} = -\int \mathbf{M}\cdot\mathbf{H}_{ext}\,dV \quad (1.33)$$

1.3.2. The software for solving micromagnetic problem

There are a various software for solving micromagnetic problem. The software are classified into two groups by how to solve the differential equation : Finite difference method (FDM)-based software and finite element method (FEM)-based software. FDM and FEM are numerical methods for solving partial differential equations. FDM is a method by. Object Oriented Micro Magnetic Framework (OOMMF)

code [60] and mumax code [61] are a widely used micromagnetic software based on the FDM. Magpar [62] and Nmag [63] are a representative software based on the FEM. In this thesis, we employed mumax^3 and OOMMF to solve LLG equation based on the FDM. Especially mumax^3 calculates a spin dynamics using graphic processing unit (GPU) paralleling computing. That is, the rate of calculation is very fast compared to the CPU-based simulation code. As seen in Fig. 1.11, FDM used the rectangular grid to solve the differential equation and each cell includes a local magnetization.

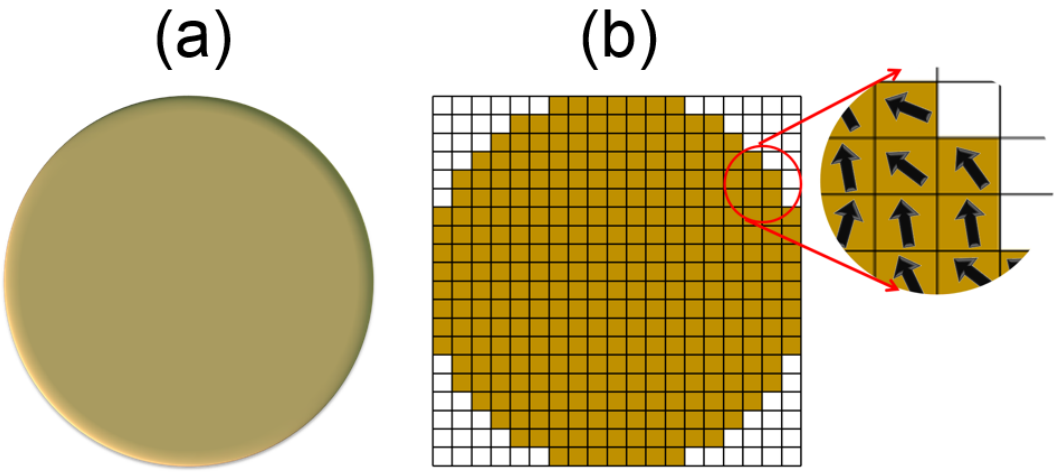

Figure 1.11 (a) a circular disk in real system. (b) A circular disk when FDM is employed. The each cell includes a local magnetization.

In this thesis, we choose a ferromagnetic materials as a $Ni_{80}Fe_{20}$ alloy, called Permalloy (Py). The following table shows the material parameters of Permalloy.

Table 1.1 The material parameters of Permalloy.

Material Parameters	Symbols	SI Units	cgs Units
Gyromagnetic ratio	γ	2.211×10^5 (m/As)	$2.8 \times 2\pi$ (MHz/Oe)
Saturation Magnetization	M_s	8.6×10^5 (A/m)	860 (emu/cm^3)
Exchange constant	A_{ex}	1.3×10^{-11} (J/m)	1.3×10^{-6} (erg/cm)
Damping constant	α	0.01	0.01
Cubic anisotropy constant	K_{c1}, K_{c2}	0 (J/m^3)	0 (erg/cm^3)
Interfacial Dzyaloshinski-Moriya constant	D	0 (J/m^2)	0 (erg/cm^2)
Bulk Dzyaloshinski-Moriya constant	D	0 (J/m^2)	0 (erg/cm^2)

2. Magnetic vortex structure in relatively thick circular disk

With increasing interest of 3-dimensional (3D) ferromagnetic element, the magnetic vortex formed in 3D system has been studied. In a circular disk, it is well-known that the magnetic vortex is no longer homogeneous along the thickness [64]. In this section, we shows an inhomogeneous magnetization of magnetic vortex structure with varying the thickness.

2.1. Thickness dependence of magnetic vortex structure

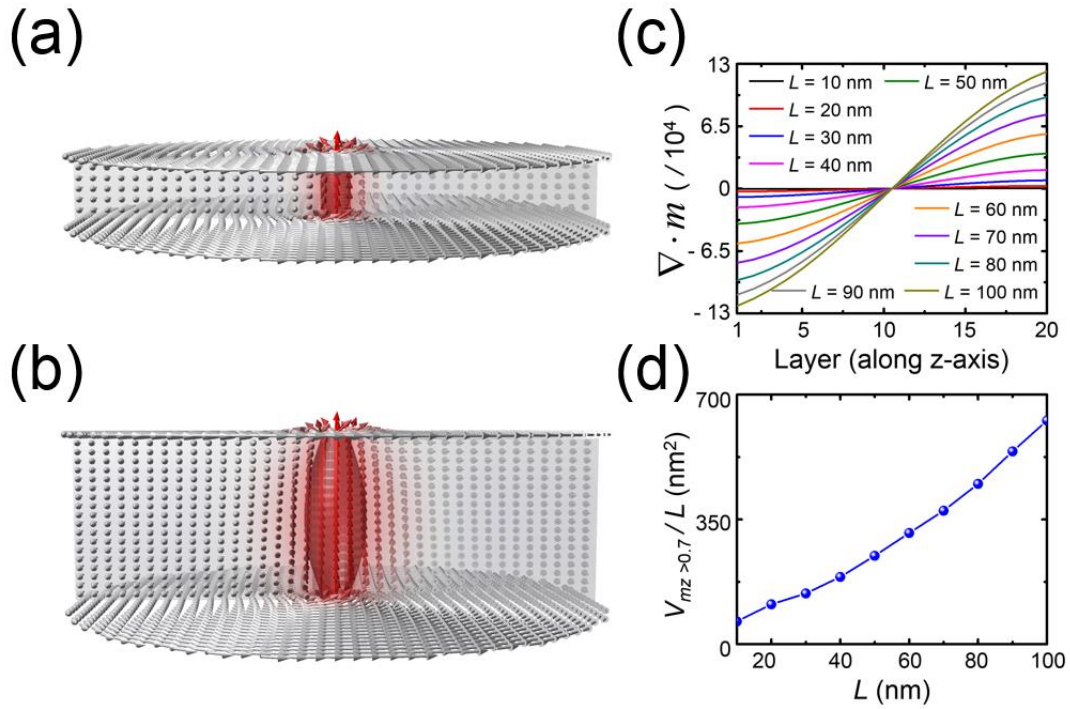

Figure 2.1 The cross section of magnetic vortex in the Py disk with diameter 300 nm when thickness L = (a) 40 nm, and (b) 100 nm. (c) First layer (bottom, Layer 1) to the final layer (top, Layer 20), the divergence of magnetization increases. In other words, in-plane magnetization is twisted. The degree of twist increases with thickness. (d) The plot of the vortex core size which is defined as the volume for $m_z > 0.7$ versus thickness.

It is well known that the magnetic vortex structure is not homogeneous along the thickness in 3D nanostructure [20,64]. In Fig. 2(a), as L increases, vortex core in the interior region is expanded and in-plane magnetization is twisted regardless of chirality. Fig. 2(b-c) shows the definite difference between the magnetization in the thin medium and thick medium. In the thin medium, the in-plane magnetization is a flux closure structure to reduce magnetostatic energy and it results in zero value of the divergence of in-plane magnetization. For example, as seen in Fig. 2(b), the divergence is nearly zero and the gradient of divergence is also nearly zero. However, there are large gradient of magnetization when L = 100 nm. It shows definitely twist of magnetization. Furthermore, the volume of $m_z > 0.7$ per thickness

increases, i.e, the size of vortex core increases with L.

3. Magnetic vortex dynamics

It shows that magnetic vortex in three dimensional nanostructures has a rich variety of the dynamics compared to that in two dimensional nanostructures. Furthermore, it is reported flexure oscillations of the vortex core with higher order frequency along the disk thickness in a relatively thick circular disk, elliptical disk, and prism [18-22]. However, the understanding the dynamics of magnetic vortex formed in thick circular disk is insufficient yet.

3.1. The variation of eigenfrequency of magnetic vortex gyration

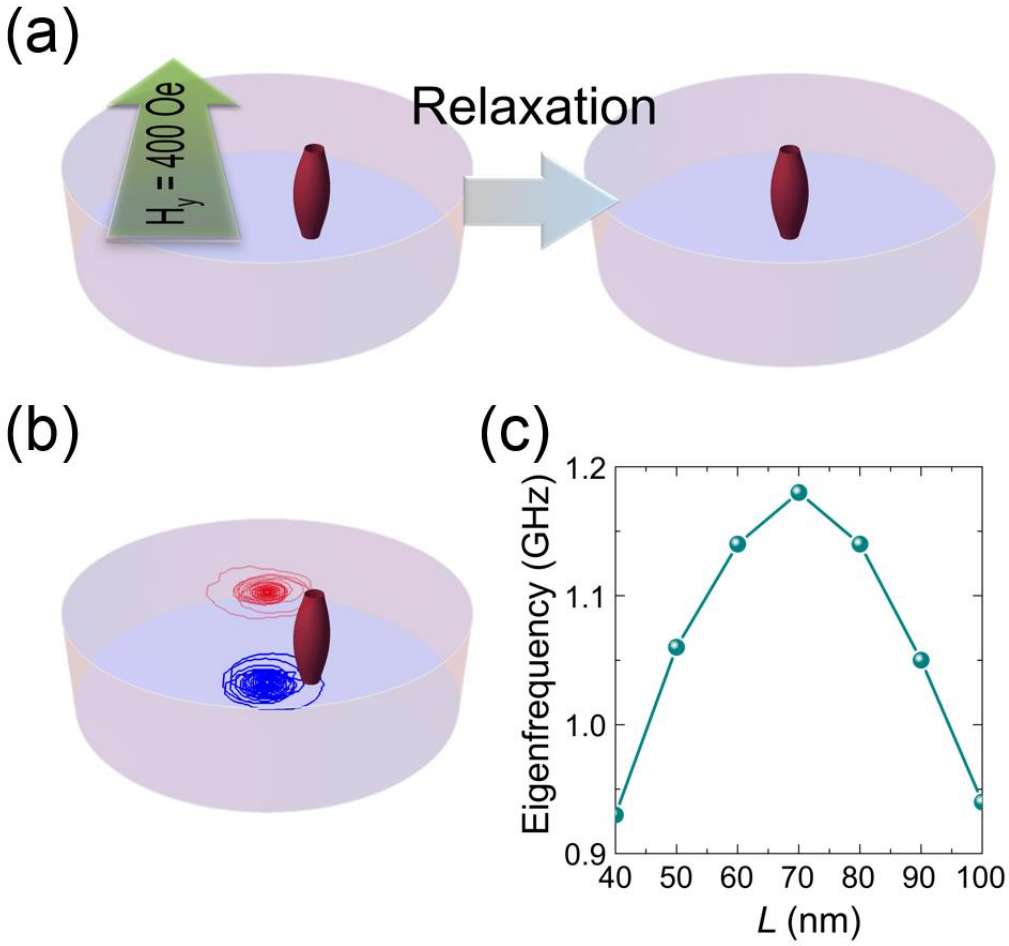

Figure 3.1 (a) The shifted vortex core returns to the center of the disk when 400 Oe static magnetic fields is turned off. (b) The trajectory of vortex core on the top and bottom layer. From Fast Fourier Transformation (FFT) using the x coordinate of vortex core, (c) the eigenfrequency versus thickness *L* plot is drawn.

Based on the Thiele's approach, the eigenfrequency of magnetic vortex structure is linearly increased with thickness of a circular disk. However, this results is just corresponded to thin circular disk. Basically, In Thiele's approach, it is assumed that the magnetic vortex structure is homogeneous along

the thickness and it result in the mismatch between the Thiele's approach and numerical simulation results. In order to calculate the eigenfrequency of magnetic vortex with varying the thickness, we applied a static magnetic fields along a positive y direction and it makes the shift of vortex core along x direction. Then, the applied magnetic fields is immediately released to zero. It result in the gyrotropic motion and then vortex core goes to the center of disk. Through Fast Fourier Transform (FFT) of x-component of vortex core, we obtained Fig. (c) and it allows previous well-known trends with varying the thickness [18,29].

3.2. Vortex dynamics under rotating magnetic field

In relatively thin disk, the magnetic vortex is specified by the rotating magnetic fields. A linearly oscillated fields is a superposition of two rotating magnetic fields. One has a counterclockwise rotating sense and the other has a clockwise rotating sense [65]. A counterclockwise (clockwise) rotating magnetic fields shows a resonance with a magnetic vortex with p = +1 (-1) regardless of the chirality. Accordingly, we specified the dynamics of magnetic vortex using a rotating magnetic fields.

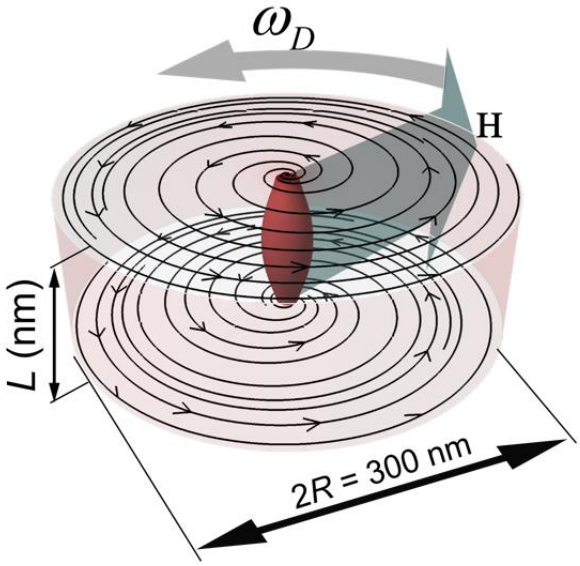

Figure 3.2 The schematic image of a Py circular disk under a counterclockwise rotating fields with eigenfrequency for gyrotropic mode. The red surface indicate the boundary for m_z >=0.7 and the streamline shows in plane magnetization. That is, the initial magnetization is the magnetic vortex with p = +1 (upward core direction) and c = +1 (counterclockwise circularity of in-plane magnetization).

We used micromagnetic simulator, mumax^3 code [61], to study the thickness dependence of the dynamics of magnetic vortex, which is based on the Landau Lifshitz Gilbert (LLG) equation, $d\mathbf{m}/dt = -|\gamma_L|[\mathbf{m}\times\mathbf{H}_{eff}]+\alpha[\mathbf{m}\times(d\mathbf{m}/dt)]$, where $\gamma_L = \gamma/(1+\alpha^2)$. It describes the dynamic motion of normalized magnetization, $\mathbf{m}$, with the gyromagnetic ratio, γ, the effective field, $\mathbf{H}_{eff}$, the saturation magnetization, M_s, the Gilbert damping constant α. As a model system, we considered a Permalloy (Py, $Ni_{79}Fe_{21}$), circular disk of $2R$ = 300 nm diameter with varying the thickness L and it is presented in Fig. 3.2(a). The initial magnetization of Py circular disk is the magnetic vortex which has the upward out-of-plane magnetization, corresponding to polarity p = +1 with chirality c = +1 represented by a counterclockwise (CCW) in-plane curling magnetization. In order to excite magnetic vortex, we applied a CCW rotating magnetic fields of the eigenfrequency for gyrotropic mode $\mathbf{H}=H_0[\cos(\omega_D t)+\sin(\omega_D t)]$. An unit cell size which our system used is 2 × 2 × 5 nm^3.

3.2.1. A phase and gyro-radii of vortex core gyration

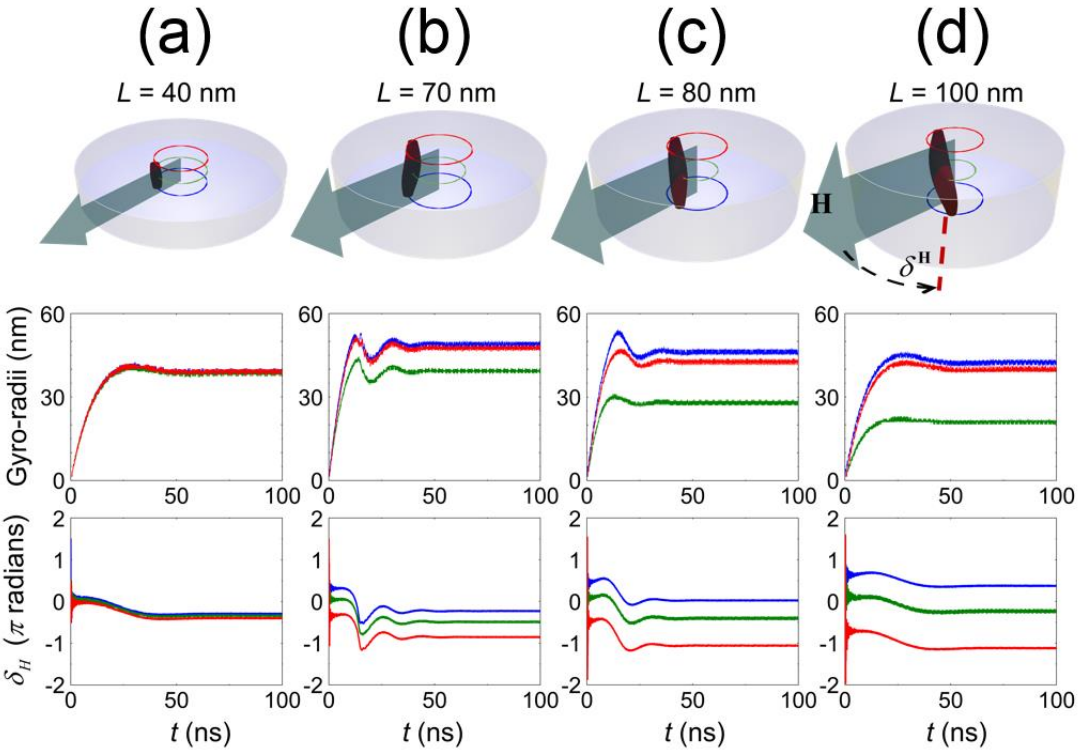

Figure 3.3 The micromagnetic simulation results as the thickness L of circular disk is (a) 40 nm, (b) 70 nm, (c) 80 nm, and (d) 100 nm when the field amplitude H_0 is 10 Oe. First row shows the snapshot of magnetic vortex dynamics under counterclockwise rotating magnetic fields. As seen in (d), $\delta^{\mathbf{H}}$ means the phase difference between the vortex core and the rotating magnetic fields. Second and third row show the time evolution of gyro-radii and $\delta^{\mathbf{H}}$. Red (Blue) color means that of vortex core on the top (bottom) surface and green color means that of vortex core on the middle layer.

As reported earlier, the vortex core with p = +1 is excited by counterclockwise rotating magnetic fields with eigenfrequency and show the gyrotropic motion where the trajectory is exactly circular shape [65,66]. Similarly, our results show the circular trajectories of vortex core regardless of the thickness. As seen Fig. 3.3(a), the resultant data (when L = 40 nm) is the same as aleardy reported works [65]. The magnetic vortex is rarely deformed and their phase difference $\delta^{\mathbf{H}}$ is almost homogeneous along the thickness with keeping its structure. However, Fig. 3.3(b)-(d) show the definte difference compared to reported works. During the gyrotropic motion, the magnetic vortex undergoes the dynamic deformation and then it causes non-uniform $\delta^{\mathbf{H}}$ along thickness although the vortex dynamics is performed in the perfectly circular disk, not in elliptical disk or prism. That is, in the relatively thick disk, the magnetic vortex core is elongated and Interestingly, the gyro-radii is not uniform along the thickness [67]. When L = 70 nm (See Fig. 3.3(b)), the gyro-radii of vortex core on the middle layer is markedly small compared to that on the surface layer. Evenly, the difference of gyro radii between top and bottom

surface is observed when L > 70 nm (See Fig. 3.3(c), (d)). That is, it is not symmetric with respect to the middle layer. In our model system, the gyro-radii on the top layer is larger than that on the bottom layer and the phase at the top layer lags behind that at the bottom layer.

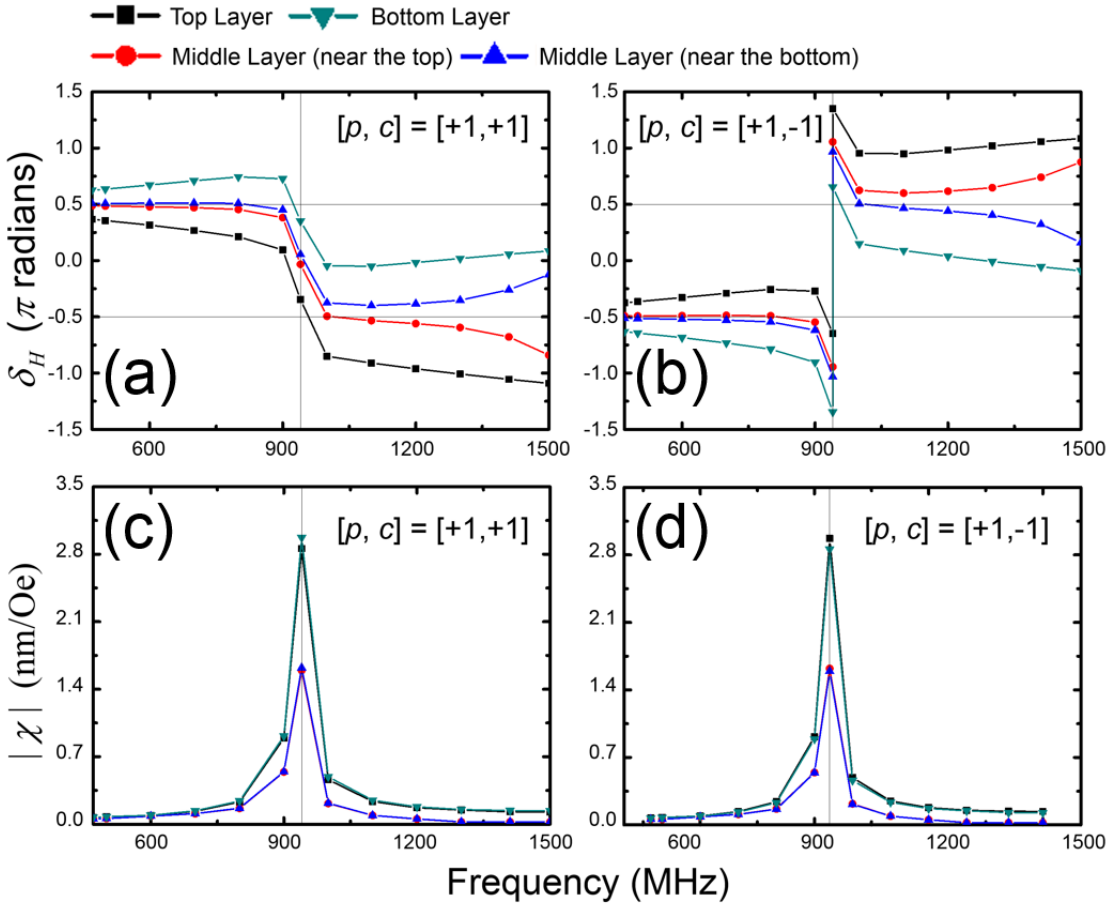

Figure 3.4 The dynamic properties when L = 100 nm. The phase difference $\delta^{\mathbf{H}}$ versus the fields when (a) c = +1 and (b) c = -1. The dynamic susceptibility χ versus the frequency of rotating magnetic fields when (c) c = +1 and (d) c = -1. All results is in the regime of linear dynamics of magnetic vortex. Black (Bluish green) line shows the properties of the top (bottom) surface and Red (Blue) line shows the properties of the middle layer near the top (bottom) surface. The grey vertical line shows the eigenfrequency of magnetic vortex.

To specify such penicular dynamics of magnetic vortex, we perform an additional simulation with changing the frequency of rotating magnetic fields and chiarlity of magnetic vortex when L = 100 nm. To analyze the simulation results, we calculate a dynamic susceptibility χ with satisfying the relation, position of vortex core $\mathbf{X} = \chi H_0$, and phase difference $\delta^{\mathbf{H}}$. The magnetic vortex with c = +1 shows a larger χ and $\delta^{\mathbf{H}}$ of the top layer than that of the bottom layer. This relation is reversed when c = -1. $\delta^{\mathbf{H}}$ is monotoncially increased (decreased) from the top (bottom) surface to the bottom (top) surface for c =

+1 (-1) while χ is the smallest at the middle layer. Accordingly, the chirality of magnetic vortex determines which surface the motion of vortex core is faster while it influences only the phase of magnetic vortex during the gyrotropic motion in thin nanoelement. Interestingly, $\delta^{\mathbf{H}}$ difference between top surface and bottom surface increases with the driving frequency of rotating magnetic fields. It imply the existence of the gyrotropic mode with higher mode as reported by *J. Ding et al* [18].

3.2.2. Vortex core reversal

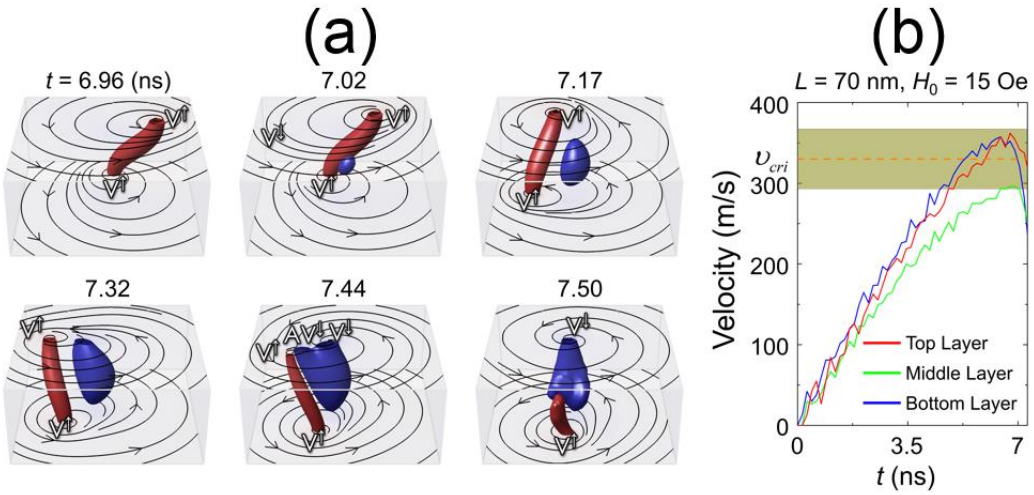

Figure 3.5 The vortex core reversal process when H_0 = 15 Oe and L = 70 nm. (a) The snapshot of the vortex-antivortex mediated reversal process. (b) The velocity of vortex core before the vortex core reversal.

Conventionally, through a resonant excitation with a rotating magnetic field, the vortex core reversals has been achieved. The magnetization dip with an opposite polarization to the original vortex core is nucleated next to the vortex core when the magnetic vortex. This magnetization dip is transformed into vortex and antivortex with the opposite polarization to the original vortex core. By combining generated antivortex with the original vortex, the original vortex is annihilated and new generated vortex remains [38,68-70]. Such vortex-antivortex reversals is achievable by moving Bloch point from the surface into the opposite surface [71]. This vortex core reversals process is achieved when the vortex core reaches the critical velocity [72]. *A Priori*, it has been believed that vortex core reversals process starts at the surface of the nanoelement and it ends the surface of the nanoelement. In other words, it is considered that the magnetization dip is nucleated at the surface.

However, we found that the magnetization dip is nucleated in the interior region in the disk, not at the surface, as seen in Fig. 3.5(a). A nucleated magnetization dip extends to the surface and it is divided into the vortex and antivortex at the surface. Consequently, the velocity of vortex core at the interior region is important for vortex core reversals rather than that at the surface. As seen in Fig. 3.5(b), vortex core reversals starts as soon as vortex core at the middle of the thickness reaches the critical velocity. It is attributable to the surface magnetostatic fields. The gyrotropic fields that is induced by the vortex core motion exerts throughout the thickness but the surface magnetostatic fields suppresses the nucleation of magnetization dip induced by the gyrotropic fields. That is, the nucleation of magnetization dip occur easily at the middle of the thickness. It seems that the magnetization dip is nucleated at the surface, but it is always nucleated at the middle layer. Accordingly, the velocity of

vortex core at the middle layer is important for vortex core reversals process.

3.2.3. Nonlinear dynamics

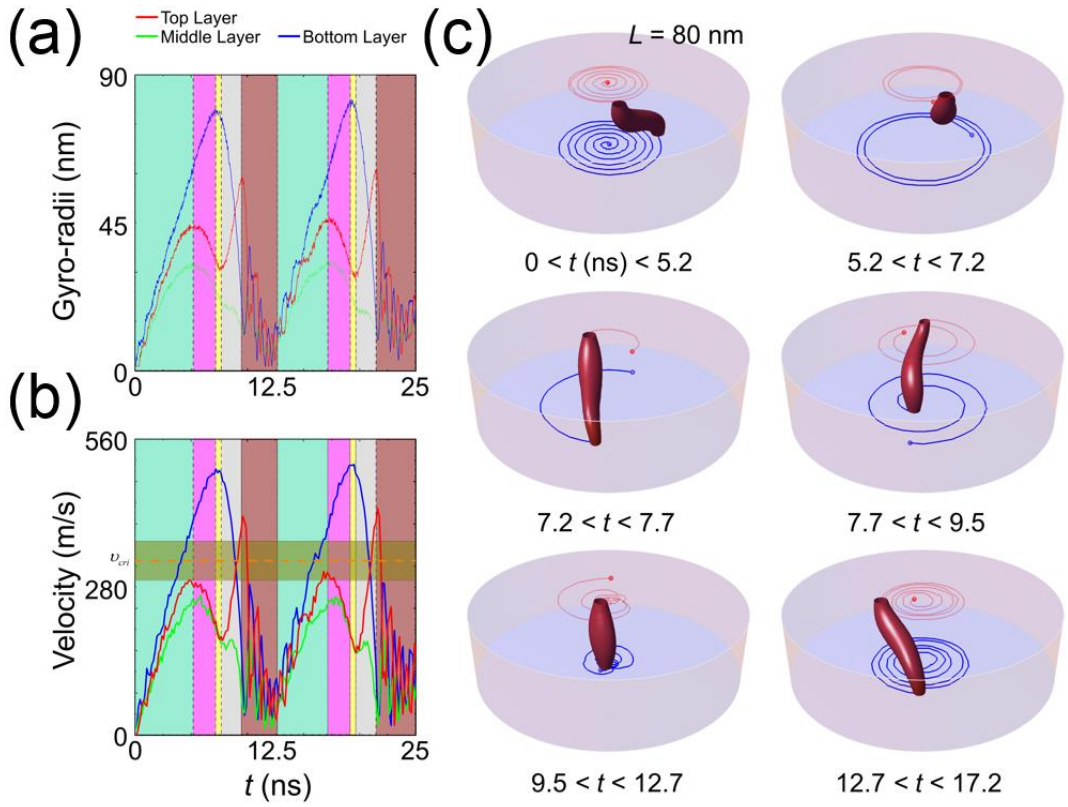

Figure 3.6 The nonlinear dynamics of magnetic vortex in a circular disk with L = 80 nm, and H_0 = 20 Oe. (a) The gyro-radii and (b) the velocity of vortex core are not constant. Each color in (a) and (b) means the individual dynamic regions and it is distinguished by boundaries for the sign of acceleration of vortex core on the top and bottom surface. The trajectories of individual regions is shown in (c).

It is well-known that the vortex core reversals can be achieved through resonant excitation as seen in Fig. 3.5. However, it is no longer achieved even though 20 Oe counterclockwise rotating fields with eigenfrequency is applied if L is larger than 70 nm. Instead, it shows a nonlinear peculiar dynamics. The gyro-radii, velocity and phase are not constant and show the complex oscillation. Fig. 3.6 shows a dramatic time-varying deformation of vortex core during the gyrotropic motion. Such nonlinear dynamics can be distinguished by the sign of acceleration of vortex core, *i.e.*, the time derivative of the velocity of vortex core.

Region I (bluish green)

Initially, both gyro-radii and velocity of vortex core on the top and bottom surface increase linearly. It is corresponded to the snapshot which shows the spiral-like trajectory of vortex core until time is smaller than 5.2 ns In Fig. 3.6(c). It is analogous to the transient motion of linear dynamics of magnetic vortex in a thin nanoelement.

.

Region II (magenta)

In this range, it is observed a non-linear dynamics, which cannot be observed in the linear dynamics. The gyro-radii and velocity of vortex core on the top surface decrease while those on the bottom surface increase continuously. Interestingly, the vortex core reversals does not occur although the velocity of vortex core on the bottom surface exceeds the critical velocity required for vortex core reversals in Py disk (~330m/s). The trajectories is shown in 5.2 ns < time < 7.2 ns in Fig. 3.6(c)

Region III (yellow)

After the vortex core reaches the maximum gyro-radii and velocity on the bottom surface, those are steeply decreased during about 0.5 ns. Those values on the top surface is still decreased.

Region IV (grey)

The gyro-radii and velocity of vortex core on the top surface increase steeply. In this region, on two surface, vortex core reaches the critical velocity required for vortex core reversals but it does not occur.

Region IV (brown)

Finally, the vortex core on the top surface goes to the center of disk with complex oscillation. Also, the vortex core on the bottom surface also undergoes the complex oscillation. This trajectory of vortex core is convoluted. Interestingly, the spin wave radiation along the azimuthal direction as soon as the vortex core on the top surface starts to return to the center of disk.

When the vortex core returns to the center, the vortex core starts the dynamics in region I again. That is, it is periodic. As presented in Section 3.2.2 (in the linear regime), the differences of phase and gyro-radii of vortex appear in relatively thick circular disk. Even, those properties is not symmetric with respect to the center of the vortex core. The vortex core is more elongated asymmetrically when the amplitude of rotating magnetic fields H_0 increases. Accordingly, the steep increase of such difference makes the vortex core not be able to maintain its structure. As a result, the dynamics corresponding to region II starts. Occasionally, the velocity of vortex core at the surface arrives much higher than the critical velocity while the velocity of vortex core at the middle layer is lower than the critical velocity.

3.2.4. Adiabatic and non-adiabatic process

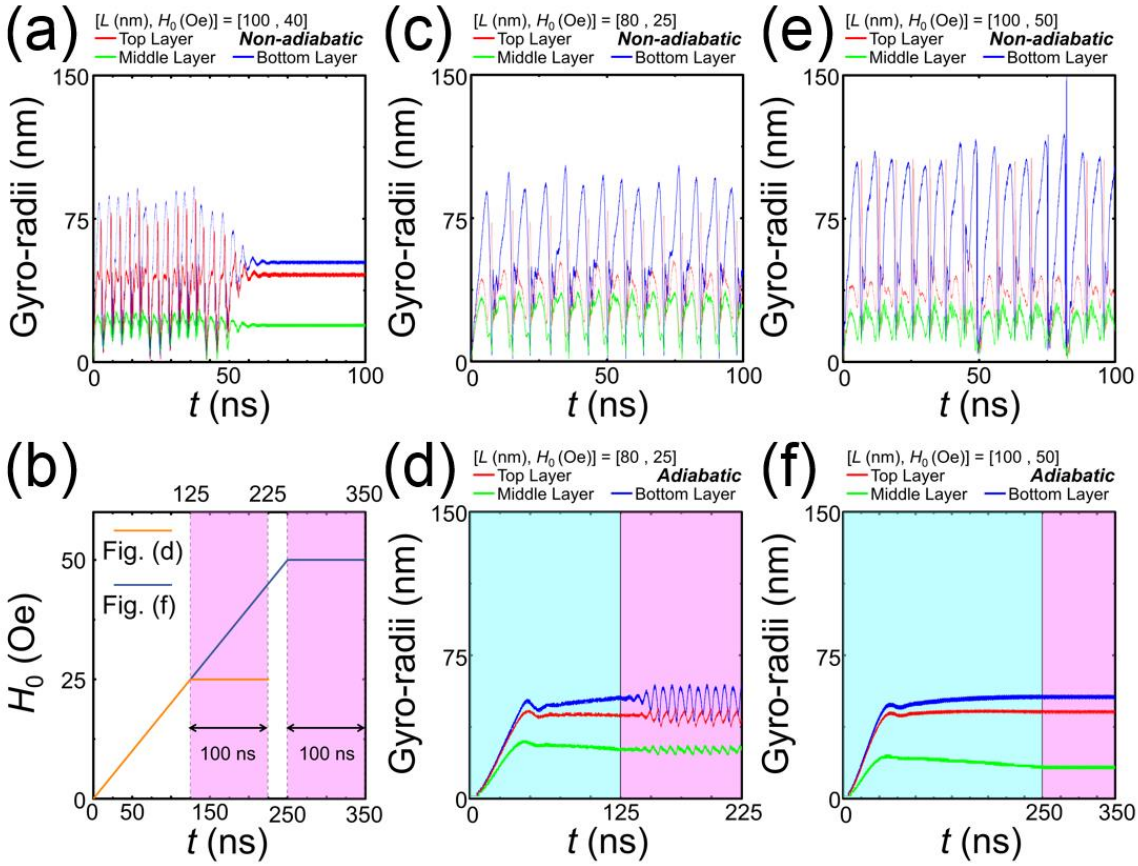

Figure 3.7 The gyro-radii when the amplitude increases (a), (c), (e) non-adiabatically and (d), (f) adiabatically in the circular disk with (c-d) L = 80 nm, and (a), (e-f) 100 nm. The amplitude H_0 is following : (a) 40 Oe, (c-d) 25 Oe, and (e-f) 50 Oe. Fig. (b) shows the time evolution of amplitude H_0 to mimic an adiabatic process. Initially, H_0 increases with a gradient 0.25 Oe / ns and at the 25 Oe (50 Oe), H_0 is fixed at the Fig. (d) (Fig. (f)).

Interestingly, Fig. 3.7(a) shows that the nonlinear dynamics of vortex core goes to the linear dynamics. That is, the nonlinear dynamics may be just a transient regime. Accordingly, it may be resulted by the steep deformation of vortex core. To specify it, we makes the amplitude of rotating magnetic fields be increased linearly and this amplitude is fixed when it reaches the amplitude we want (See Fig. 3.7(b)). Two dynamics between the adiabatic increasing and the non-adiabatic increasing of the amplitude of rotating magnetic fields shows a completely different dynamics. In case of non-adiabatic process, it shows the results corresponding to the nonlinear dynamics in Fig. 3.6. However, the non-adiabatic process does not show the nonlinear dynamics (See Fig. 3.7(f)). Each colors mean the linearly increasing amplitude region (magenta) and the fixed amplitude region (cyan). The gyro-radii reaches a critical gyro-radii and it decreases in the region which colored in magenta. In the region colored in cyan, the circular disk with L = 80 nm under 25 Oe rotating magnetic fields show that the vortex core does

not return to the center of the disk regardless of the surface but the gyro-radii shows the oscillation at the specific frequency as seen in Fig. 3.7(d). Even, the vortex in the circular disk with L = 100 nm under a rotating magnetic fields with H_0 = 50 Oe, it shows the completely linear dynamics in Fig. 3.7(e) although non-adiabatic process makes the tearing up a vortex core, which we will mention in section 3.2.5, occurs. In other words, the non-adiabatic process makes the steep vortex deformation and it results in the nonlinear dynamics. However, this nonlinear dynamics occurs when amplitude H_0 is too large to maintain the vortex elongation regardless of adiabatic or non-adiabatic process.

3.2.5. Tearing up vortex core at the surface layer

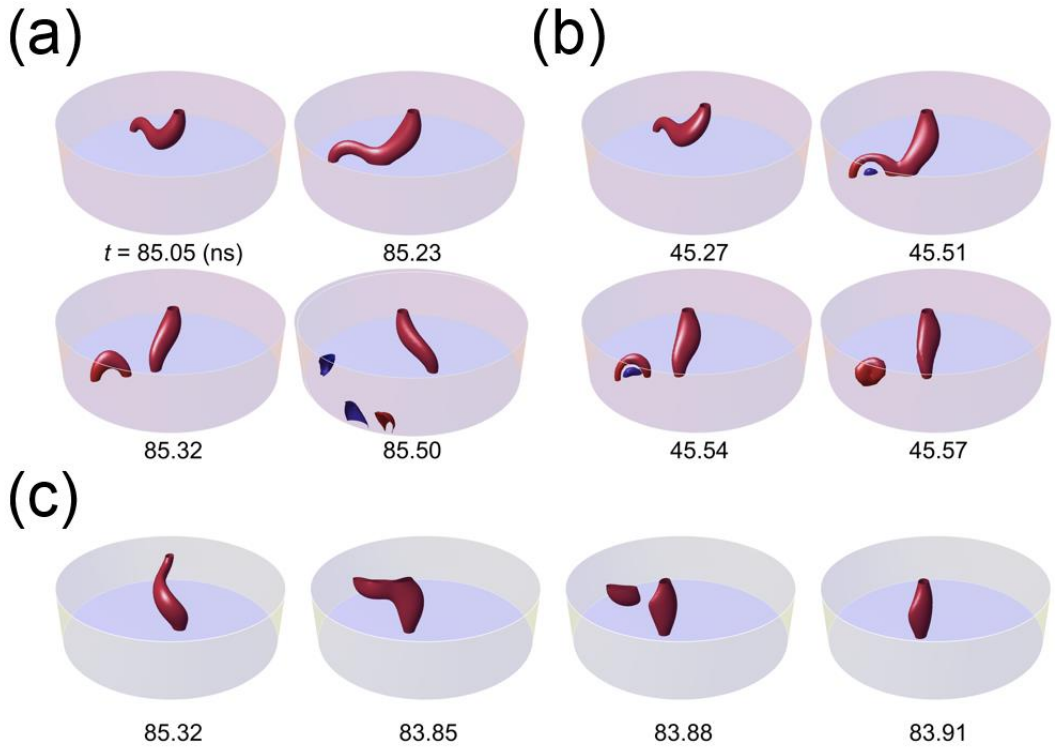

Figure 3.8 Two types of tearing up a vortex core at (a-b) the bottom surface and at (c) the top surface. At the bottom surface, the torn vortex core (vortex tube structure) is annihilated by (a) the collision with the edge and (b) combination with new nucleated non-zero m_z.

In the nonlinear dynamics, the velocity of vortex core is steeply is changed in the boundary between the region 2 and region 3 (boundary 2-3) and between the region 4 and region 5 (boundary 4-5) (regions are marked in Fig. 3.6). In these boundaries, as increasing H_0, the tube-shaped structure, which is called vortex tube structure in this thesis, was pulled out from the original vortex core as seen in Fig. 3.8. At the boundary 2-3 (4-5), the acceleration of vortex core is changed from positive value to negative value steeply at the bottom (top) surface and it causes the tearing up a vortex core. That is, the strong acceleration difference between two regions makes the nucleation of a vortex tube structure. It is not stable structure and it disappears while moving or when it collides with the edge of the disk with spin wave radiation at the top surface as seen in Fig. 3.8(c). However, at the bottom surface, it is not annihilated while moving but it is destroyed by collision with the edge of the disk and combination with new nucleated non-zero m_z in Fig. 3.8(a-b).

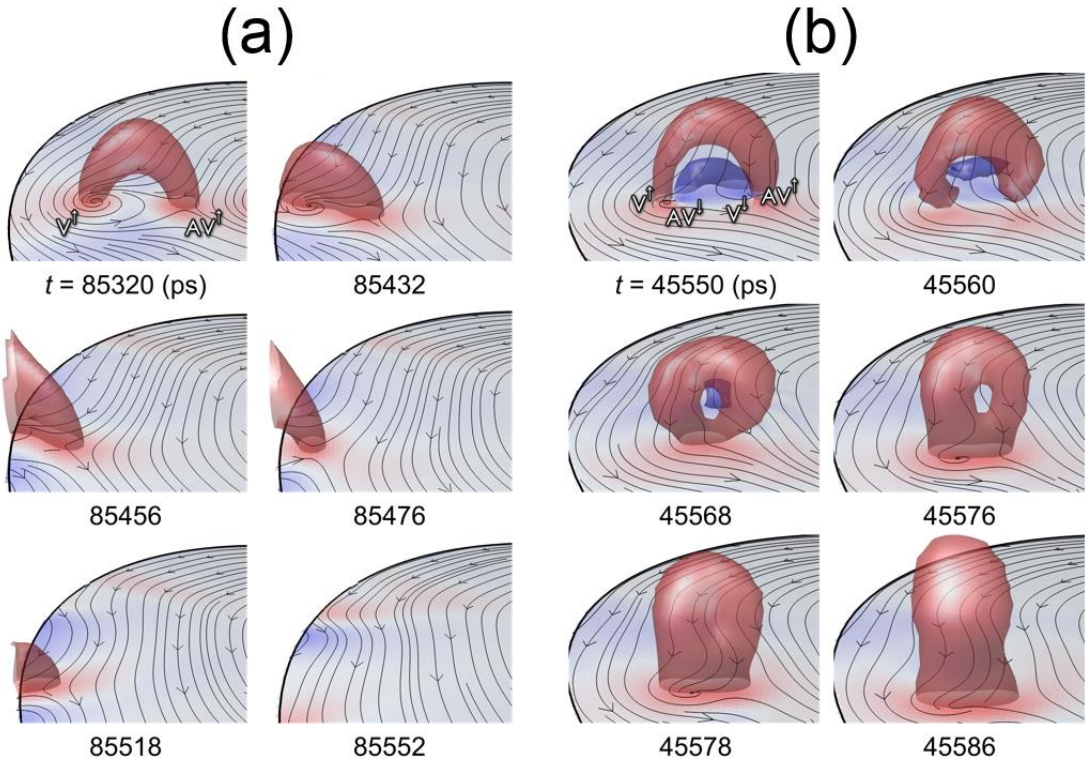

Figure 3.9 At the bottom surface, the annihilation process of vortex tube by (a) the collision with the edge of disk and the combination with non-zero m_z which consists of vortex-antivortex pair.

As seen in Fig. 3.9, the vortex tube structure connects to the vortex-antivortex pair at the surface. We approaches such vortex tube structure topologically. The magnetic vortex and magnetic antivortex is considered as a topological singularity with winding number, one of a topological number, n = +1 and -1. It has a half integer skyrmion number, another topological number, $q = np/2 = \pm 1/2$ and its sign is dependent on the polarity p. In Ref. [71], in three-dimensional system, this skyrmion number q is dependent on whether the vortex is in the top surface or the bottom surface (top surface : $-np/2$, bottom surface : $+np/2$) . That is, the total skyrmion number of a single vortex is zero due to it is connected between the top surface and the bottom surface. It is well-known that the winding number n is conserved during the vortex core reversals process. In case of the vortex tube structure, its n and p are zero. Thus, its creation and annihilation is trivial dynamic process with conserving the total topological number. As shown in Fig. 3.9(b), double vortex tube structure is also observed. Interestingly, additional vortex tube with opposite polarity appears just below the tube separated from the original vortex core. The additional vortex tube also connects with the surface vortex-antivortex pair. For conserving the total topological charge, the vortex is always annihilated with antivortex. Surprisingly, the vortex (antivortex) is always nucleated next to the original antivortex (vortex). Thus two tubes annihilate individually by vortex-antivortex annihilation process. Accordingly, during this process, the topological numbers are

conserved. That is, topologically dynamic trivial process being analogous to vortex core reversals (See Fig. 3.5). It is well-known that this process is accompanied with a single Bloch point. However, in this case, two vortex-antivortex annihilation process occurs simultaneously. In other words, Bloch point pair annihilates the vortex tube structure. Mainly, the vortex tube annihilation by Bloch point pair occurs mainly at the large H_0 compared to the vortex tube annihilation by the collision with the edge.

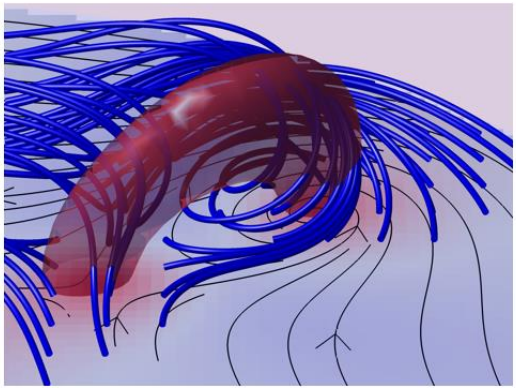

Figure 3.10 The three-dimensional image of vortex tube structure.

This ring-shaped structure consists of vortex-antivortex pair (See Fig. 3.9). The winding number, *n*, of vortex is +1 while *n* for antivortex is -1. Another topological number, skyrmion number *q* is *np*/2. That is, the winding number *n* and skyrmion number *q* of ring-shaped structure is zero. Interestingly, as seen in Fig. 3(b), the antivortex (vortex) of new ring-shaped structure is always next to the vortex (antivortex) of original ring-shaped structure. Being analogous to vortex core reversal process, the vortex (antivortex) is always annihilated by combining the antivortex (vortex). That is, both winding number and skyrmion number are conserved during the annihilation process of ring-shaped structure.

3.2.6. Phase diagram and criterion of tearing

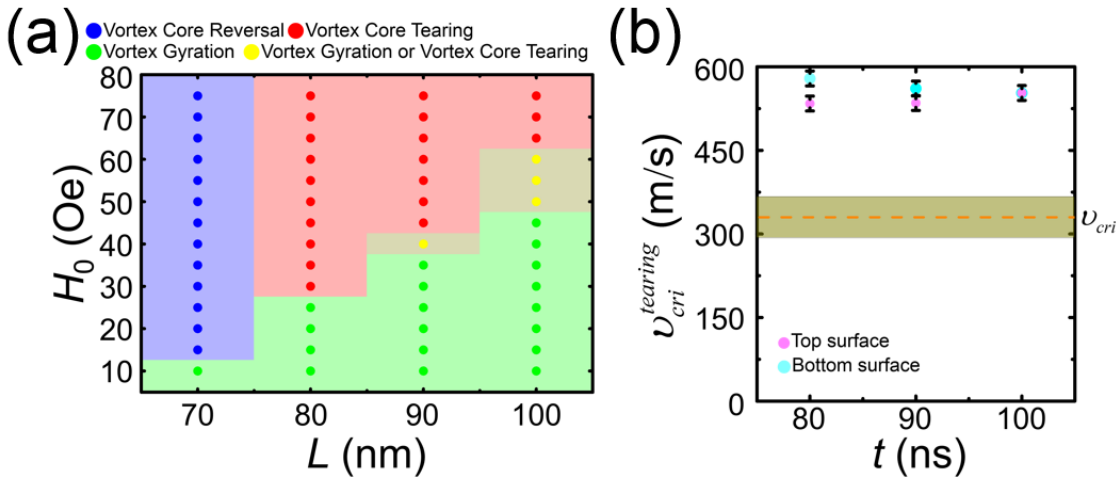

Figure 3.11 (a) The phase diagram of vortex dynamics with varying H_0 and L. The green region shows the non-linear and the linear gyrotropic motion of vortex core. The blue region means the vortex core reversals. The red color means the vortex core tearing. The yellow region means that the magnetic vortex shows gyrotropic motion in the adiabatic process and tearing up a vortex core in the non-adiabatic process. (b) The required velocity for tearing up vortex core at the top surface (magenta circle) and bottom surface (cyan circle). The region colored in yellowish green in Fig. (b) is a critical velocity required for vortex core reversals in Py disk.

Finally, we drew a phase diagram of vortex dynamics with varying L and H_0 until the simulation time is 100 ns in Fig. 3.11(a). As $L \leq 70$nm, the well-known dynamics, which have been reported, is shown. For relatively low H_0, As $L \geq 80$ nm, vortex core shows linear or non-linear gyrotropic motion. We cannot define the critical amplitude of rotating magnetic fields because vortex core moving nonlinearly sometimes returns the linear dynamics (See .3.7(a)). We found that the H_0 of rotating magnetic fields for tearing up vortex core for L = 80 nm, 90 nm, and 100 nm, are 30 Oe, 40 Oe, and 50 Oe. However, in adiabatic process, the nonlinear dynamics which is required for dynamic tearing up vortex core is prevented. That is, the critical H_0 is changed. The critical amplitude of rotating fields for tearing up vortex core, when L= 90 nm, and 100 nm, increases to each 45 Oe, and 65 Oe. In fact, non-linear dynamics doesn't appear until the amplitude reaches the critical amplitude in adiabatic process.

To specify the criterion for the tearing up a vortex core, we tried to find the critical velocity for tearing up a vortex core and result is in Fig. 3.11(b). Its value is larger than 500m/s regardless of which surface is. That is, the critical velocity required for tearing up a vortex core is much larger than the critical velocity required for the vortex core reversals.

3.3. Vortex dynamics under out-of-plane dc spin-polarized current

Among a lot of spintronic technology, the current-induced spin dynamics has a lot of attention for developing the spintronic device such as racetrack memory, skyrmion based racetrack memory. The electrical current makes the spin-transfer torque (STT) on the local magnetization to conserve an angular momentum. A combination of STT and vortex makes the vortex core switching and compensation for the dissipation of gyrotropic motion. That is, it is proposed to develop the vortex based spin torque oscillator. Accordingly, the current-induced dynamics is a reliable mean of specifying the magnetic vortex. For instance, the current-driven gyrotropic motion of magnetic vortex and vortex core reversals in confined magnetic nanoelement have been observed both experimentally, numerically and analytically [11,12,38,73-77]. Despite a several studies employing the STT effect on such vortex excitations, most of studies manipulate the magnetic vortex which has a uniform profile along the thickness of disk. However, in relatively thick circular disk, the out-of-plane current dynamics may be expected that it shows a different dynamics due to non-uniform magnetization along thickness. Furthermore, there are a deficient study of the effect of Oersted fields, which is another effect of the electrical current. In this section, we deal with the effect of OH fields and STT in relatively thick circular dot and provides an understanding how the individual effects influences the gyrotropic motion and vortex core reversals.

In this study, we used a micromagnetic numerical simulation code, mumax[3]. We employed a model system composed of an isolated permalloy (Py, $Ni_{80}Fe_{20}$) disk of $2R$ = 300 nm diameter and L = 80 nm thickness (See Fig. 3.12(a)). A perpendicular polarizer of the spin-polarization direction m_p = -1**,** which is a downward direction of magnetization, is positioned below the Py disk. Our system considered STT and a circumferential OH fields produced by an electrical current. The OH fields is plotted by using Biot-Savart law in Fig. 3.12(b). The mumax[3] code [61] calculated the Landau-Lifshitz-Gilbert equation and an additional STT term : $d\mathbf{m}/dt = -|\gamma_L|[\mathbf{m}\times\mathbf{H}_{eff}]+\alpha[\mathbf{m}\times(d\mathbf{m}/dt)]+\mathbf{T}_{STT}$, where $\gamma_{L=}\ \gamma/(1+\alpha^2)$, which describes the dynamic motion of normalized magnetization **m**, with the gyromagnetic ratio γ, the effective field $\mathbf{H}_{eff}$, the saturation magnetization M_s, the Gilbert damping constant α. The STT is given by $\mathbf{T}_{STT} = \mathbf{m}\times[\mathbf{m}\times(u\cdot\nabla)\mathbf{m}]+\beta\ \mathbf{m}\times(u\cdot\nabla)\mathbf{m}$ where $u = -Pj_e\mu_B/eM_s(1+\beta^2)$ where with non-adiabatic constant β = 0.04, the current density j_e, Bohr magneton μ_B, electron charge e, and the degree of spin polarization P = 0.5669. The electrical current always flows from top to bottom. The initial ground state of a magnetic vortex is the upward core magnetization corresponding to the core polarization p = +1. We deal with two in-plane curling magnetization of magnetic vortex, that is., counterclockwise (CCW, c = +1) and clockwise (CW, c = -1) direction. The unit cell size is 2 × 2 × 5 nm^3.

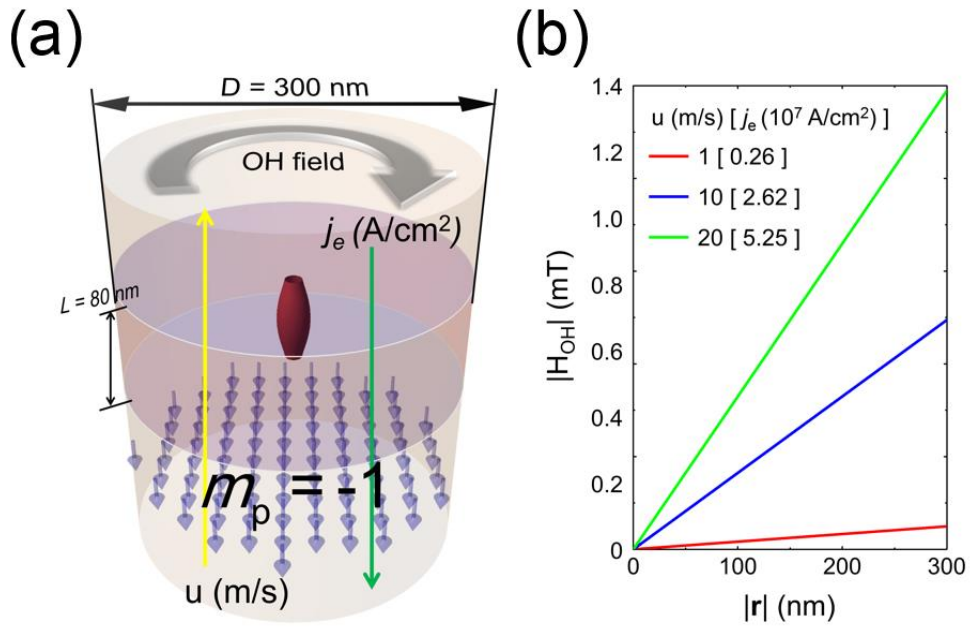

Figure 3.12 (a) The isolated magnetic vortex structure. (b) The strength of OH fields versus the distance **r** from the center of the disk.

3.3.1. The deformation of magnetic vortex core

When the thickness is small (L < 40 nm), the deformation of magnetic vortex by STT is a negligible due to the homogeneous magnetization along the thickness. However, the magnetic vortex is no longer homogeneous along the thickness when the thickness is large (L > 70 nm), as seen in Chapter 2. Thus we expected that there exists a large deformation of magnetic vortex by an electrical current. Using that the radial symmetry of magnetic vortex makes spend a lot of time showing gyrotropic motion when the vortex core is in the center of dot. Thus, we run the simulation which applies the out-of-plane spin-polarized current to the magnetic vortex during 20 ns to observe the deformation of magnetic vortex. We divided this section into following three parts. First part considered a pure STT and second part considered both STT and OH fields. Finally, it summarized the deformation of magnetic vortex by the electrical current.

3.3.1.1. The deformation of magnetic vortex core by a pure STT

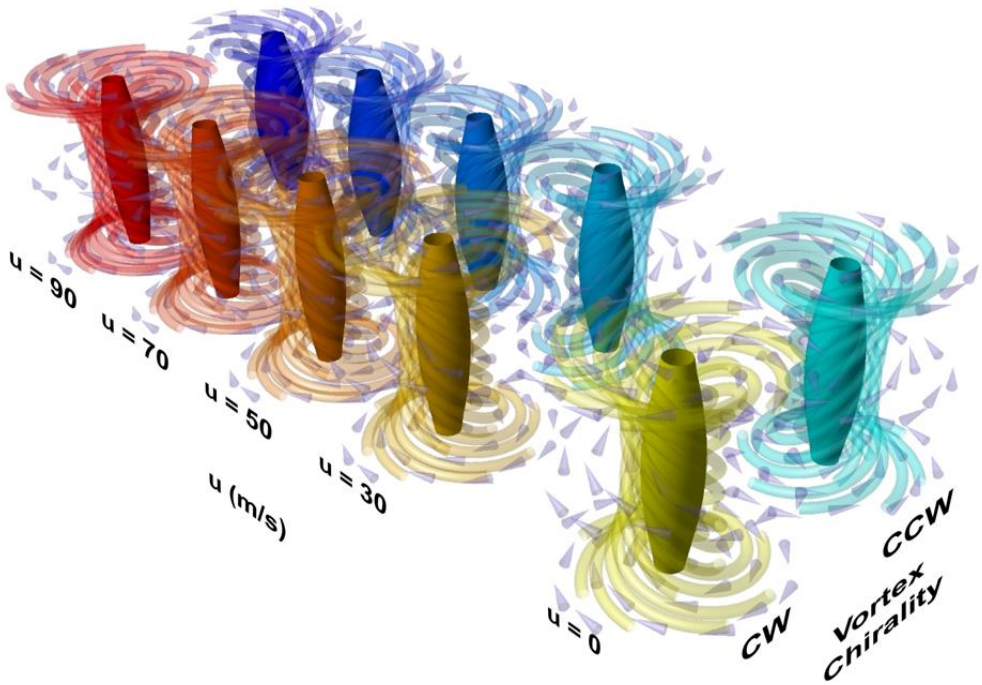

Figure 3.11 The deformation of magnetic vortex core structure at the center by the out-of-plane spin-polarized current. The spiraling tube and cone mean the in-plane magnetization of magnetic vortex. The convex-shaped surface is the boundaries for $m_z \geq 0.7$., *i.e., the vortex core.*

Originally, the volume of vortex core is independent of chirality. In other words, the volume of vortex core for c = +1 is the same as that of vortex core for c = -1. However, STT effect makes split those degenerated states by deforming the structure (See Fig. 3.11) in relatively thick circular disk unlike thin

nanoelement. In the case of vortex core for c = +1, the volume of vortex core is expanded and twist of in-plane magnetization increases when the current density increases. In contrast, the vortex core for c = -1 and STT make the volume of vortex core reduced and twist of in-plane magnetization decreases. In summary, the vortex core for c = +1 tends to be inhomogeneous along the thickness while the vortex core for c = -1 tends to be homogeneous.

3.3.1.2. The deformation of magnetic vortex core by a two effects : STT and OH fields

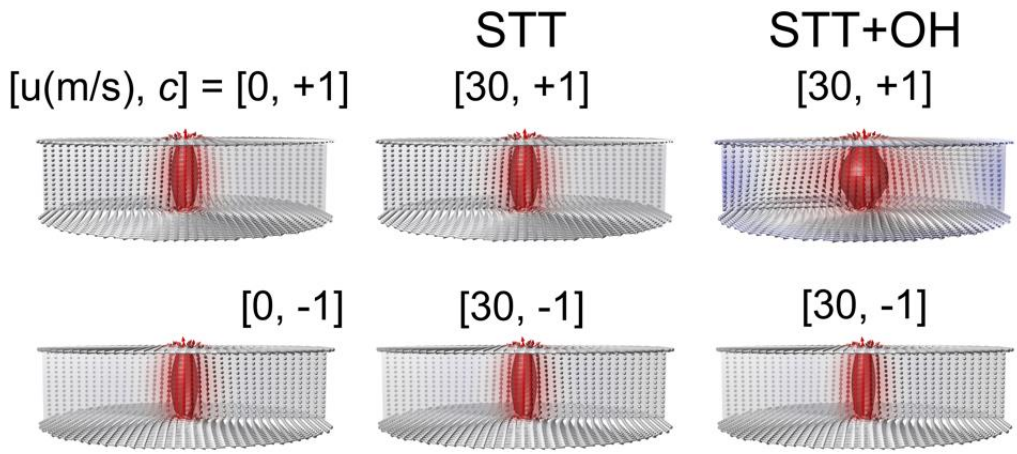

Figure 3.12 The schematic images of magnetic vortex. First column is the magnetic vortex when u = 0 m/s. A second and third column, the magnetic vortex structure considering only pure STT and both STT and circumferential OH field

We considered both the STT effect and OH fields. In our system, the rotating sense of OH fields is clockwise. Accordingly, in the presence of OH fields, Zeeman energy of the magnetic vortex for c = +1 is much larger than for the magnetic vortex for c = -1. Accordingly, OH fields makes the vortex core for c = +1 be homogeneous while the vortex core for c = -1 tends to be inhomogeneous. Interestingly, the degree of volume variation of vortex core induced by both STT and OH fields is much stronger than that induced by only pure STT.

3.3.1.3. Summary on the deformation of magnetic vortex induced by an electrical current

In order to consider all symmetries when the magnetic vortex is under a spin-polarized current, we changed the polarizer direction and initial polarization of magnetic vortex.

Table 3.1 The volume of vortex core when u = 30 m/s. Orange color means volume reduction and green color means volume expansion.

m_p	p	c	Core size (nm^3)	Core size (nm^3) [STT]	Core Size (nm^3) [OH]	Core Size (nm^3) [STT+OH]
+1	+1	+1	80640	78120	133560	112320
		-1		84600	68760	71100
	-1	+1		90405	133560	208665
		-1		73620	68760	64800
-1	+1	+1		90450	133560	208710
		-1		73620	68760	64800
	-1	+1		78120	133560	112320
		-1		84600	68760	71100

Based on the Table 3.1, STT makes the volume of vortex core expanded for $m_p pc$ = +1 while it is reduced for $m_p pc$ = -1. When considering only OH fields, the m_p and p is independent on the volume of vortex core. However, it is sensitively dependent on whether OH fields is parallel or antiparallel to the in-plane magnetization and it is originated from the rotational direction of spin-transfer torque. As a results, volume of vortex core is expanded for c = +1.

In conclusion, the competition between two effects determines the volume of vortex core. The effect of OH fields is dominant effect when u = 30 m/s.

3.3.2. Chirality dependence of vortex dynamics

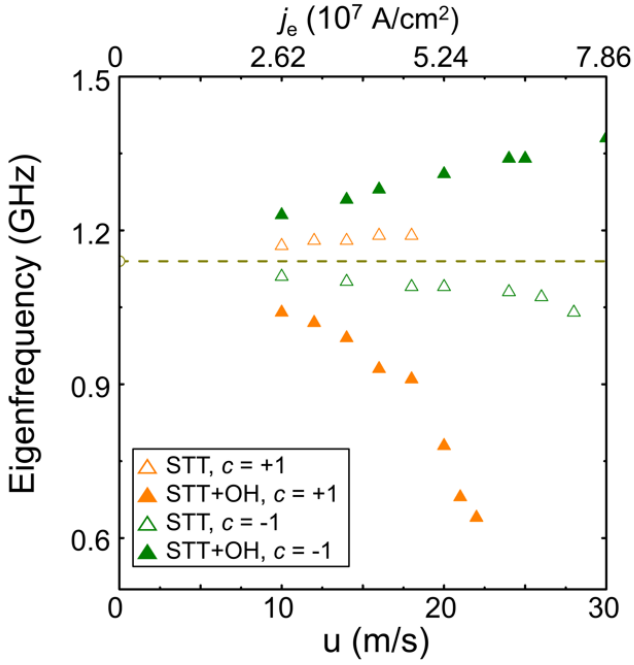

Figure 3.13 The shift of eigenfrequency of magnetic vortex when the out-of-plane spin polarized current is applied. At each point, the magnetic vortex shows the linear gyrotropic motion. An orange color and green color mean c = +1 and c = -1. The open triangle includes both STT and OH fields while the closed triangle does not consider the OH fields. The dotted line and open yellow circle is the eigenfrequency when there is no electrical current.

Generally, it is reported that under the out-of-plane spin-polarized current, STT does not influences the eigenfrequency of magnetic vortex but OH fields makes the shift of eigenfrequency of magnetic vortex [12,76]. To specify the eigenfrequency, we applied out-of-plane spin polarized current with the magnetic vortex which is shifted by 50Oe in-plane fields. However, Fig. 3.13 shows the change of eigenfrequency of only pure STT driven vortex. Whether the OH includes or not and whether c = +1 or -1 determine the shift of eigenfrequency and it is originated from the Section 3.3.1 which shows the degenerated magnetic vortex states are split by both STT and OH fields. Except the case considering both STT and OH fields with c = +1, the eigenfrequency is linearly increasing or decreasing. In case of considering only STT, the chirality of magnetic vortex determines whether eigenfrequency increases or decreases. However, the rate of eigenfrequency change is small compared to that considering OH fields. Also, OH fields makes the sign of the rate of eigenfrequency change be reversed. Interestingly, the magnetic vortex for c = +1 shows a unique dynamics such as nonlinear dynamics and tearing up a vortex core when u $\geq$ 20 m/s. However, OH fields suppressed this unique dynamics. Instead, it results in the large rate of eigenfrequency change compared to when u < 20 m/s. Such unique dynamics is described in 3.3.2.1 ~ 3.3.2.2 except the description of linear dynamics.

3.3.2.1. The magnetic vortex with clockwise (CW) in-plane magnetization

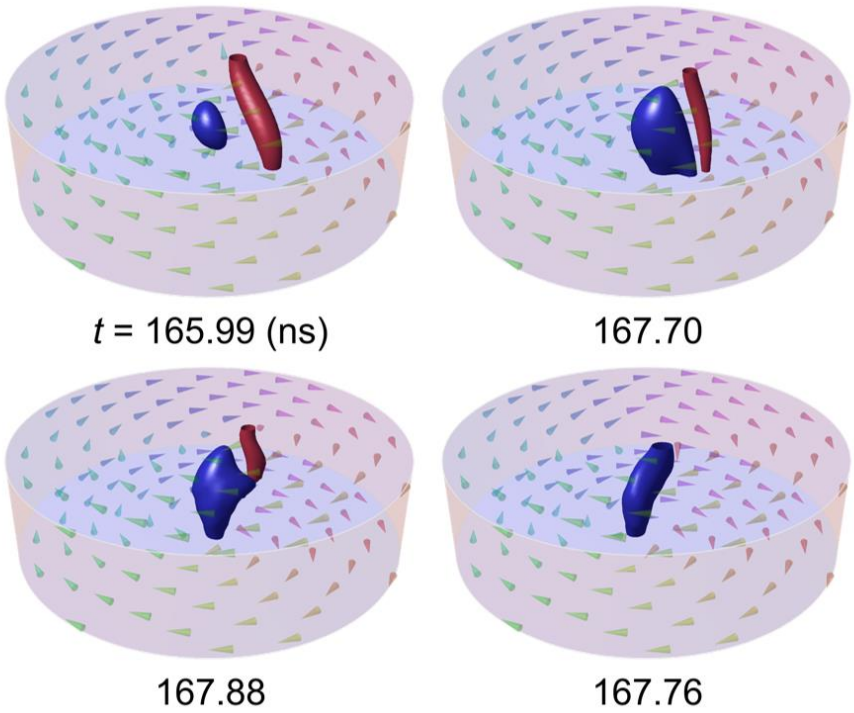

Figure 3.14 The vortex core reversals process when *c* = -1 and u = 30 m/s considering only STT.

In the previous chapter, we reported that the vortex core cannot be reversed by the rotating magnetic fields through the resonant excitation. However, this out-of-plane spin-polarized current can make the vortex core reversals through vortex-antivortex nucleation and annihilation regardless of existence of OH fields when *c* = -1. OH fields makes just the current required for vortex core reversal increased because Zeeman energy tends to suppress the gyrotropic motion of magnetic vortex. We found that the current required for vortex core reversals is larger than 30 m/s and smaller than 31 m/s in STT system while it is larger than 30 m/s and smaller than 40 m/s in STT system

At present, we think that there are two regions. One is related to size of vortex core and the other is related to the strong torque at the bottom surface. Both STT and OH fields make the vortex core for *c* = -1 shrunk. That is, both STT and OH makes vortex core be homogeneous along thickness. In other words, it is analogous to the magnetic vortex in the thin nanoelement. It may cause the vortex core reversals. Also, the magnetization is undergo strong torque by spin-polarized current due to a large spatial derivation of magnetization compared to the others. In the previous chapter, the gyro-radii of vortex core on the top surface is larger than that on the bottom surface. Furthermore, the vortex core on the bottom surface lag behind the vortex core on the top layer. However, the strong torque at the bottom surface decreases the phase difference and phase between top surface and bottom surface. It tends to make gyrotropic motion be homogenous along thickness.

3.3.2.2. The magnetic vortex with counterclockwise (CCW) in-plane magnetization

In case of c = +1, the existence of OH fields makes a completely different dynamics of magnetic vortex. In this section, we shows the description of non-linear dynamics driven by only STT and both STT and OH fields.

3.3.2.2.1 Consideration of only STT system

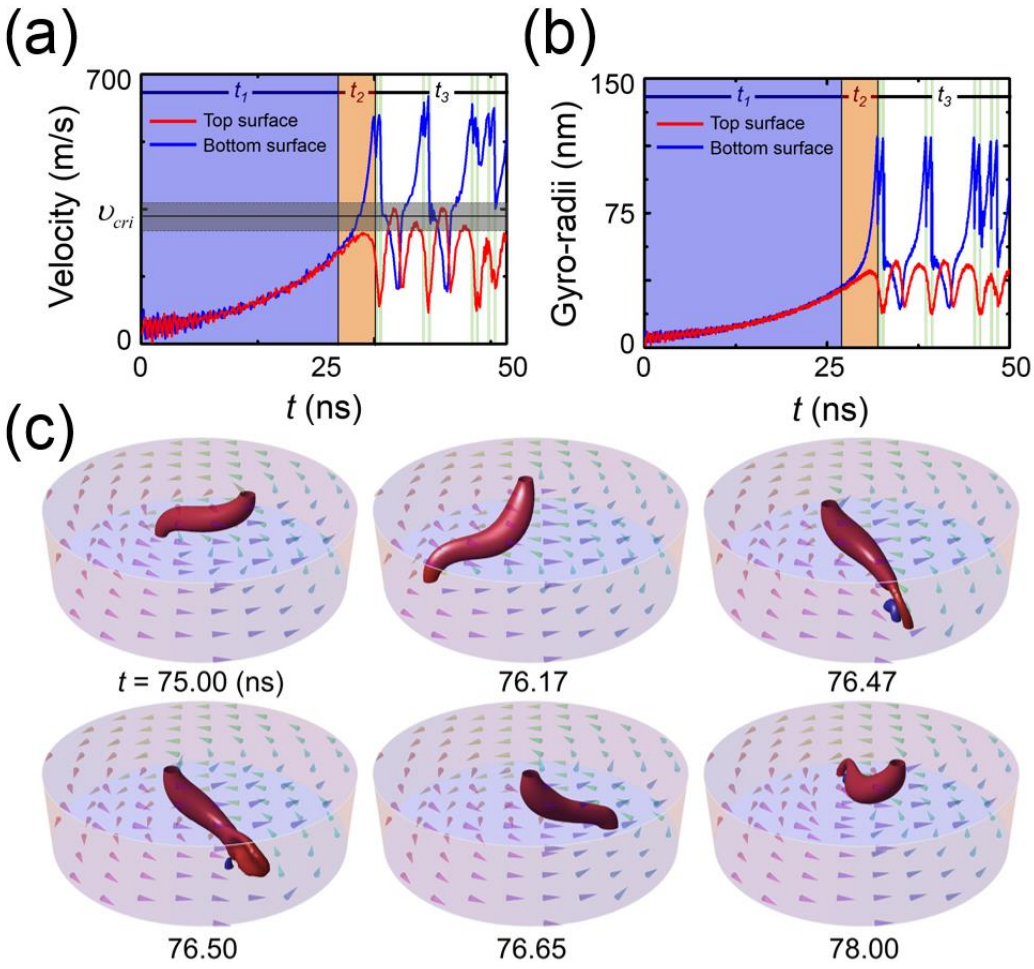

Figure 3.15 The nonlinear dynamics of magnetic vortex driven by only STT when c = +1 and u = 30 m/s. The time evolution of (a) velocity and (b) gyro-radii. The grey regions is the critical velocity required for vortex core reversals. The three regions t_1, t_2 and t_3 are divided by the vortex dynamics. (c) The snapshot of vortex dynamics in the region t_3 when u = 20m/s.

Interestingly, the magnetic vortex with c = +1 does not show the vortex core reversals. Instead, it shows the nonlinear dynamics similar to the vortex dynamics driven by rotating magnetic fields. However, this nonlinear dynamics is slightly different from rotating fields driven nonlinear dynamics. In the reported rotating fields driven nonlinear dynamics, it is divided into five regions and it is hard to analyze it due to complexity such as tearing up vortex core and for vortex core returning to the center

of disk. However, the STT driven nonlinear dynamics can be divided into three regions t_1, t_2 and t_3 as seen in Fig. 3.15(a-b). In the t_1 region, the magnetic vortex on the top and bottom surface shows spiral-like motion with increasing gyro-radii and velocity. However, there are no differences of gyro-radii and velocity between the top and bottom surface unlike the rotating fields driven nonlinear dynamics. In the region t_2, the differences of gyro-radii and velocity appear and its magnitude increases. Especially, at the bottom surface, both gyro-radii and velocity increase rapidly. As a results, in the region t_3 (See Fig. 3.15(c)), at the bottom surface, the vortex core is fluctuated by non-zero m_z being analogous to Fig. 3.9 of section 3.2.5. However, it is not pulled out and makes fluctuation with spin wave radiation. However, due to for the vortex core not returning to the center of the disk with increasing gyro-radii of vortex core at the top surface. This nonlinear dynamics occurs when $u \geq 20$ m/s

In contrast to the magnetic vortex with c = -1, the vortex core is expanded by the spin-polarized current. That is, it makes the magnetic vortex be more inhomogeneous along thickness. Accordingly, it may suppress the vortex core reversals. Also, previous mentioned strong spin-transfer torque on the bottom surface may prevent the vortex core on the top layer from large gyro-radii and velocity. As a results, the vortex core on the top surface is confined in the small area compared to the vortex core on the bottom surface.

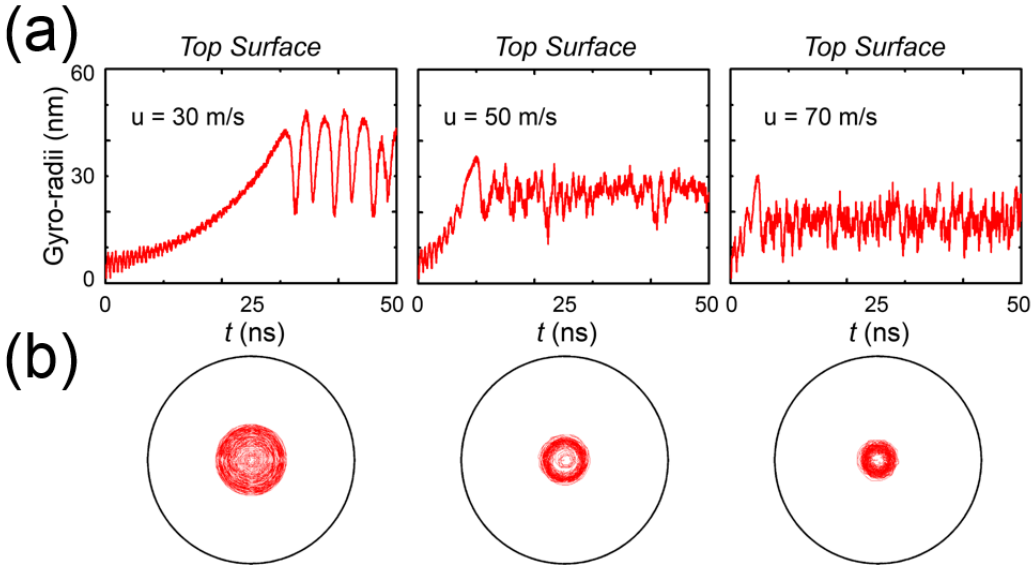

Figure 3.16 A time evolution of (a) gyro-radii and (b) trajectories of vortex core on the top surface. The trajectories means the vortex core position from 0 ns to 100 ns. Each column shows the dynamics when u = 30 m/s, 50 m/s and 70 m/s from the left side to the right side.

This confinement area of vortex core on the top layer is reduced with increasing the current density as seen in Fig. 3.16. However, the time to reach non-linear dynamics is reduced. As well as, the fluctuation increases with the current density.

3.3.2.2.2 Consideration of both STT and OH system

OH fields prevent the nonlinear dynamics induced by STT which occurs for when u ≥ 20 m/s. As u < 20 m/s, the shift of eigenfrequency decreases linearly versus the u value. However, the rate of eigenfrequency change is steeply increased at u = 20 m/s. That is, a strong magnitude of OH fields near the edge suppresses the fluctuation on vortex core on the bottom surface. When it shows gyrotropic motion, the vortex core is largely elongated compared to other systems and the vortex core is similar to the first snapshot of Fig. 3.18.

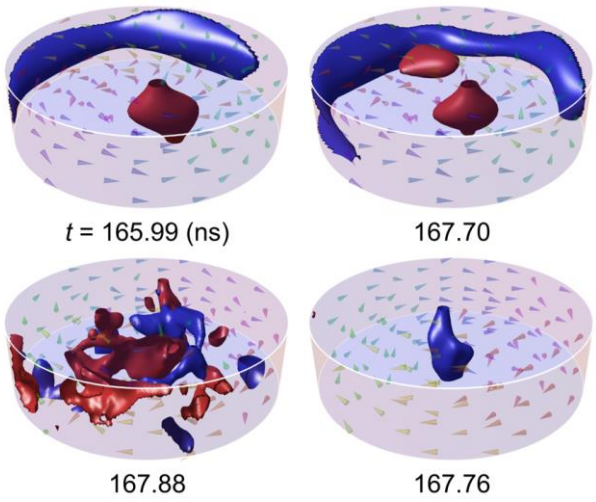

Figure 3.17 The snapshot of vortex core reversals process when u = 30m/s.

Interestingly, in STT + OH system, the vortex core reversals occurs in contrasts of only STT system as seen in Fig. 3.17 in contrast to the STT system. However, to achieve vortex core reversals, it is always accompanied with the chirality of magnetic vortex reversals. This chirality reversals is mediated by chaotic dynamics. That is, it is achieved through a very complex dynamics. However, although the magnetization direction of polarizer is downward along *z*-direction, the polarity reversals are determined by chaos and it cannot be reversed when the chirality is reversed.

As seen Fig. 3.18, the chirality reversals through the chaotic dynamics but the polarity reversals does not occurs in this process. The polarity reversals can be achieved by vortex-antivortex through gyrotropic motion. Although the vortex core reversals cannot be achieved when c = -1 and u = 24, strong torque induced by the chirality reversals makes the vortex-antivortex mediated vortex core reversals possible.

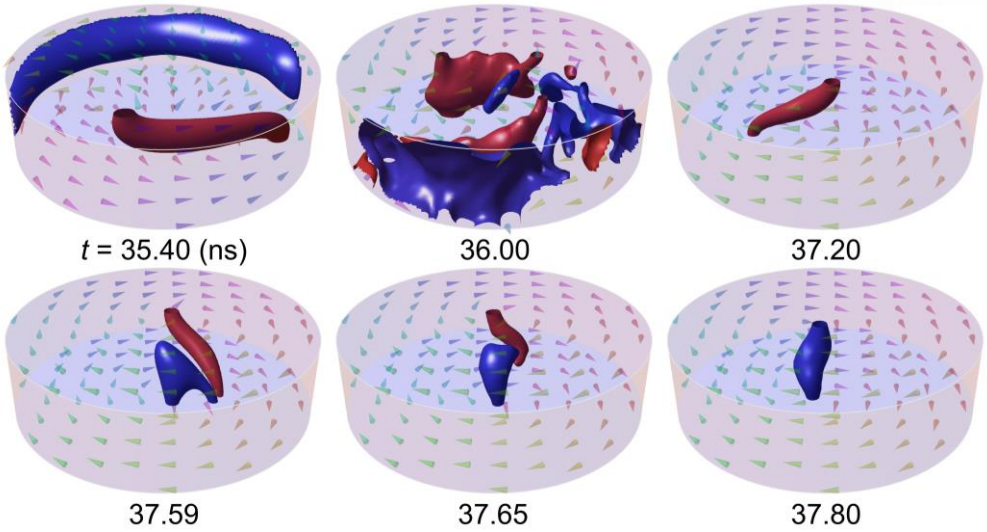

Figure 3.18 The snapshot of vortex core reversals process when u = 25m/s.

3.4. Vortex dynamics under alternating out-of-plane spin-polarized current

For controlling magnetic vortex states with low power, the resonant excitation with the dynamic mode, such as gyrotropic mode, azimuthal spin wave mode and radial spin wave mode, of magnetic vortex is necessary. It is well-known that the magnetic vortex core reversals can be achieved when the oscillating frequency of any driving forces is tuned to that mode's eigenfrequency [37-42]. Furthermore, ultrafast vortex core reversals have been attracted much attention on account of their possible implementation in information storage devices. However, in the relatively thick nanoelement, the vortex core cannot be reversed through the resonant excitation of gyrotropic mode using rotating magnetic fields. In the previous chapter, the dc out-of-plane spin polarized current can make a vortex core reversed. However, It spends a long time to reverse vortex core and the vortex core should be shifted by in-plane fields, fluctuation and defect for breaking radial symmetry. That is, in relatively thick nanoelement, another mode should be specified to find new dynamic mode. We report new high frequency mode, beating mode and higher-order-beating mode, which corresponded to the size oscillation of vortex core. Also, we address the beating-mode-assited vortex-core reversals, which differs completely from the familiar vortex-antivortex-pair-mediated mechanism .

We set the model system composed of a circular permalloy (Py, $Ni_{80}Fe_{20}$) disks of $2R$ = 300 nm diameter and L = 80 nm thickness and two polarizer using mumax[3] code which performs micromagnetic numerical simulation. One polarizer is positioned below the Py disk and the other polarizer is above the Py disk. In this simulation, both the spin transfer torque and Oersted (OH) fields are considerd, which is produced by an electrical current. We took into account both effects in all the simulations. The mumax[3] code [61] solves the Landu-Lifshitz-Gilbert (LLG) equation with spin-transfer torque : $d\mathbf{m}/dt = -|\gamma_L|[\mathbf{m}\times\mathbf{H}_{eff}]+\alpha[\mathbf{m}\times(d\mathbf{m}/dt)]+\mathbf{m}\times[\mathbf{m}\times(\mathrm{u}\cdot\nabla)\mathbf{m}]+\beta\mathbf{m}\times(\mathrm{u}\cdot\nabla)\mathbf{m}$, where $\mathrm{u} = -Pj_e\mu_B/eM_s(1+\beta^2)$ where with non-adiabatic constant β = 0.04, the current density j_e, Bohr magneton μ_B, electron charge e, and spin polarization P = 0.5669. Initially, we applied a sinc function out-of-plane spin-polarized current expressed as $\mathrm{u} = u_0\sin[\omega_H(t-t_0)]/[\omega_H(t-t_0)]$ with u_0 = 50 m/s, $\omega_H = 2\pi \times 50$ GHz, and t_0 = 1 ns to four type of model system during 10 ns to excite the intrinsic modes in the given disk (See Fig. 3.19). Then, through Fast Fourier Transformation (FFT), we obtained a peak corresponding a specific mode. The reason why the system is divided into four is to find optimized system which has a large FFT intensity. We applied out-of-plane sinusoidal current (designated as $\mathrm{u} = u_0\sin(\omega_D t)$) with a corresponding peak. We assumed that the current flows along a perpendicular direction to plane geometry and it flows uniformly through the entire Py disk (See Fig. 3.19). The initial ground state of a magnetic vortex composed of the upward core magnetization corresponding to the polarization p = +1 and the counterclockwise (CCW) in-palne curling magnetization, chirality c=+1. The unit cell size is 2 × 2 × 5 nm^3. Fig. 3.19 shows four initial states by varying the magnetization direction of polarizer.

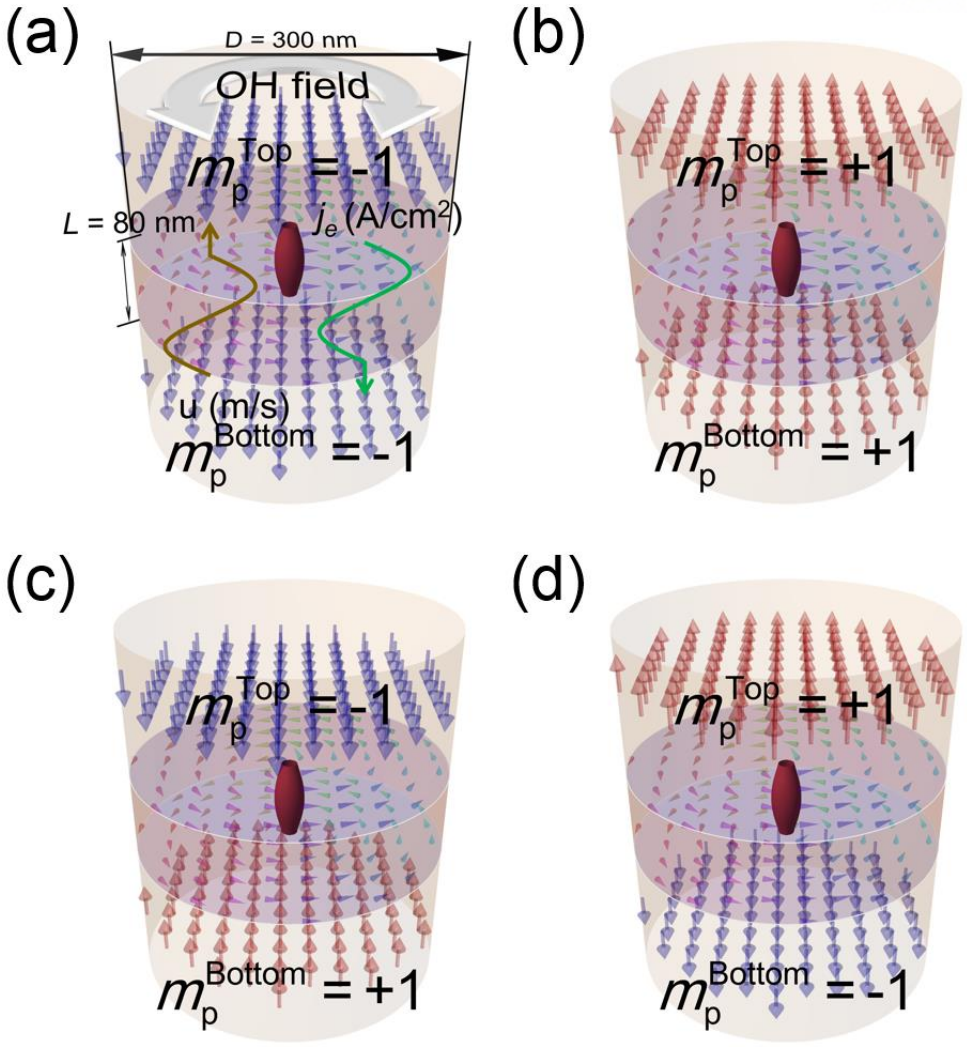

Figure 3.19 The four model systems. [m_p^{Top}, m_p^{Bottom}] = (a) [-1, -1], (b) [+1, +1], (c) [-1, +1], and (d) [+1, -1].

3.4.1. The eigenfrequency of a beating mode

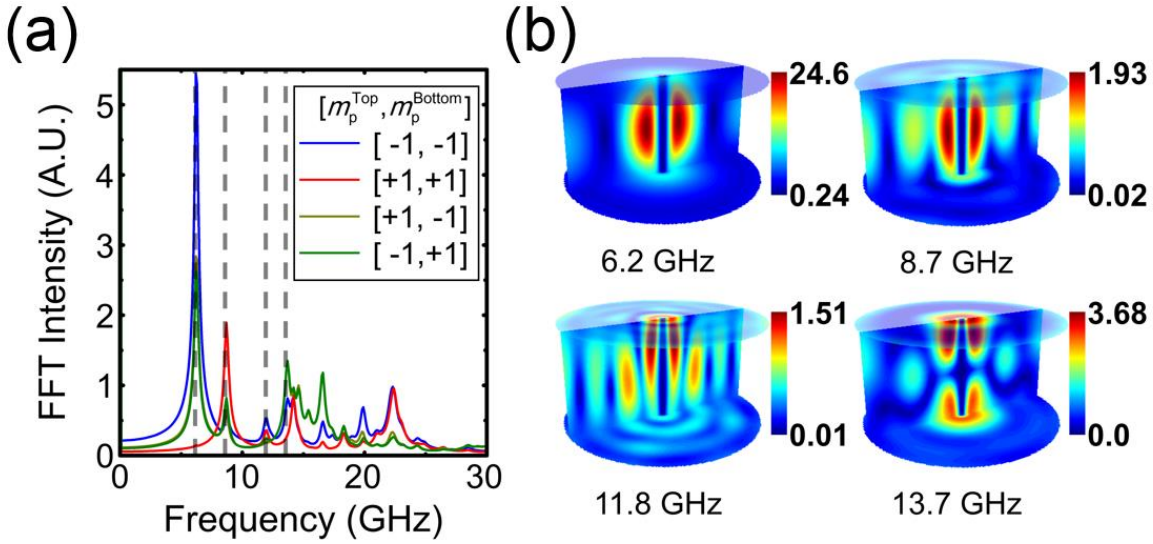

Figure 3.20 The results obtained from FFT of the temporal oscillations of m_z over the entire disk. (a) The averaged value of FFT intensity versus the frequency. The gray dotted lines mean the peaks at 6.2 GHz, 8.7 GHz, 11.8 GHz, and 13.7 GHz. (b) The spatial distribution of FFT intensity corresponding the dotted line in (a) and it is drawn in the system where the magnetization of both polarizer is downward direction.

One distinct peaks were found at 6.2 GHz except the system where the magnetization of both polarizer is upward direction (the system [m_p^{Top}, m_p^{Bottom}] = [+1, +1]). The system [-1, -1] show the largest intensity and then, the system [+1, -1] and the system [-1, +1] follow. We concentrated on the four peaks at the 6.2 GHz, 8.7 GHz, 11.8 GHz and 13.7 GHz in Fig. 3.2(a). At the each peaks, the FFT intensity is localized near the vortex core with satisfying the radial symmetry. Conventionally, it is believed that the radial mode is homogeneous along thickness and its node exists on the in-plane. However, we found that its spatial distribution of FFT is not homogeneous along thickness. Interestingly, as seen in Fig. 3.2(b), there exists a node on not only in-plane but also in the interior region of nanodisk. That is, similar to the higher order gyrotropic mode, new mode exists. Accordingly, it is necessary to specify this dynamic modes.

3.4.2. Excitation of beating mode using AC spin-polarized current

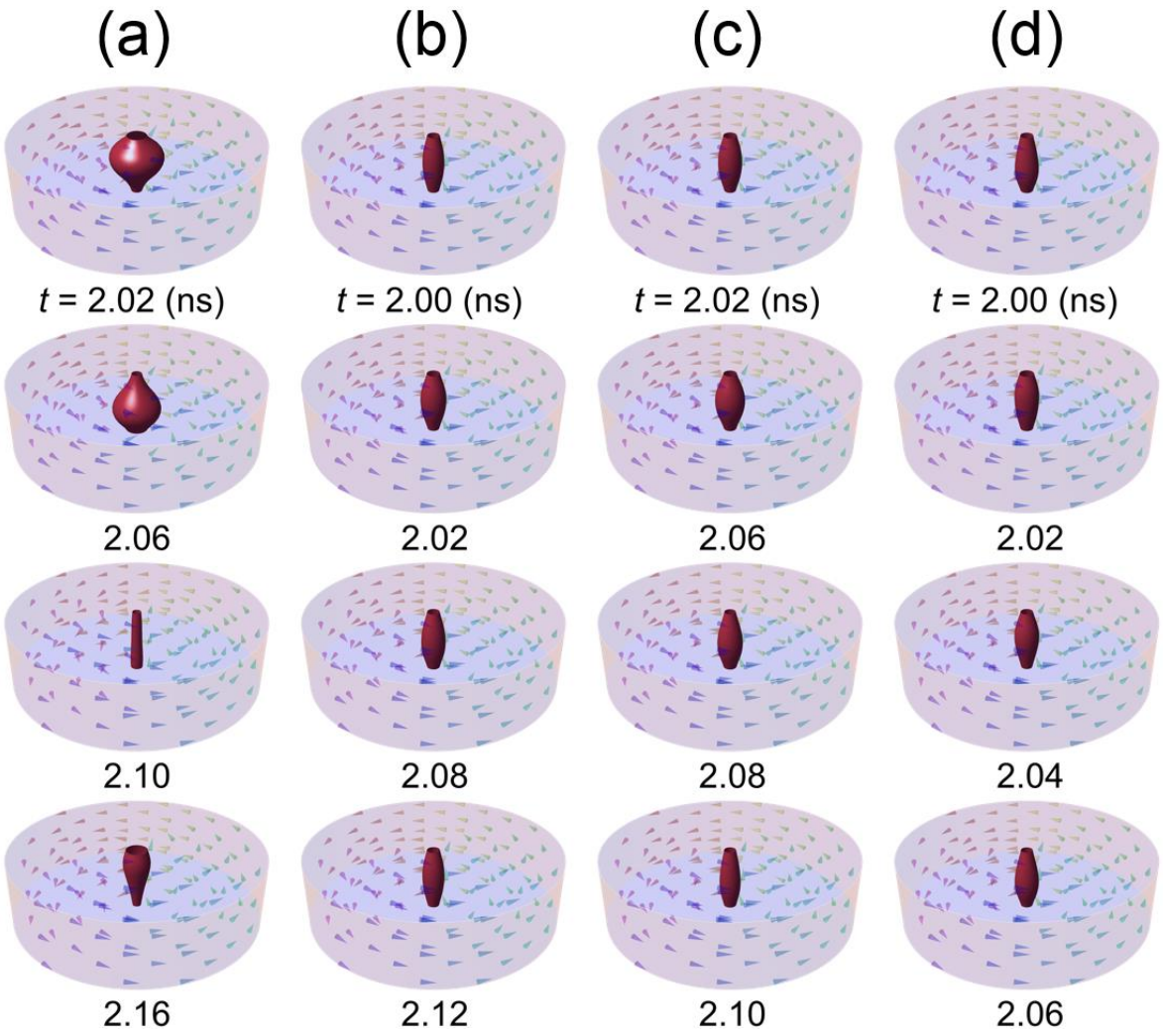

Figure 3.21 the snapshot of the vortex dynamics when it is excited by out-of-plane spin-polarized current with the driving frequency $\omega_D/2\pi$ = 6.2, 8.7, 11.8, and 13.7 GHz.

Then, we applied the out-of-plane sinusoidal current to the magnetic vortex with u_0 = 10 m/s. Fig. 3.21(a-d) describes the vortex dynamics with the driving frequency $\omega_D/2\pi$ = 6.2, 8.7, 11.8, and 13.7 GHz. As seen in Fig. 3.20(a), the strong oscillation is found at $\omega_D/2\pi$ = 6.2 GHz, which shows the size oscillation of vortex core in the interior region with maintaining an in-plane radial symmetry. The oscillation of vortex core on each layer has a different phase. This dynamics of vortex core looks like the heart beat. In this thesis, we call it the beating mode of magnetic vortex and 6.2 GHz is the eigenfrequency for beating mode. When $\omega_D/2\pi$ = 8.7, and 11.8, the core oscillation appears. Interestingly, there are no core oscillation at the center of vortex core in the interior region when When $\omega_D/2\pi$ = 13.7, that is, there is a node at the interior region and it is named a higher order beating mode.

3.4.3. The role of spin transfer torque and Oersted field

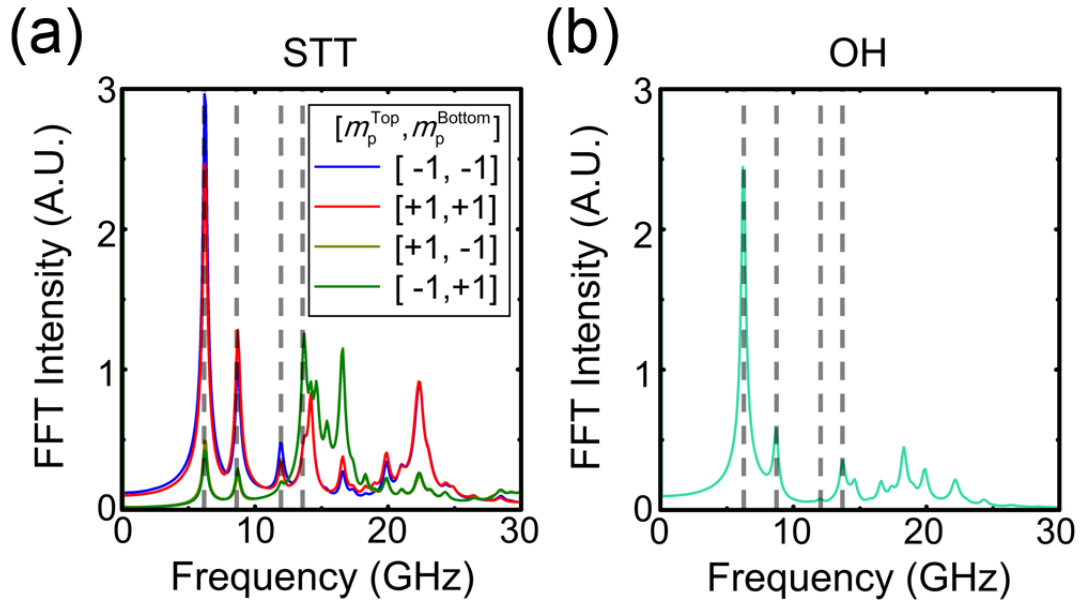

Figure 3.22 FFT results of the temporal oscillations of m_z over the entire disk (a) when considering only ths oscillation of STT and (b) when considering only the oscillation of OH fields. The averaged value of FFT intensity versus the frequency is plotted. The gray dotted lines mean the peaks at 6.2 GHz, 8.7 GHz, 11.8 GHz, and 13.7 GHz.

We applied sinc function out-of-plane spin-polarized current when consdering only the oscillation of STT and when considering only the oscillation of OH fields to specify which a driving force induces the beating mode of magnetic vortex as seen in Fig. 3.22. FFT result induced by each driving force shows the peaks which appears at the previous mentioned frequency although the peak intensity is different each other. Also, in the system [+1, +1], the peak at 6.2 GHz has a sizeable intensity in contrast to negligible intensity at 6.2 GHz when considering both STT and OH, That is, the oscillation amplitude corresponding beating mode and higher order of beating mode is determined by the competition between STT and OH fields.

Furthermore, whether the magnetization of polaizer positioned below Py disk is the parallel or the antiparallel to the that of polarizer positioned above Py disk determines the peak intensity. Parallel case shows a high intensity compared to an antiparallel case. From Table 3.1, the magnetization of polarizer determines whether vortex core is expanded or shrinked by static STT. That is, the polarizer where the magnetization direction is downward (upward) which is positioned below Py disk makes an upward vortex core with c = +1 expanded (shrinked) by static STT. Also, this relation is reversed when the polarizer position is changed or the magnetizaiton of polarizer is changed. Accordingly, two polarizers which has a opposite magnetization makes more flexible oscillation of vortex core.

3.4.4. Constructive and destructive interference in a beating mode

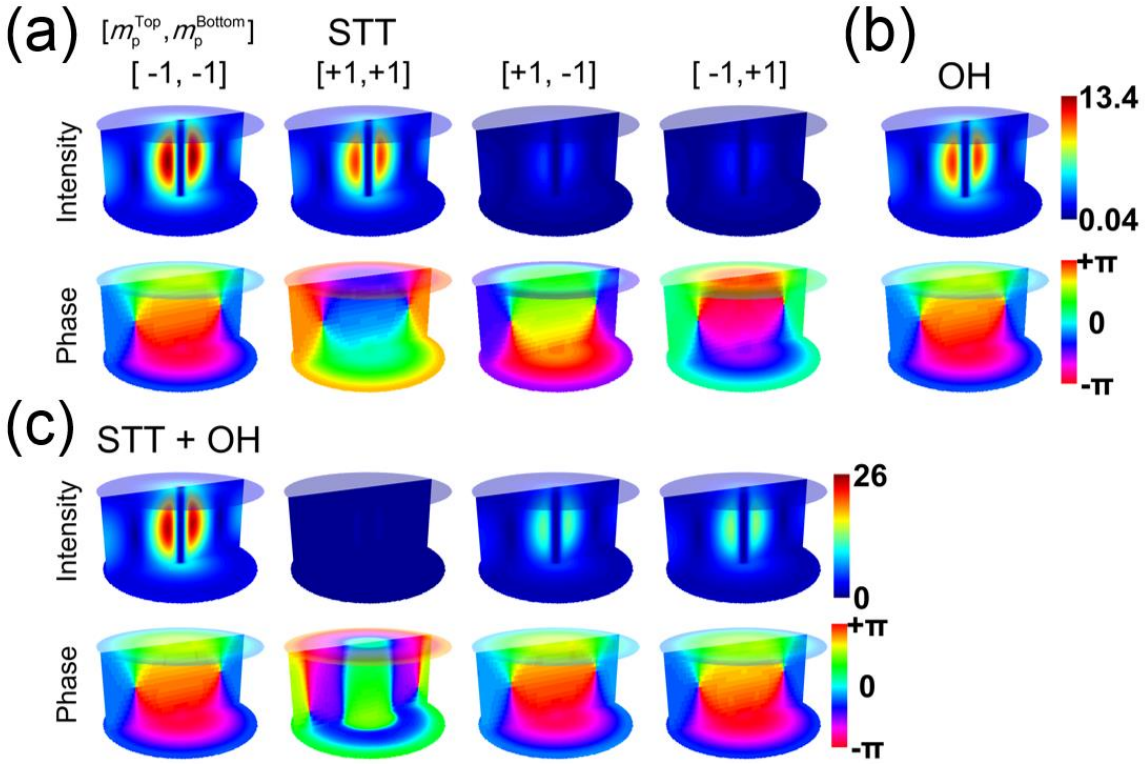

Figure 3.23 Spatial distributions of FFT intensity and phase induced by (a) only STT and (b) only OH fields and (c) both STT and OH fields. The right side of each row means the color bar.

To specify why the system [-1, -1] shows the highest intensity at 6.2 GHz peak when considering both STT and OH fields, we drew the spatial distribution of FFT results as seen in Fig. 3.23. The systems [-1, -1] and [+1, +1] shows completely different FFT intensity from the systems [-1, +1] and [+1, -1] when considering only STT (See Fig. 3.23(a)). There is just phase difference between system [+1, +1] and system [-1, -1] (system [-1, +1] and system [+1, -1]). Those two oscillations are out of phase. The oscillation in the system [-1, -1] and the oscillation driven by only OH fields are in-phase. That is, the system [+1, +1] and the oscillation driven by OH fields have an out-of-phase relation. Accordingly, the spin-polarized current makes peak intensity at 6.2 GHz in the system [-1, -1] increased (decreased) by constructive (destructive) interference. It is originated from the superposition of the oscillations driven by STT and OH. In case of systems [-1, +1] and [+1, -1], there is a small phase difference from the oscillation driven by OH fields. It causes increase of the peak intensity in both systems although the relation is not in phase. Also, except system [-1, -1], the phase of 6.2 GHz, is nearly same as the phase driven by only OH fields.

3.4.5. Vortex core reversal by resonant excitation with beating mode

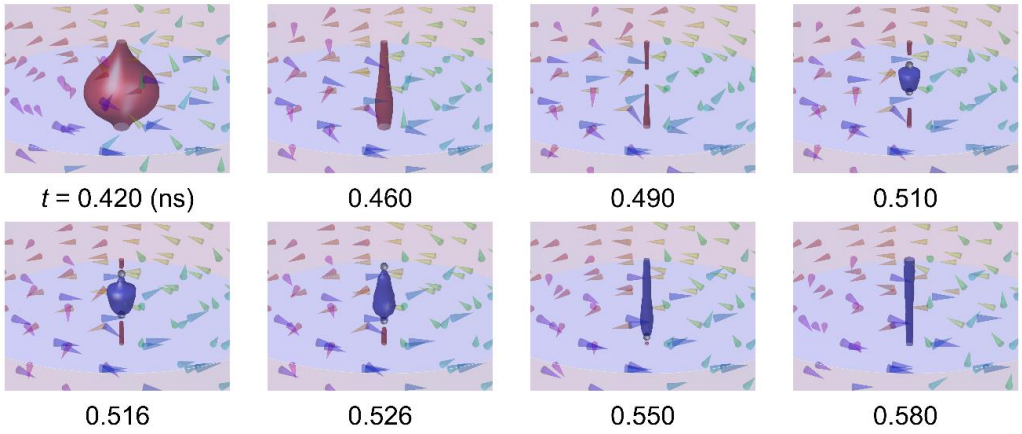

Figure 3.24 The beating mode-assisted vortex core reversals. In the interior region, Bloch point pair (grey sphere) is nucleated with disconnecting of vortex core by formation of negative m_z when u_0 = 25 m/s. In this case, red (blue) surface means the boundaries for $m_z \geq 0.9$.

It is well known that the vortex core reversals through resonant excitation with an intrinsic mode of magnetic vortex. Accordingly, we applied the sinusoidal current along out-of-plane direction. As a results, the vortex core reversal can be achieved in the aids of the resonant excitation with beating mode. Initially, vortex core shows the size oscillation. Then, the size of vortex core is shrinked by strong oscillation, the center of vortex core is disconnected and then, negative m_z is nucleated at the disconnected point with Bloch point pair. One is positioned above and the other is positioned below negative m_z. Each Bloch point moves toward surface with expansion of negative m_z. As a result, the vortex core reversal can be achieved with the annihilation of Bloch point pair.

Previously, the vortex core reversal process, which is topologically trivial, is always mediated by vortex-antivortex pair, or edge soliton. Bloch point is a three-dimensional singularity, which has a skyrmion number q = +1 (-1) if Bloch point has a positive (negative) divergence of magnetization in case of vortex-like Bloch point. Also, the q of magnetic vortex is +1/2 (-1/2) when the magnetization of vortex core is facing the inside (outside) of magnetic element. When the Bloch point pair is nucleated at the center of vortex core, one has q = +1 and the other has q = -1. That is, total skyrmion number of the Bloch point is zero. Also, when the vortex core is combined from Bloch point at the top (bottom) surface, the q is changed from -1/2 (+1/2) to +1/2 (-1/2). That is, this beating mode assisted vortex core reversal is topologically trivial process by conserving the total skyrmion number.

Interestingly, it can be achieved with low power through a resonant excitation with 11.8 GHz frequency. We conformed that the current with u_0 = 15m /s can makes the vortex core reversals although the FFT intensity is small compared to the peak at 6.2 GHz while the beating mode assisted vortex core reversals can be achieved at $u_0 \geq 24$ m/s. Present, we thinks the localized FFT at the top surface makes a strong deformation of vortex core.

3.4.6. A beating mode induced by the oscillating out-of-plane magnetic fields

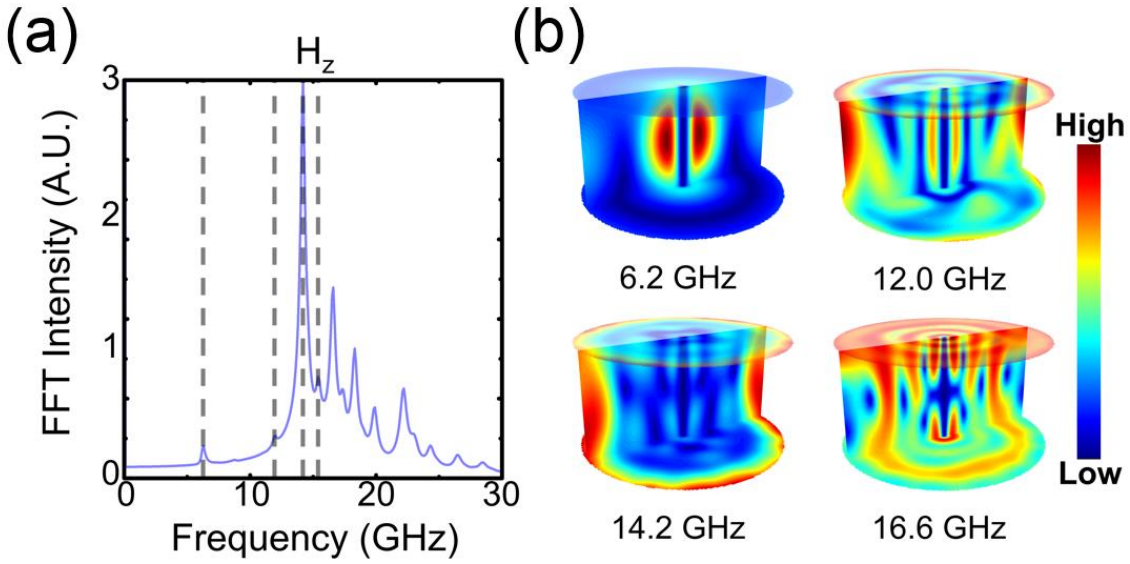

Figure 3.25 The results obtained from FFT of the temporal oscillations of m_z over the entire disk in aids of out-of-plane sinc function fields. (a) The averaged value of FFT intensity versus the frequency is plotted. The gray dotted lines mean the peaks at 6.2 GHz, 12 GHz, 14.2 GHz, and 16.6 GHz. (b) The spatial distribution of FFT intensity corresponding the dotted line in (a).

We applied a sinc function out-of-plane magnetic fields expressed as $H_z = H_{z0}\sin[\omega_H(t-t_0)]/[\omega_H(t-t_0)]$ with H_{z0} = 100 Oe, $\omega_H = 2\pi \times 50$ GHz, and t_0 = 1 ns. It shows the peak at 6.2 GHz corresponding beating mode. However, the FFT intensity is relatively small. Also, there are additional mode at 13.7 GHz which has a node at interior region. Compared to the spin-polarized current driven dynamics, at the edge of disk, the FFT intensity is localized.

To specify the beating mode assisted vortex core reversals using alternating out-of-plane fields, we applied $H = H_{z0}\sin(\omega_D t)$ to the magnetic vortex with p = +1 and c = +1. However, the large amplitdue is required for the vortex core reversals. Even, 1.2kOe alternating magnetic fields cannot switch vortex core. We can achieved the vortex core reversals with 1.5kOe alternating magnetic fields. That is, it is not efficient.

IV. The formation of magnetic vortex

It has been generally believed that one of the four states of magnetic vortex according to *c* and *p* are determined randomly during nucleation process from the saturation states. For developing a non-volatile multi-bit memory device based on the magnetic vortex structure. It is required to find the manipulation method of the magnetic vortex structure. Recently, it is revealed that the magnetic vortex structure is determined stochastically in a patterned asymmetric disk and final spin configuration is dependent on the nucleation process of magnetic vortex structure [78]. To control four states of a magnetic vortex structure, we should understand fundamentals on the nucleation process.

In the classical views, the position, velocities of particles and the force acting on it are known, the dynamics of particles can be calculated in the future or past by a governing equation [79]. In other words, the nature is deterministic. In a nonlinear system in nature, however, there are enormous unpredictable phenomena, such as oscillating of double pendulum and forecasting climate because of *deterministic chaos*. In contrast to the *randomness* system whose time evolution does not occur deterministically but occurs randomly, the time evolution occurs deterministically but it has sensitive dependence on initial conditions. In this works, we firstly reveal that the deterministic chaos occurs in the dynamic nucleation process of magnetic vortex state and, by breaking static- and dynamic-symmetries, the final four states of magnetic vortex can be manipulated very efficiently.

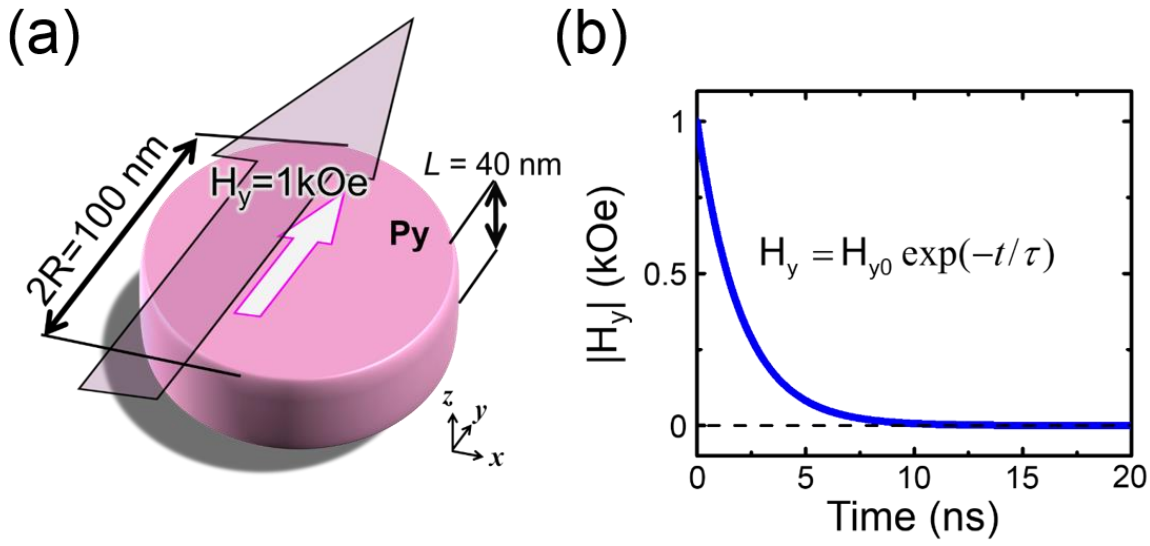

Figure 4.1 (a) The schematic image of a magnetically saturated circular disk along *y*-direction. To mimic experiment, (b) the exponentially decaying fields H_y with time constant τ = 2 ns is employed.

To explore the deterministic chaos in the nucleation process of magnetic vortex, we performed the micromagnetic numerical simulation using OOMMF code [60], which solves numerically the Landau-Lifshitz-Gilbert (LLG) equation: $d\mathbf{M}/dt=-\gamma[\mathbf{M}\times\mathbf{H}_{\mathbf{eff}}]+\alpha/M_s[\mathbf{M}\times(d\mathbf{M}/dt)]$ which describes the time

evolution of the magnetization vector **M,** with the gyromagnetic ratio γ, the effective field $\mathbf{H}_{\mathbf{eff}}$, the Gilbert damping constant α and the saturation magnetization M_s. We used a standard material parameters for permalloy (Py, $Ni_{79}Fe_{21}$) : exchange stiffness A_{ex} = 13 pJ·m^{-1}, M_s = 860 kA·m^{-1}, α = 0.01, γ = 2.21 × 10^5 m·A^{-1}·s^{-1} and zero magnetocrystalline anisotropy with cell size of 1 × 1 × 2 nm^3. As a model system, we adopt a circular Py disk with the radius, R = 50 nm, and the thickness, L = 40 nm (See Fig. 4.1(a)). To observe the nucleation process of magnetic vortex from the uniformly saturated magnetization configuration, a 1 kOe-fields was applied initially and it decayed exponentially with τ = 2 ns as shown in Fig. 4.1(b). To check the sensitive dependence on initial condition in the nucleation process, relaxation simulations were repeated several times with slightly different initial **M** configurations. The energy difference between each initial states is $|\Delta E_{tot}| \leq 5.7 \times 10^{-31}$ J. That is, it looks negligible as shown in Fig. 4.2(a).

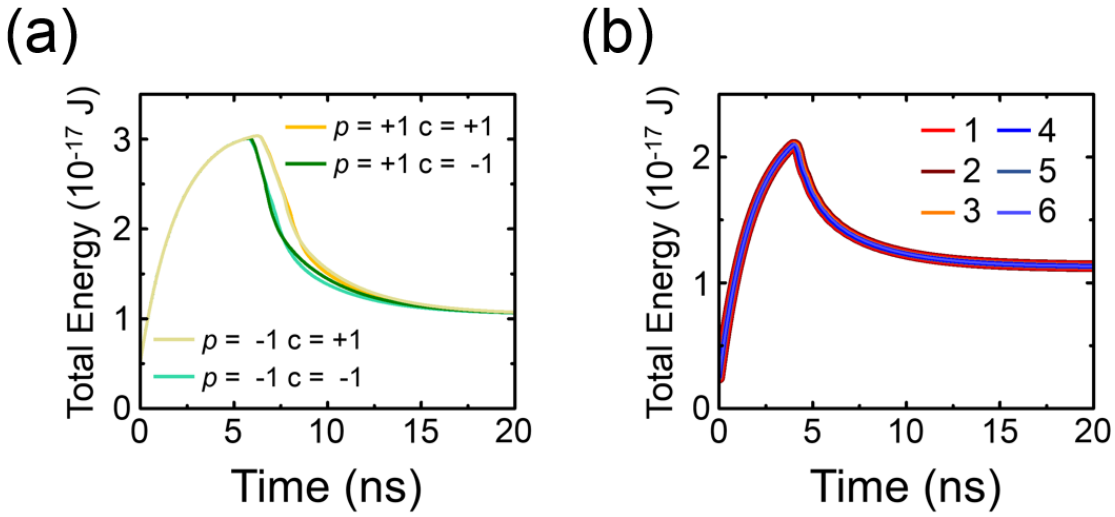

Figure 4.2 The time evolution of the total magnetic energy during the relaxation process in magnetically saturated (a) circular disk and asymmetric disk.

4.1 Chaotic behavior in the formation of magnetic vortex

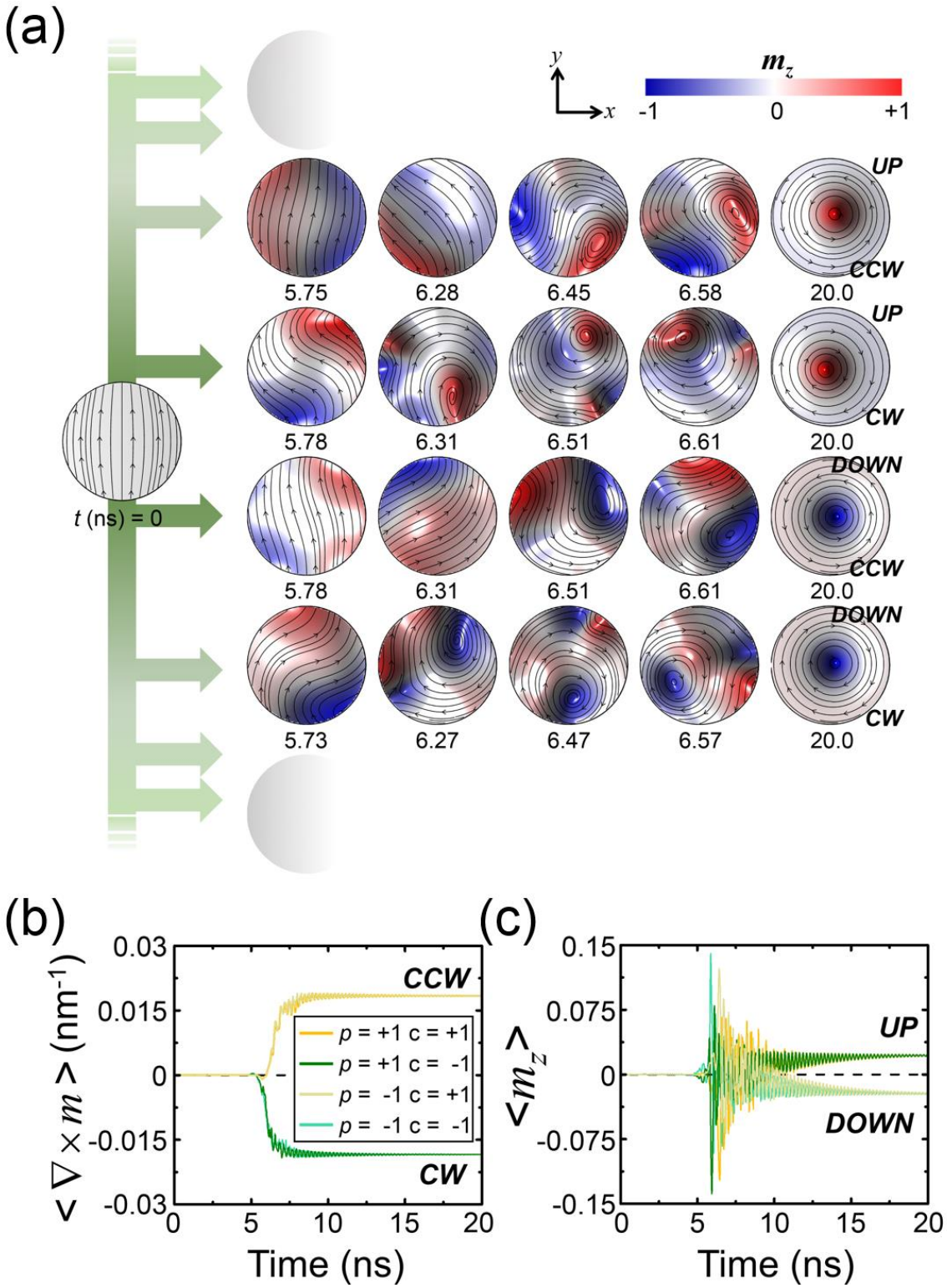

Figure 4.3 The chaos in the nucleation of magnetic vortex structure in a circular disk. (a) A snapshot of four nucleation process of magnetic vortex among a lot of nucleation paths. A color means the average value of m_z along thickness. (b) The time evolution of the curl of normalized M ($\langle \nabla \times m \rangle$), the average value of m_z ($\langle m_z \rangle$). $\langle \nabla \times m \rangle$ means the curling of magnetization configuration and its sign is

corresponded to the chirality of magnetic vortex. Likewise, a sign of $<m_z>$ at the ground state is the polarity of magnetic vortex.

As shown in the time evolution snapshot images in Fig. 4.3(a), the saturated magnetization starts to be curled at the edge and it results in *C*-shaped or *S*-shaped magnetization configuration to reduce a stray fields and curvature of magnetization increases. It makes a dint of curved magnetization at near the edge of the disk and it has a large gradient of magnetization. A non-zero m_z is localized at the magnetization dint configuration and it makes the vortex core structure created from the magnetization dint configuration. Immediately, the complicated magnetization dynamics such as creations and annihilations of the vortex-antivortex pair and edge-solitions follows [80]. Finally, only a single magnetic vortex structure remains with arbitrary *c* and *p*. Representative dynamic nucleation process of four different final magnetic vortex states are shown in Fig. 4.3(a) but there are plenty of different nucleation paths were found according to the initial configuration. Figure 4.3(b) indicates the time evolution of the curl of normalized magnetization ($<\nabla \times m>$) and the average values of m_z ($<m_z>$) which reflect the formation of chirality (*c*) and polarity (*p*), respectively. At the initial magnetization, both $<\nabla \times m>$ and $<m_z>$ are nearly zero until t ~ 5 ns. However, it shows the difference in four nucleation paths of magnetic vortex is marked. Likewise, the time evolution of the total magnetic energy shows a definite difference as shown in Fig. 4.2(a). It reveals that the nucleation process of magnetic vortex shows a sensitive dependence on initial **M** configuration, which is a typical behavior of deterministic chaos. Consequently, any of quaternary states can be formed chaotically.

4.2 Manipulation of chirality of magnetic vortex through a static symmetry breaking

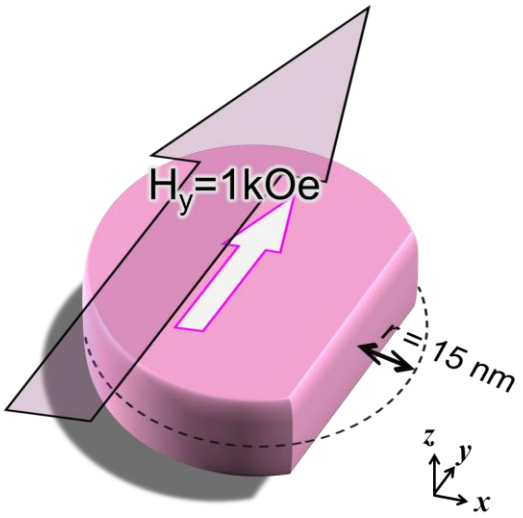

Figure 4.4 The schematic image of a magnetically saturated asymmetric disk along *y*-direction. The decaying fields is described as shown in Fig. 4.1(b).

As reported earlier [81-85], four possible states can be reduced two through a breaking symmetry of the geometry by cutting the edge of circular disk as shown in Fig. 4.4. When the saturation magnetization state is relaxed, the initial magnetization start to curl along the round edge due to magnetostatic energy. The asymmetric geometry with cutting edge gives rise to prevent **M** configuration forming *S*-shaped configuration at the initial stage of the nucleation process (See Fig. 4.5(a)). Only the *C*-shaped **M** configuration is allowed and the dint **M** configuration always forms at the flat edge. Unlike the complex **M** dynamics in a perfect circular disk, the injected magnetic vortex just shows the gyrotropic motion and it is relaxed by an intrinsic damping. This gyrotropic motion causes the oscillation of **M** as seen in Fig. 4.5(b), e. As a result, the magnetic vortex state with the specific curling direction of CW (c = -1) forms finally in an asymmetric disk. Consequently, the chaos of determining c disappears as shown in the plot of $\langle \nabla \times m \rangle$ in Fig. 4.5(b). However, the time evolution of $\langle m_z \rangle$ still shows a chaotic behavior. Interestingly, the sign of $\langle m_z \rangle$ at the instant of occurrence of non-zero $\langle m_z \rangle$ is corresponded to the out-of-plane core direction of final magnetic vortex structure since there is no vortex core reversal during the nucleation process in contrast to the case of perfect circular disk in which the complex dynamics including multiple core reversals. Furthermore, it was found that the sign of $\langle m_x \rangle$ always opposites to that of $\langle m_z \rangle$ during the nucleation process while $\langle m_y \rangle$ decreases rapidly at the instant of symmetry breaking as shown in Fig. 4.5(c-e). Those reveal that negative (positive) value of $\langle m_x \rangle$ always occurs when the magnetic vortex structure is formed with p = +1 (-1). From a repetitive simulation with a slightly different **M** configuration in an asymmetric disk ($|\Delta E_{tot}| \leq 1.4 \times 10^{-30}$ J, see Fig. 4.2(b)), such tendency of nucleation process is not changed and there are only two nucleation paths which are energetically equivalent each other. It should be mentioned that the curling direction switched

if the initial saturation direction reversed. And thus, *c* is controlled by the saturation direction but *p* is still determined chaotically.

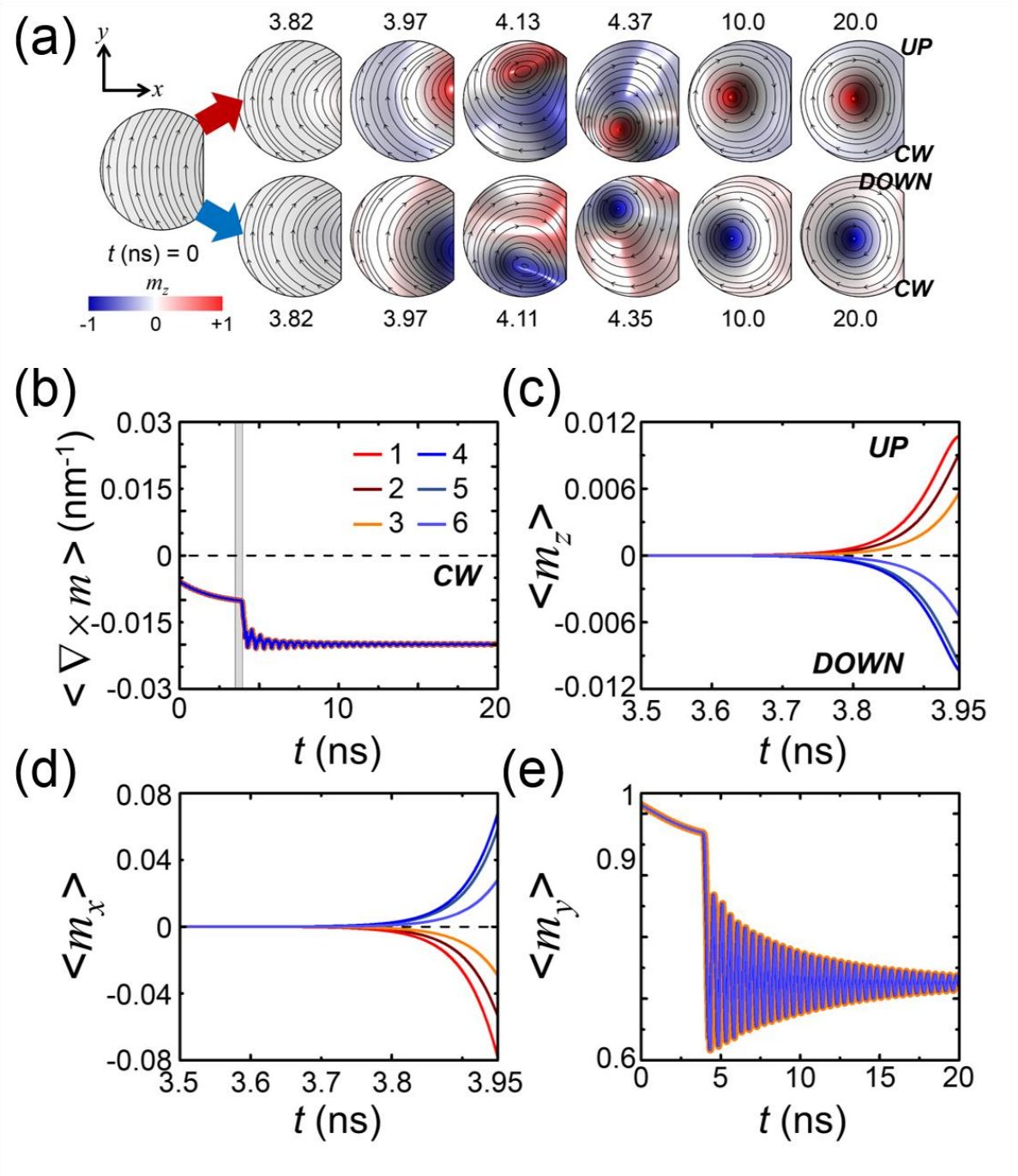

Figure 4.5 The chaos in the nucleation of magnetic vortex in an asymmetric disk. (a) The snapshot of two nucleation paths of magnetic vortex. The time evolution of curl is always negative. (c) and (d) show a time evolution of $<m_z>$ and $<m_x>$ in a time where marked in Fig. 4.51(a). (e) A time evolution of $<m_y>$ shows the rapid decrease of $<m_y>$ induced by nucleation of magnetic vortex and gyrotropic motion of magnetic vortex.

4.3 An implicit relation on magnetization dynamics

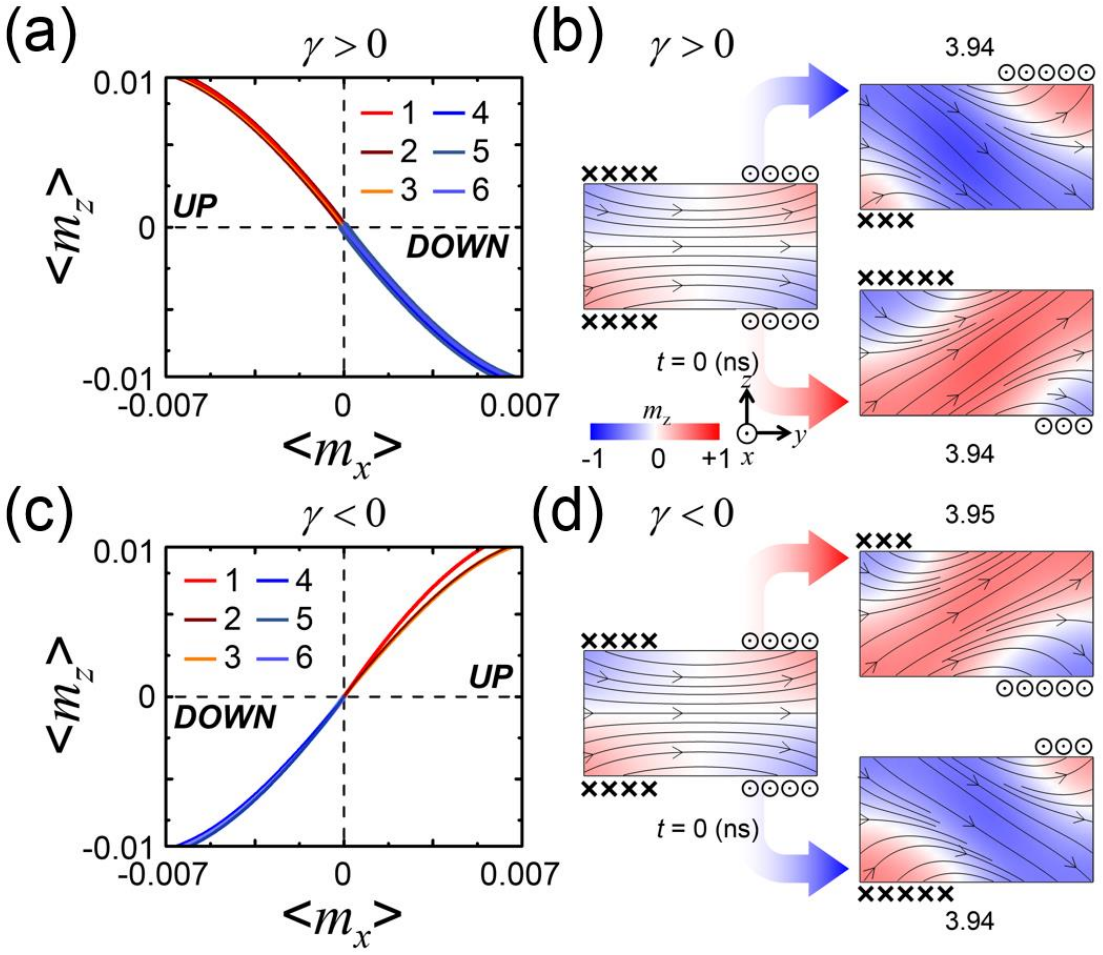

Figure 4.6 The implicit relation between $\langle m_z \rangle$ and $\langle m_x \rangle$ originated from LLG equation. A trajectories of $\langle m_z \rangle$ vs $\langle m_x \rangle$ when gyromagnetic ratio (a) $\gamma > 0$ and (c) $\gamma < 0$ in the asymmetric disk before a magnetic vortex is nucleated at the flat edge. The snapshot of magnetization at the flat edge when symmetry breaking occurs with (e) $\gamma > 0$ and (d) $\gamma < 0$.

In the asymmetric disk which excludes the chaos on *c* state formation process, the trajectories of ($\langle m_x \rangle$,$\langle m_z \rangle$) appear only at the second and the fourth quadrant in Fig. 4.6(a). It results in an implicit relation between $\langle m_x \rangle$ and $\langle m_z \rangle$. To understand the relation between $\langle m_x \rangle$ and $\langle m_z \rangle$ in the nucleation process, we focus on the detailed nucleation process of vortex core from the dint magnetization configuration in the vicinity of the flat edge. Figure 4.6(b) indicates the magnetization distribution at the flat edge of the asymmetric disk. At the initial saturation state, magnetization configuration on the flat edge has the mirror symmetry with respect to the *y*-axis. But the symmetry breaks after 3.8 ns in Fig. 4.5; the oblique magnetization configuration forms along +*y* and +*z* direction (/-shape) or along +*y* and –*z* direction (\-shape). Since the oblique **M** configuration is shifted from the center, the *x* component of magnetization on the upper and lower surface is imbalanced as shown in Fig. 4.3(b). The +*z* (–*z*)

oblique **M** configuration is shifted always along the $+y$ ($-y$) direction and thus, $-x$ ($+x$) component **M** on the upper (lower) surface exceeds $+x$ ($-x$) component **M** on the lower (upper) surface. It is found that the core with $p = +1$ (-1) is injected into the disk center from the $+z$ ($-z$) oblique **M** configuration on the flat edge surface as shown in Fig. 4.7(a).

Consequently, the sign of $<m_x>$ and $<m_z>$ are always opposite during the nucleation process. It is reported that the asymmetry in time evolution be important for nucleation dynamics of magnetic vortex [86]. We found such asymmetric behavior of shifted direction according to the oblique **M** configuration direction comes from the intrinsic symmetry breaking of the magnetization dynamics. Since **M** presses about the effective field with a specific direction as described in LLG equation, the dynamic motion of **M** has inherent dynamic-symmetry breaking. To confirm this, we put the negative sign of gyromagnetic ratio γ in LLG equation. As shown in Fig. 4.6(c) the relation between the oblique **M** configuration direction and the shift direction are opposite to the case of positive γ value in Fig. 4.6(b). The reversal of the implicit relation between $<m_z>$ and $<m_x>$ with the sign of γ as shown in Fig. 4.6(d) and 4.7(b) reveals clearly that it results from the intrinsic asymmetry of **M** dynamics.

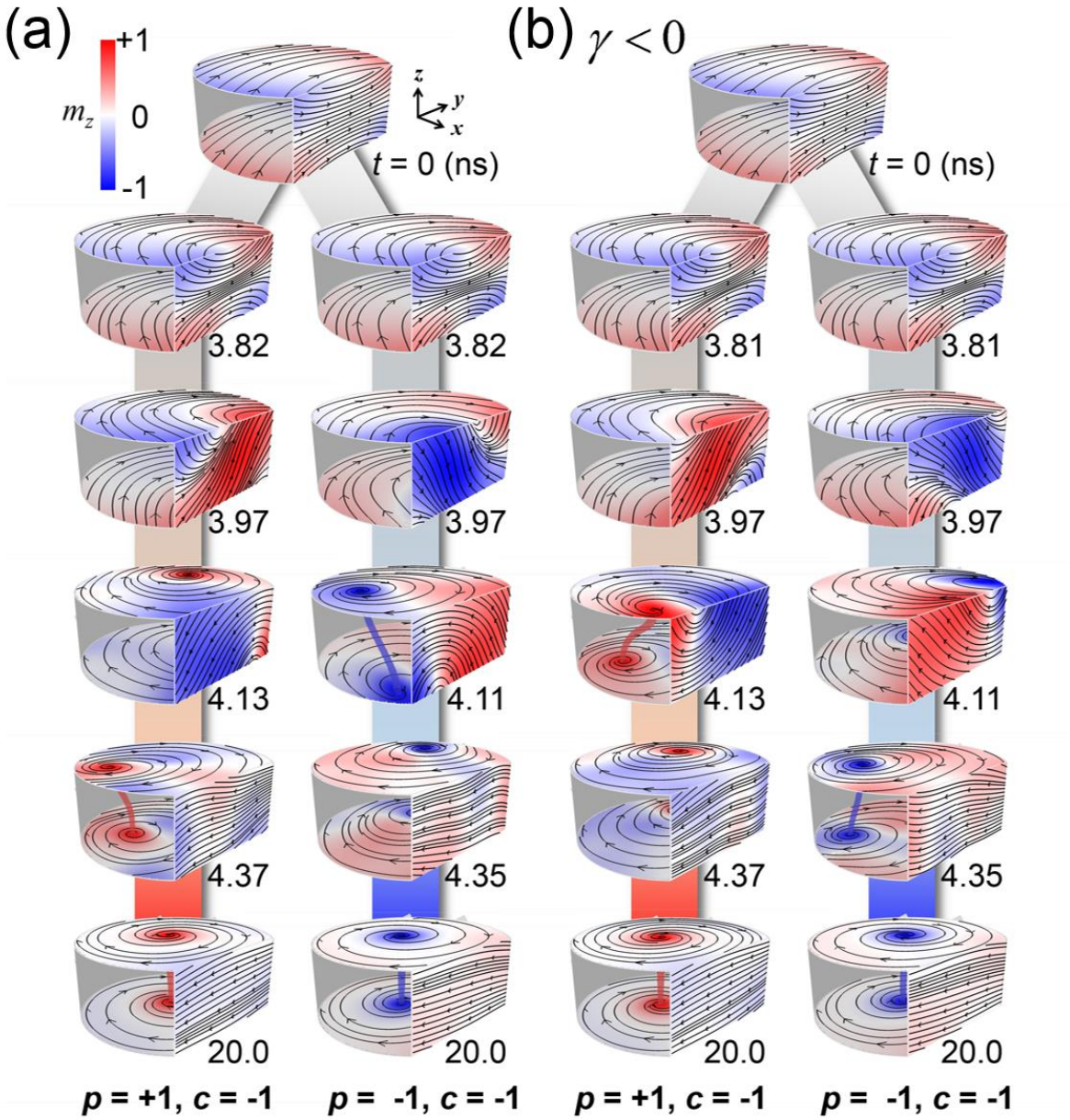

Figure 4.7 The time evolution of **M** distribution at the surface of the asymmetric disk when (a) $\gamma > 0$ and (b) $\gamma < 0$.

4.4 Manipulation of polarity of magnetic vortex through a dynamic symmetry breaking

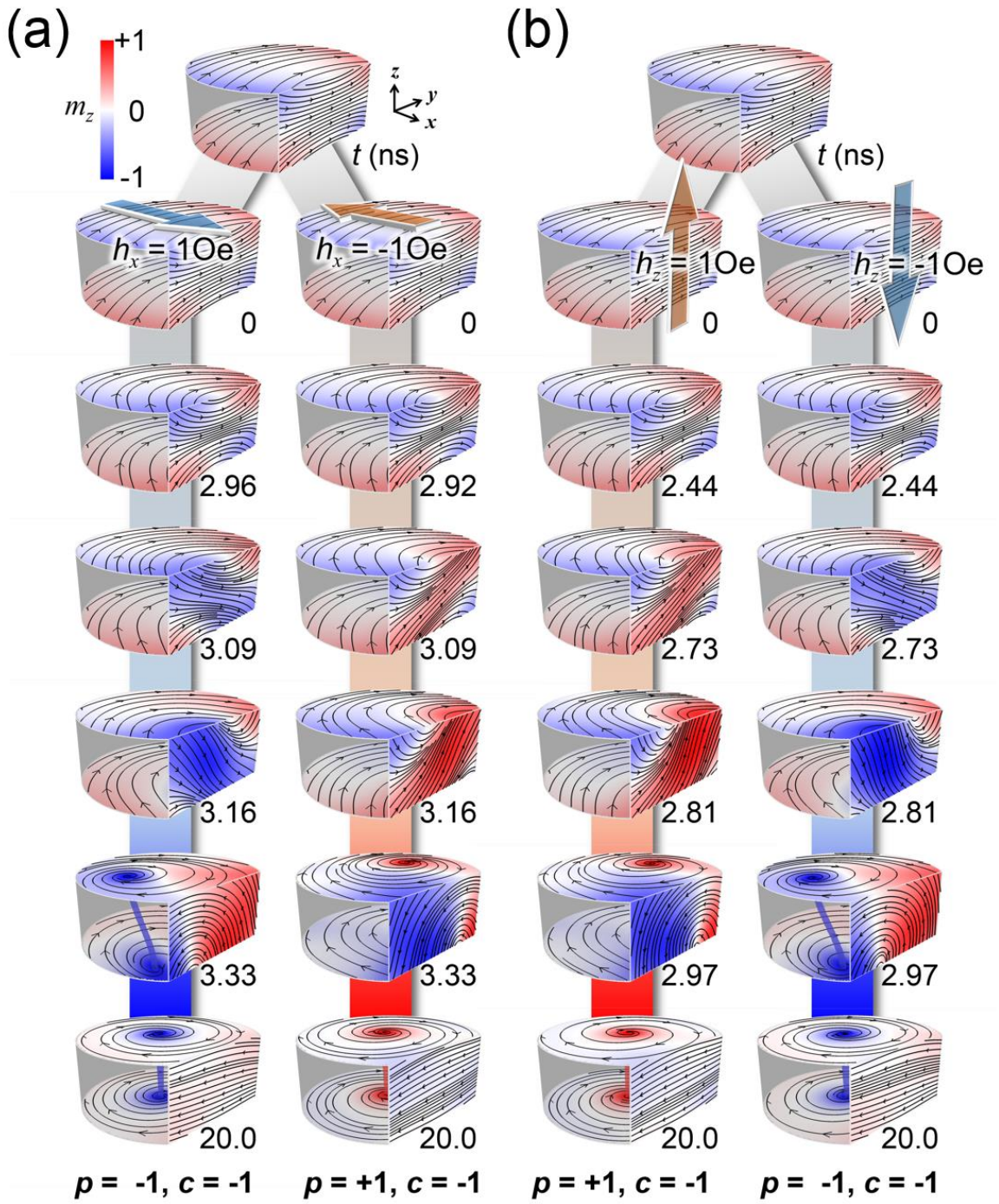

Figure 4.8 The manipulation of magnetic vortex using an external fields along (a) *x*-direction and (b) *z*-direction.

Based on such implicit relation, we applied the weak external fields (~1 Oe) along *x*-direction and *z*-direction to affect the sign of $\langle m_x \rangle$ and $\langle m_z \rangle$. First of all, considering the external fields h_x along x-

direction, the external fields along +x (-x) direction favors <m_x> with positive (negative) sign and it gives rise to the negative (positive) sign of <m_z> during the nucleation process (See Fig. 4.7). As a result, the magnetic vortex structure with p = +1 (-1) appears at the final state. Likewise, the direction of external fields h_z along z-direction determines a core polarization. Interestingly, the nucleation dynamics of magnetic vortex is the same as the chaotic dynamics in the asymmetric disk without the external fields except the reduction of nucleation time. That is, the sign of <m_x> always follows the sign of the external fields along x- (z-) direction and the sign of <m_x> follows the resulted implicit relation between <m_x> and <m_z> when there is no any external fields as shown in Fig. 4.8.

If the sign of γ is changed, the nucleation dynamics follows reversed implicit relation. That is, the chaotic behavior on nucleating magnetic vortex dynamics completely disappear even though the strength of external fields looks negligible as a "butterfly effect" which originate from an example for the fluttering of wings of butterfly to make a hurricane [79]. It seems that the role of external fields looks negligible due to a weak fields strength but it breaks the dynamic symmetry of nucleation process. It reveals that the breaking of the dynamic symmetry of the magnetization using an external fields manipulate the final vortex state.

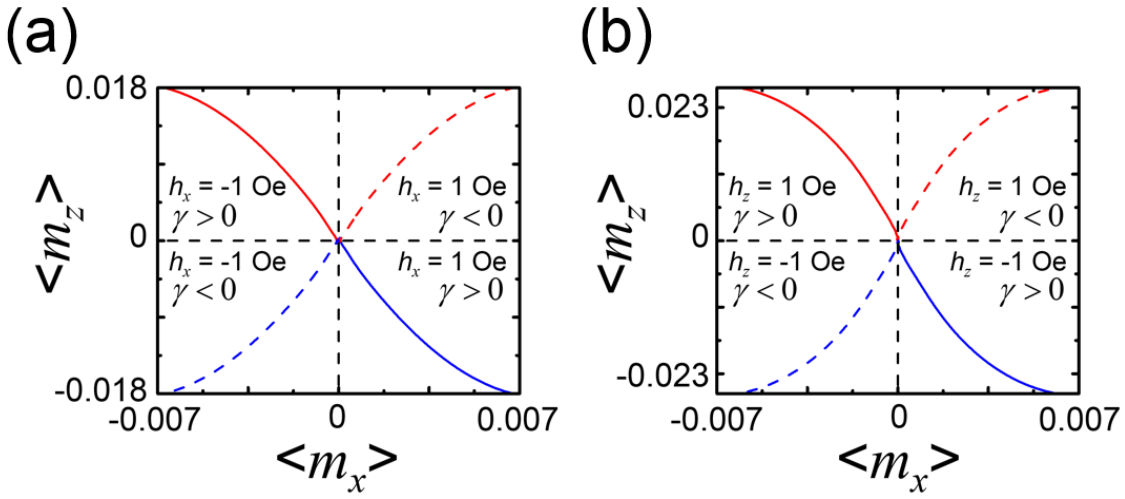

Figure 4.9 A trajectories of <m_z> vs <m_x>in the asymmetric disk before a magnetic vortex is nucleated at the flat edge when external fields is applied along (a) x-direction and (b) z-direction. The solid line means $\gamma > 0$ and dotted line means (c) $\gamma < 0$. Red (Blue) color means that the final spin state is magnetic vortex with p = +1 (-1).

4.4 Fully controlling of a magnetic vortex by a tilted magnetically saturation direction

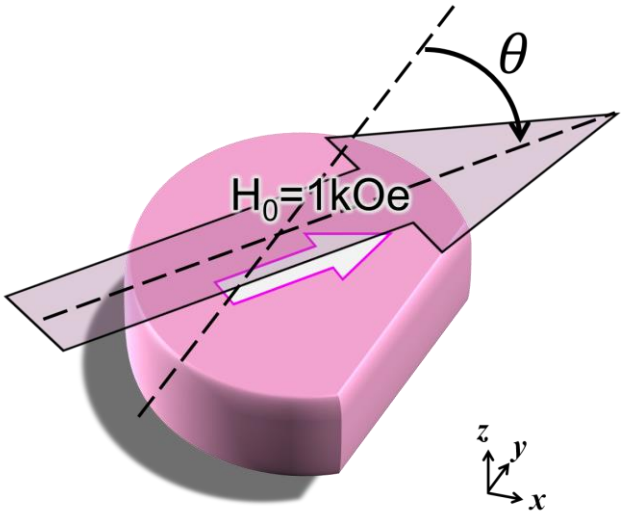

Figure 4.10 The schematic image of a magnetically saturated asymmetric disk. The saturation direction is tilted with respect to the *y*-direction. The decaying fields is described as shown in Fig. 4.1(b).

Finally, we combines in-plane external fields and exponentially decaying fields by tilting in-plane saturation direction as shown in Fig. 1(c). The angle between *y*-axis and the saturation direction θ determines the final magnetic vortex state. That is, $H_0 \sin\theta$ is a role of the in-plane fields along x direction while $H_0 \cos\theta$ is an analogous to the exponentially decaying fields of a previous system. The resultant simulation data is shown in Table 4.1. In the regime $50° < |\theta| < 130°$, it shows the chaotic dynamics due to decreasing the effect of a static symmetry breaking. In other words, $H_0 \cos\theta$ is larger than $H_0 \sin\theta$ cannot reduce a complex dynamics to two nucleation path. In case of $|\theta| < 50°$ ($|\theta| > 130°$), *c* is always -1 (+1) and the sign of θ determines *p*. Accordingly, this tilted saturation state can makes the magnetic vortex state efficiently.

Table 4.1 The magnetic vortex state with varying the angle θ.

$\theta < 0$	*p*	*c*	$\theta > 0$	*p*	*c*
-5°	+1	-1	5°	-1	-1
-10°	+1	-1	10°	-1	-1
-15°	+1	-1	15°	-1	-1
-20°	+1	-1	20°	-1	-1
-25°	+1	-1	25°	-1	-1
-30°	+1	-1	30°	-1	-1
-35°	+1	-1	35°	-1	-1
-40°	+1	-1	40°	-1	-1
-45°	+1	-1	45°	-1	-1
-50°	*Chaos*	*Chaos*	50°	*Chaos*	*Chaos*

-60°	*Chaos*	*Chaos*	60°	*Chaos*	*Chaos*
-70°	*Chaos*	*Chaos*	70°	*Chaos*	*Chaos*
-80°	*Chaos*	*Chaos*	80°	*Chaos*	*Chaos*

5. Summary

An energetically equivalent fourfold states of magnetic vortex structure in ferromagnetic nanoelement has high thermal stability and an intriguing dynamic properties. It receives a great attention for developing an information storage device and nano-oscillator. It is considered that its magnetization distribution is uniform along thickness. Based on such assumption, most of simulation and analytical approaches related to the magnetic vortex is performed. However, when the thickness of nanelement is relatively thick (> ~ 70 nm). The magnetization distribution of magnetic vortex is no longer homogeneous. It causes a novel dynamics of magnetic vortex such as higher-order dynamics reported in [18-22] which cannot be observed in thin nanoelement. This thesis deals with magnetic vortex dynamics under an in-plane rotating magnetic fields and an out-of-plane spin-polarized current by micromagnetic numerical simulations in relatively thick circular disk. Also, it treats a chaotic formation of magnetic vortex and its control.

In relatively thick circular disk, the magnetic vortex shows a reported gyrotropic motion under a rotating magnetic field of eigenfrequency with low amplitude. However, as increasing amplitude, this linear gyrotropic motion disappears and the complex nonlinear gyrotropic motion appears instead of vortex core reversals. It shows dramatic time-varying gyro-radii and velocity and it causes the tearing up vortex core at the surface. A torn vortex core called vortex tube structure consist of antivortex-vortex pair. It is annihilated by combination of antivortex-vortex pair with opposite polarization and vortex pair. This complex dynamics is a topologically trivial process and it is revealed by conservation of topological numbers, such as winding number n and skyrmion number q.

Such nonlinear dynamics appears when DC spin-polarized current is applied to the magnetic vortex structure along out-of-plane direction. Whether chirality is counterclockwise (CCW) or clockwise (CW) and whether a circumferential Oersted (OH) fields is considered or not determines the vortex dynamics. In relatively thick nanoelement, both spin transfer torque (STT) and OH fields can make the size of vortex core. Accordingly, only STT can make the shift of eigenfrequency. In our system, only vortex core reversals can be achieved when chirality is CW. However, DC spin polarized currents make vortex core reversal achieved. It spends a lot of time due to radial symmetry when the vortex core is not initially shifted.

We found that a new mode of magnetic vortex which exists in thick nanoelement. It is corresponded to the size oscillation of vortex core induced by STT and OH fields, which called beating mode and higher order beating mode in this thesis. Through resonant excitation using AC spin-polarized current along out-of-plane direction, we can achieve ultrafast vortex core reversal. This beating mode can be excited by out-of-plane sinusoidal magnetic fields but its intensity is small compared to the excitation by spin-polarized currents. Finally, this thesis shows the chaotic behavior and inherent symmetry

breaking in the nucleation of magnetic vortex and we show that it can be manipulated simply by the breaking of the static- and dynamic-symmetries.

REFERENCES

1 Slonczewski, J. C. Current-driven excitation of magnetic multilayers. *Journal of Magnetism and Magnetic Materials* **159**, L1-L7, doi:http://dx.doi.org/10.1016/0304-8853(96)00062-5 (1996).

2 Berger, L. Emission of spin waves by a magnetic multilayer traversed by a current. *Physical Review B* **54**, 9353-9358 (1996).

3 Brataas, A., Kent, A. D. & Ohno, H. Current-induced torques in magnetic materials. *Nature materials* **11**, 372-381, doi:10.1038/nmat3311 (2012).

4 Liu, Y., Li, H., Hu, Y. & Du, A. Oscillation frequency of magnetic vortex induced by spin-polarized current in a confined nanocontact structure. *Journal of Applied Physics* **112**, 093905, doi:10.1063/1.4764059 (2012).

5 Parkin, S. S. P., Hayashi, M. & Thomas, L. Magnetic Domain-Wall Racetrack Memory. *Science* **320**, 190-194, doi:10.1126/science.1145799 (2008).

6 Parkin, S. & Yang, S. H. Memory on the racetrack. *Nature nanotechnology* **10**, 195-198, doi:10.1038/nnano.2015.41 (2015).

7 Cowburn, R. P. Spintronics: Change of direction. *Nature materials* **6**, 255-256 (2007).

8 Yu, Y.-S., Jung, H., Lee, K.-S., Fischer, P. & Kim, S.-K. Memory-bit selection and recording by rotating fields in vortex-core cross-point architecture. *Applied Physics Letters* **98**, 052507, doi:10.1063/1.3551524 (2011).

9 Yu, Y.-S. *et al.* Polarization-selective vortex-core switching by tailored orthogonal Gaussian-pulse currents. *Physical Review B* **83**, doi:10.1103/PhysRevB.83.174429 (2011).

10 Dussaux, A. *et al.* Field dependence of spin-transfer-induced vortex dynamics in the nonlinear regime. *Physical Review B* **86**, doi:10.1103/PhysRevB.86.014402 (2012).

11 Dussaux, A. *et al.* Large microwave generation from current-driven magnetic vortex oscillators in magnetic tunnel junctions. *Nature communications* **1**, 8, doi:10.1038/ncomms1006 (2010).

12 Choi, Y.-S., Kim, S.-K., Lee, K.-S. & Yu, Y.-S. Understanding eigenfrequency shifts observed in vortex gyrotropic motions in a magnetic nanodot driven by spin-polarized out-of-plane dc current. *Applied Physics Letters* **93**, 182508, doi:10.1063/1.3012380 (2008).

13 Kim, M.-K. *et al.* Self-assembled magnetic nanospheres with three-dimensional magnetic vortex. *Applied Physics Letters* **105**, 232402, doi:10.1063/1.4903741 (2014).

14 Kim, S. K. *et al.* Resonantly excited precession motion of three-dimensional vortex core in magnetic nanospheres [corrected]. *Scientific reports* **5**, 11370, doi:10.1038/srep11370 (2015).

15 Yoo, M.-W. & Kim, S.-K. Curved geometrical confinement effect on vortex-state reversals in magnetic half-spheres. *Applied Physics Express* **8**, 063003, doi:10.7567/apex.8.063003 (2015).

16 Yoo, M.-W., Lee, J.-H. & Kim, S.-K. Excited eigenmodes in magnetic vortex states of soft magnetic half-spheres and spherical caps. *Journal of Applied Physics* **116**, 223902, doi:10.1063/1.4903815 (2014).

17 Sloika, M. I., Kravchuk, V. P., Sheka, D. D. & Gaididei, Y. Curvature induced chirality symmetry breaking in vortex core switching phenomena. *Applied Physics Letters* **104**, 252403, doi:10.1063/1.4884957 (2014).

18 Ding, J., Kakazei, G. N., Liu, X., Guslienko, K. Y. & Adeyeye, A. O. Higher order vortex gyrotropic modes in circular ferromagnetic nanodots. *Scientific reports* **4**, 4796, doi:10.1038/srep04796 (2014).

19 Ding, J., Kakazei, G. N., Liu, X. M., Guslienko, K. Y. & Adeyeye, A. O. Intensity inversion of vortex gyrotropic modes in thick ferromagnetic nanodots. *Applied Physics Letters* **104**, 192405, doi:10.1063/1.4878617 (2014).

20 Boust, F. & Vukadinovic, N. Micromagnetic simulations of vortex-state excitations in soft magnetic nanostructures. *Physical Review B* **70**, doi:10.1103/PhysRevB.70.172408 (2004).

21 Yan, M., Hertel, R. & Schneider, C. M. Calculations of three-dimensional magnetic normal modes in mesoscopic permalloy prisms with vortex structure. *Physical Review B* **76**, doi:10.1103/PhysRevB.76.094407 (2007).

22 Lv, G., Zhang, H., Cao, X., Gao, F. & Liu, Y. Micromagnetic simulations of magnetic normal modes in elliptical nanomagnets with a vortex state. *Applied Physics Letters* **103**, 252404, doi:10.1063/1.4850537 (2013).

23 Cohen, M. S. Lorentz Microscopy of Small Ferromagnetic Particles. *Journal of Applied Physics* **36**, 1602, doi:10.1063/1.1703094 (1965).

24 Raabe, J. *et al.* Magnetization pattern of ferromagnetic nanodisks. *Journal of Applied Physics* **88**, 4437, doi:10.1063/1.1289216 (2000).

25 Miltat, J. & Thiaville, A. Vortex Cores--Smaller Than Small. *Science* **298**, 555, doi:10.1126/science.1077704 (2002).

26 Shinjo, T., Okuno, T., Hassdorf, R., Shigeto, K. & Ono, T. Magnetic Vortex Core Observation in Circular Dots of Permalloy. *Science* **289**, 930-932, doi:10.1126/science.289.5481.930 (2000).

27 Wachowiak, A. *et al.* Direct Observation of Internal Spin Structure of Magnetic Vortex Cores. *Science* **298**, 577-580, doi:10.1126/science.1075302 (2002).

28 Im, M. Y. *et al.* Symmetry breaking in the formation of magnetic vortex states in a permalloy nanodisk. *Nature communications* **3**, 983, doi:10.1038/ncomms1978 (2012).

29 Guslienko, K. Y. *et al.* Eigenfrequencies of vortex state excitations in magnetic submicron-size

disks. *Journal of Applied Physics* **91**, 8037, doi:10.1063/1.1450816 (2002).

30 Novosad, V. *et al.* Spin excitations of magnetic vortices in ferromagnetic nanodots. *Physical Review B* **66**, doi:10.1103/PhysRevB.66.052407 (2002).

31 Guslienko, K. Y., Scholz, W., Chantrell, R. W. & Novosad, V. Vortex-state oscillations in soft magnetic cylindrical dots. *Physical Review B* **71**, doi:10.1103/PhysRevB.71.144407 (2005).

32 Buess, M. *et al.* Fourier transform imaging of spin vortex eigenmodes. *Physical review letters* **93**, 077207, doi:10.1103/PhysRevLett.93.077207 (2004).

33 Thiele, A. A. Steady-State Motion of Magnetic Domains. *Physical review letters* **30**, 230-233, doi:10.1103/PhysRevLett.30.230 (1973).

34 Fischer, P. *et al.* X-ray imaging of vortex cores in confined magnetic structures. *Physical Review B* **83**, doi:10.1103/PhysRevB.83.212402 (2011).

35 Choe, S.-B. *et al.* Vortex Core-Driven Magnetization Dynamics. *Science* **304**, 420-422, doi:10.1126/science.1095068 (2004).

36 Yu, Y. S. *et al.* Resonant amplification of vortex-core oscillations by coherent magnetic-field pulses. *Scientific reports* **3**, 1301, doi:10.1038/srep01301 (2013).

37 Lee, K.-S., Guslienko, K. Y., Lee, J.-Y. & Kim, S.-K. Ultrafast vortex-core reversal dynamics in ferromagnetic nanodots. *Physical Review B* **76**, doi:10.1103/PhysRevB.76.174410 (2007).

38 Van Waeyenberge, B. *et al.* Magnetic vortex core reversal by excitation with short bursts of an alternating field. *Nature* **444**, 461-464, doi:10.1038/nature05240 (2006).

39 Yamada, K. *et al.* Electrical switching of the vortex core in a magnetic disk. *Nature materials* **6**, 269-263, doi:10.1038/nmat1867 (2007).

40 Kammerer, M. *et al.* Magnetic vortex core reversal by excitation of spin waves. *Nature communications* **2**, 279, doi:10.1038/ncomms1277 (2011).

41 Yoo, M.-W., Lee, J. & Kim, S.-K. Radial-spin-wave-mode-assisted vortex-core magnetization reversals. *Applied Physics Letters* **100**, 172413, doi:10.1063/1.4705690 (2012).

42 Yoo, M.-W. & Kim, S.-K. Azimuthal-spin-wave-mode-driven vortex-core reversals. *Journal of Applied Physics* **117**, 023904, doi:10.1063/1.4905689 (2015).

43 Landau, L. D. & Lifshitz, E. M. Theory of the dispersion of magnetic permeability in ferromagnetic bodies. *Phys. Z. Sowjetunion* **8** (1935).

44 Brown, W. F. *Micromagnetics*. (Interscience Publishers, 1963).

45 Gilbert, T. L. A Lagrangian formulation of the gyromagnetic equeation of the magnetic field. *Physics Review* **100**, 1243 (1955).

46 Martinez, E., Emori, S. & Beach, G. S. D. Current-driven domain wall motion along high perpendicular anisotropy multilayers: The role of the Rashba field, the spin Hall effect, and the Dzyaloshinskii-Moriya interaction. *Applied Physics Letters* **103**, 072406,

doi:10.1063/1.4818723 (2013).

47 Kim, K.-W., Seo, S.-M., Ryu, J., Lee, K.-J. & Lee, H.-W. Magnetization dynamics induced by in-plane currents in ultrathin magnetic nanostructures with Rashba spin-orbit coupling. *Physical Review B* **85**, doi:10.1103/PhysRevB.85.180404 (2012).

48 Zhang, S. & Li, Z. Roles of nonequilibrium conduction electrons on the magnetization dynamics of ferromagnets. *Physical review letters* **93**, 127204, doi:10.1103/PhysRevLett.93.127204 (2004).

49 Thiaville, A., Nakatani, Y., Miltat, J. & Suzuki, Y. Micromagnetic understanding of current-driven domain wall motion in patterned nanowires. *Europhysics Letters (EPL)* **69**, 990-996, doi:10.1209/epl/i2004-10452-6 (2005).

50 Miron, I. M. *et al.* Perpendicular switching of a single ferromagnetic layer induced by in-plane current injection. *Nature* **476**, 189-193, doi:10.1038/nature10309 (2011).

51 Skinner, T. D. *et al.* Spin-orbit torque opposing the Oersted torque in ultrathin Co/Pt bilayers. *Applied Physics Letters* **104**, 062401, doi:10.1063/1.4864399 (2014).

52 Manchon, A. Spin–orbitronics: A new moment for Berry. *Nature Physics* **10**, 340-341, doi:10.1038/nphys2957 (2014).

53 Emori, S., Bauer, U., Woo, S. & Beach, G. S. D. Large voltage-induced modification of spin-orbit torques in Pt/Co/GdOx. *Applied Physics Letters* **105**, 222401, doi:10.1063/1.4903041 (2014).

54 Brataas, A. & Hals, K. M. Spin-orbit torques in action. *Nature nanotechnology* **9**, 86-88, doi:10.1038/nnano.2014.8 (2014).

55 Fert, A., Cros, V. & Sampaio, J. Skyrmions on the track. *Nature nanotechnology* **8**, 152-156, doi:10.1038/nnano.2013.29 (2013).

56 Rohart, S. & Thiaville, A. Skyrmion confinement in ultrathin film nanostructures in the presence of Dzyaloshinskii-Moriya interaction. *Physical Review B* **88**, doi:10.1103/PhysRevB.88.184422 (2013).

57 Aharoni, A. *Introduction to the theory of ferromagnetism*. (Oxford, Clarendon Press, 1996).

58 Hubert, A. & Schäfer, A. *Magnetic domain*. (Springer Berlin Heidelberg, 1998).

59 Coey, J. M. D. *Magnetism and magnetic materials*. (Canbridge University Press, 2009).

60 Donahue, M. J. a. P., D.G. . *OOMMF User's Guide, Version 1.0*, <http://math.nist.gov/oommf> (1999).

61 Vansteenkiste, A. *et al.* The design and verification of MuMax3. *AIP Advances* **4**, 107133, doi:10.1063/1.4899186 (2014).

62 Scholz, W. *et al.* Scalable parallel micromagnetic solvers for magnetic nanostructures. *Computational Materials Science* **28**, 366-383, doi:http://dx.doi.org/10.1016/S0927-

0256(03)00119-8 (2003).

63 Fischbacher, T., Franchin, M., Bordignon, G. & Fangohr, H. A Systematic Approach to Multiphysics Extensions of Finite-Element-Based Micromagnetic Simulations: Nmag. *Magnetics, IEEE Transactions on* **43**, 2896-2898, doi:10.1109/TMAG.2007.893843 (2007).

64 Ha, J. K., Hertel, R. & Kirschner, J. Micromagnetic study of magnetic configurations in submicron permalloy disks. *Physical Review B* **67**, 224432 (2003).

65 Lee, K.-S. & Kim, S.-K. Two circular-rotational eigenmodes and their giant resonance asymmetry in vortex gyrotropic motions in soft magnetic nanodots. *Physical Review B* **78**, doi:10.1103/PhysRevB.78.014405 (2008).

66 Lee, K.-S. & Kim, S.-K. Gyrotropic linear and nonlinear motions of a magnetic vortex in soft magnetic nanodots. *Applied Physics Letters* **91**, 132511, doi:10.1063/1.2783272 (2007).

67 Pribiag, V. S. *et al.* Magnetic vortex oscillator driven by d.c. spin-polarized current. *Nature Physics* **3**, 498-503, doi:10.1038/nphys619 (2007).

68 Hertel, R. & Schneider, C. M. Exchange explosions: Magnetization dynamics during vortex-antivortex annihilation. *Physical review letters* **97**, 177202, doi:10.1103/PhysRevLett.97.177202 (2006).

69 Hertel, R., Gliga, S., Fahnle, M. & Schneider, C. M. Ultrafast nanomagnetic toggle switching of vortex cores. *Physical review letters* **98**, 117201, doi:10.1103/PhysRevLett.98.117201 (2007).

70 Tretiakov, O. A. & Tchernyshyov, O. Vortices in thin ferromagnetic films and the skyrmion number. *Physical Review B* **75**, doi:10.1103/PhysRevB.75.012408 (2007).

71 Noske, M., Stoll, H., Fähnle, M., Hertel, R. & Schütz, G. Mechanisms for the symmetric and antisymmetric switching of a magnetic vortex core: Differences and common aspects. *Physical Review B* **91**, doi:10.1103/PhysRevB.91.014414 (2015).

72 Lee, K. S. *et al.* Universal criterion and phase diagram for switching a magnetic vortex core in soft magnetic nanodots. *Physical review letters* **101**, 267206, doi:10.1103/PhysRevLett.101.267206 (2008).

73 Petit-Watelot, S. *et al.* Commensurability and chaos in magnetic vortex oscillations. *Nature Physics* **8**, 682-687, doi:10.1038/nphys2362 (2012).

74 Caputo, J. G., Gaididei, Y., Mertens, F. G. & Sheka, D. D. Vortex polarity switching by a spin-polarized current. *Physical review letters* **98**, 056604, doi:10.1103/PhysRevLett.98.056604 (2007).

75 Mistral, Q. *et al.* Current-driven vortex oscillations in metallic nanocontacts. *Physical review letters* **100**, 257201, doi:10.1103/PhysRevLett.100.257201 (2008).

76 Choi, Y.-S., Lee, K.-S. & Kim, S.-K. Quantitative understanding of magnetic vortex oscillations

driven by spin-polarized out-of-plane dc current: Analytical and micromagnetic numerical study. *Physical Review B* **79**, doi:10.1103/PhysRevB.79.184424 (2009).

77 Khvalkovskiy, A. V., Grollier, J., Dussaux, A., Zvezdin, K. A. & Cros, V. Vortex oscillations induced by spin-polarized current in a magnetic nanopillar: Analytical versus micromagnetic calculations. *Physical Review B* **80**, doi:10.1103/PhysRevB.80.140401 (2009).

78 Im, M. Y. *et al.* Stochastic formation of magnetic vortex structures in asymmetric disks triggered by chaotic dynamics. *Nature communications* **5**, 5620, doi:10.1038/ncomms6620 (2014).

79 Marion, J. B. & Thornton, S. T. *Classical Dynamics* Vol. chapter 4 (Harcourt College Publishers, 2009).

80 Lee, K. S., Yoo, M. W., Choi, Y. S. & Kim, S. K. Edge-soliton-mediated vortex-core reversal dynamics. *Physical review letters* **106**, 147201, doi:10.1103/PhysRevLett.106.147201 (2011).

81 Hertel, R. Magnetic nanostructures: vortex states a la carte. *Nature nanotechnology* **8**, 318-320, doi:10.1038/nnano.2013.81 (2013).

82 Schneider, M., Hoffmann, H. & Zweck, J. Magnetic switching of single vortex permalloy elements. *Applied Physics Letters* **79**, 3113, doi:10.1063/1.1410873 (2001).

83 Pang, Z., Yin, F., Fang, S., Zheng, W. & Han, S. Micromagnetic simulation of magnetic vortex cores in circular permalloy disks: Switching behavior in external magnetic field. *Journal of Magnetism and Magnetic Materials* **324**, 884-888, doi:http://dx.doi.org/10.1016/j.jmmm.2011.10.012 (2012).

84 Cambel, V. & Karapetrov, G. Control of vortex chirality and polarity in magnetic nanodots with broken rotational symmetry. *Physical Review B* **84**, doi:10.1103/PhysRevB.84.014424 (2011).

85 Dumas, R. K., Gilbert, D. A., Eibagi, N. & Liu, K. Chirality control via double vortices in asymmetric Co dots. *Physical Review B* **83**, doi:10.1103/PhysRevB.83.060415 (2011).

86 Tobik, J., Cambel, V. & Karapetrov, G. Asymmetry in Time Evolution of Magnetization in Magnetic Nanostructures. *Scientific reports* **5**, 12301, doi:10.1038/srep12301 (2015).